University of Strathclyde

# Mixing Processes in Anti-solvent Crystallisation

*Author:*
Russell Miller

*Supervisors:*
Prof. Jan Sefcik
Dr. Leo Lue

# Acknowledgements

I'd like to express my gratitude to my PhD supervisors, Jan Sefcik and Leo Lue, for their invaluable guidance and support throughout my doctoral journey. I also extend my thanks to my Takeda supervisor, Neda Nazemifard, and our co-op student, Isabella Cardona Barber, for their valuable input and support in my research. Special appreciation goes to CMAC for creating a supportive environment during my PhD, and to the friends I've had the privilege to meet along the way.

I want to acknowledge the unwavering support of my friends and family over the past five years. Lastly, I've dedicated a video to those who played a significant role during the challenging moments of my PhD:

https://youtu.be/wGRF3GQ4Wdk?si=UEDCcWLz1aVWwp77

# Abstract

Mass transfer phenomena play an important role in many chemical and physical processes, such as crystallisation, and, therefore, it is essential to develop a better fundamental understanding of mass transfer effects in order to design more efficient crystallisation processes. It is aimed to investigate mixing within the context of anti-solvent crystallisation. Two mixing scales are studied, micro-mixing and macro-mixing. The first part of this thesis focuses on diffusive mixing in anti-solvent process and how it relates to turbulent mixing. This is subsequently followed by the characterisation of mixing times in one litre vessels. Through using a combined experimental and CFD approach insight into macroscopic mixing process will be gained for common anti-solvent solvent pairs.

At the micro-scale local concentration profiles at interfaces between segregated fluid elements are controlled through diffusion. Consequently diffusion is a significant step of the mixing process. This is particularly true for anti-solvent crystallisation in which nucleation outcomes are strongly influenced by localised concentration profiles. Previous work on modelling relied on a Fickian framework where concentration gradients are the driving force for diffusion. This predicts large overshoots in the supersaturation at interfaces between solution and anti-solvent, as is often intuitively expected. In this work, a thermodynamically consistent diffusion model was developed and applied to anti-solvent systems. In this model chemical potential gradients provide a more physically realistic driving force for diffusion. "Non-intuitive" behaviour was predicted for diffusion in highly non-ideal liquid systems. In particular, as solute diffusion towards anti-solvent is severely hindered, it can diffuse against its concentration gradient away from anti-solvent. Furthermore large supersaturation overshoots above that at the final mixture composition are not found when thermodynamically consistent approach is used, demonstrating that these overshoots are modelling artefacts and are not expected to be present in physical systems.

In addition, for certain conditions, localised liquid-liquid spinodal demixing is

predicted to occur during the diffusive mixing process, even when the final mixture composition is outside the liquid-liquid phase separation region. Intermittent spinodal demixing driven by diffusive mixing may provide a novel explanation for differences of nucleation behaviours among various anti-solvents. Further investigation of this phenomenon found that higher anti-solvent content within the system increased the likelihood for LLPS.

On the macro-scale, mixing occurs predominately through turbulent mechanisms in which velocity fields act to spatially rearrange fluid elements within the system. Turbulent dissipation leads to the reduction of these elements to the Batchelor length scale, in which diffusion becomes the prevalent mass transfer mechanism. Periodic boundary conditions were used to approximate the case of multiple solution-anti-solvent layers in parallel to give a better representation of diffusive mixing in turbulent systems. A qualitative discussion is offered on the relation of the developed model to other micro-mixing models reported in literature.

Macroscopic mixing was investigated through characterising mixing times for a 1litre optimax reactor using a combined experimental and computational fluid dynamics (CFD) approach. Mixing times were then calculated from the resulting conductivity profiles in three ways; the 95% homogenisation method, and through fitting exponential and first order plus dead-time models. The geometry of the system was modelled and simulated on Mstar CFD to predict mixing times. Local and global mixing times were calculated by using a simulated probe, and the tracer concentration relative standard deviation throughout the vessel respectively.

Firstly, The predicted variability of mixing from the Mstar simulations for the addition of a tracer to water, including the effects of tracer repeats and addition location is explored. Following this, the experimental results are discussed, with a comparison of mixing time determination methods shown. Subsequently, the predicted and experimental results are compared. Effects of initial solvent composition on mixing times are then

investigated. Lastly, we present the mixing times for the addition of ethanol to water, once more utilising both CFD and experimental conductivity method. Across all mixing time measurements, a wide variance was found to be present, highlighting the inherent variability associated with mixing processes.

# Contents

## List of symbols

List of symbols used within this thesis. Note this will split between two lists; one for the diffusive mixing work, and one for the macroscopic mixing work. This is due to some SI symbols having different meanings depending on context. Instead of defining our own symbols, it was decided to split over two distinct lists.

### Diffusive Work - Chapters 1-5.

Table 1: Table of Symbols used in the context of the diffusive work, corresponding to chapters 1-5 (part 1)

| Symbol | Definition |
|---|---|
| $A$ | Pre-exponential Factor in classical nucleation theory equation (Eqn 2.42) |
| $B$ | Constant in classical nucleation theory equation (Eqn 2.42) |
| $C_i$ | Molar concentration |
| $C_r$ | Solubility for particles of size (radius) r |
| $C^*$ | Bulk solubility of dissolved particles in solution |
| $C_t$ | Total Molar Concentration |
| $D_{ij}$ | Fickian binary diffusion coefficient |
| $Đ_{ij}$ | Maxwell-Stefan diffusion coefficient |
| $\mathbb{D}_{21}^{\phi}$ | Diffusion coefficient (volume reference frame) |
| $F_{ij}$ | Friction coefficient |
| $G$ | (Gibbs) Free energy |
| $\Delta G_v$ | Free energy change for phase transformation |
| $\Delta H_f$ | Heat of fusion |
| $\boldsymbol{J}$ | Diffusive flux |
| $j$ | Nucleation rate |
| $k$ | Boltzmann constant |
| $L_b$ | Bachelor length scale |
| $L_k$ | Kolomogorov length scale |
| $m_i$ | Molecular weight |
| $N_a$ | Avogadro constant |
| $N_i$ | Molar flux |
| $n_i$ | Number of mols |
| $R$ | Ideal gas constant |
| $r$ | Radius of the nucleus |
| $r_c$ | Critical radius of nucleus |

Table 2: Table of Symbols used in the context of the diffusive work corresponding to chapters 1-5 (part 2)

| Symbol | Definition |
|---|---|
| $S$ | Supersaturation |
| $T$ | System temperature |
| $T_f$ | Solute fusion temperature |
| $u$ | Reference velocity |
| $u_i$ | Mean velocity of species i |
| $u^a$ | Velocity based on the generalised reference frame 'a' |
| $V_i$ | Pure component molar volume |
| $x_0$ | Solubility of solute in solution (Mol fraction) |
| $x_i$ | Mol fraction of 'i' |
| $\beta$ | Thermodynamic constant (isothermal system) $1/RT$ |
| $\Gamma$ | Thermodynamic factor |
| $\gamma_{ij}$ | Activity coefficient |
| $\epsilon$ | Turbulent energy dissipation rate |
| $\mu_i$ | Chemical potential |
| $\mu_0^s$ | Chemical potential of pure solid solute in solution |
| $\nu$ | molar volume of component in solution |
| $\nu_{ref}$ | Reference volume used in free energy model (Eqn 3.1) |
| $\omega_i$ | Mass fraction |
| $\rho$ | Density |
| $\sigma$ | Inter-facial tension |
| $\phi_i$ | Volume fraction used in diffusion model (Eqn 3.16 ) |
| $\varphi_i$ | Volume fraction used in free energy model (Eqn 3.1 |
| $\chi_{ij}$ | Binary interaction parameter (Eqn 3.1) |

## Macroscopic mixing Work - Chapter 6

Table 3: Table of Symbols used in the context of the macroscopic mixing work corresponding to chapters 6

| Symbol | Definition |
|---|---|
| $D$ | Impeller diameter |
| $H$ | Liquid height |
| $K$ | K mixing constant (Eqn 6.7) |
| $N$ | Number of impeller rotations |
| $P$ | Power input |
| $P_0$ | Power number |
| $Q(f,f)$ | Collision operator |
| $Re$ | Impeller Reynolds' number |
| $T$ | Tank diameter |
| $T_d$ | Delay time |
| $\epsilon$ | Power per unit volume |
| $\theta$ | Mixing time |
| $\mu$ | Dynamic viscosity |
| $\nu$ | Kinematic viscosity |
| $\rho$ | Density |
| $\tau$ | Relaxation time |

# List of Figures

# List of Tables

# Chapter 1

# Research Context

## 1.1 Introduction

In process engineering, mixing can strongly influence the outcomes and efficacy of many physical and chemical processes. This is particularly the case for processes that have a high dependence on local species concentrations such as chemical reactions or separations such as crystallisation. For this reason the field of mixing has been well studied in the literature. With relation to crystallisation, there has been an emphasis on research pertaining to mixing at the macroscopic scale, and the significance of diffusive mixing at micro-scale can be under estimated. Intuitively the focus on the macroscopic scale makes sense. Mixing in typical crystallisation processes is dominated through turbulent dispersion and consequently diffusive timescales are relatively quick in comparison to the bulk-scale mixing. It can however be argued that the final stage in mixing processes is molecular diffusion and therefore it is diffusion that controls local concentration profiles within the fluid mixture. If we consider the sensitivity of crystallisation kinetics on local fluid compositions the importance of diffusion becomes apparent and highlights the needs for a better understanding of effects of diffusive mixing on crystallisation processes.

With localised fluid compositions influencing crystallisation kinetics, anti-solvent crystallisation can be considered a mixing controlled process. Various mixing techniques can be employed to control mixing to provide suitable conditions for the desired crystallisation outcomes, e.g. crystal solid from or crystal size distributions (CSD). For example, precipitation processes can be used to produce very small particle sizes.[1] Precipitation crystallisation requires fast nucleation rates, which necessitates the rapid generation of high levels of supersaturation. Multiple techniques can be used to achieve this including Confined Impinging Jet Reactors[2] and Y-mixers.[3] However, for all mixing controlled processes local composition is dictated through micro-mixing processes. With the aim of providing a quantitative description of mixing at the micro-scale, numerous micro-mixing models have been proposed such as the slab shrinkage model[4] or the engulfment-deformation-diffusion model.[5] These models envisage the micro-mixing process as the creation of fluid layers which are stretched and deformed due to turbulent dissipation. Mass transfer between these layers occurs through diffusion. Whilst these models offer a sufficient description of the micro-mixing process as a whole, they do not fully capture the spatial and temporal complexity of the diffusive process. Often diffusion is modelled using a Fickian framework for binary components in ideal solutions; two assumptions that fail for anti-solvent crystallisation processes which are both multi-component and highly non-ideal by definition. This can lead to micro-mixing models predicting vastly different nucleation conditions than those experienced experimentally. This work aims to provide a proper description of the diffusion process within anti-solvent systems which will assist in the control and design of anti-solvent crystallisation processes.

Previously published literature on diffusion in crystallisation processes is very limited however the emergence of microfluidic crystallisation has created opportunity to develop a better understanding.[6] One such study was the polymorphic screening in the anti-solvent crystallisation of indomethacine within a microfluidic platform.[7] Another study investigated the continuous anti-solvent crystallisation of glycine in a microfluidic channel.[8] In both studies, the mixing process was modelled alongside the experimental crystallisation. The former assumed mixing was diffusion only, using a Fickian framework used. The latter modelled mixing through solving the convective-diffusive equation, with Fickian diffusion. Authors then used calculated supersaturation profiles to interpret experimental results to deduce qualitative insights into the relationship between mixing and nucleation outcomes. However, using this approach, local concentration profiles at interfaces between solution and anti-solvent fluid elements can give rise to significant supersaturation overshoots over and above that at the final mixture composition, potentially leading to poorly controlled nucleation.

Using this approach diffusion was modelled with the assumption of ideal solutions with the driving force for diffusion taken as the species concentration gradients. Additionally, the solvent was considered as the background solvent, i.e. the anti-solvent and solute were modelled as binary diffusion through the solvent and multi-component interactions are not accounted for. Anti-solvent crystallisation processes inherently involve non-ideal solutions with and involve three or more components in appreciable quantities. Thus the assumptions of ideal solution and diffusion of dilute species do not give a good representation of the physical system. To further understanding into the role of diffusion in anti-solvent crystallisation it is necessary to account for these effects. In this thesis, these assumptions are avoided and diffusion is modelled through a more rigorous Maxwell-Stefan approach. This formulation provides a thermodynamically consistent diffusion model, accounting for solution non-ideality and multi-component interactions. Chapter 3 of this thesis describes the development of this model. The application of the model to ternary component anti-solvent systems is given in Chapter 4. This allows for a physically correct description of the diffusion mixing process, and provides novel insights into the effect of solution non-ideality in anti-solvent crystallisation systems.

Whilst diffusive mixing was discussed above in the context of microfluidic crystallisation, the diffusive mixing model is also qualitatively related to macro-scale mixing processes. At larger scale turbulent dissipation spatially arrange fluid elements within the system. During this process, species concentration remains unchanged within each individual element. Local turbulent eddies act to deform and stretch these elements, reducing them to the Batchelor length scale. At this scale diffusion becomes dominant and species exchange occurs where diffusion determines localised composition profiles experienced during the mixing process. Chapter 5 further explores diffusive mixing in anti-solvent crystallisation including the occurrence of liquid-liquid phase separation and effect of anti-solvent choice. A qualitative discussion on the length-scale where the developed model becomes relevant is also offered.

Overall mixing times in agitated vessels are typically controlled by macroscopic mixing and can vary from seconds to thousands of seconds depending on vessel scale. Poor mixing can lead to regions of high supersaturation within a crystallisation vessel and lead to crystals with undesirable properties being obtained. For these reasons a better understanding of macroscopic mixing is also required to improve the efficiency of anti-solvent crystallisation processes. Chapter 6 characterises mixing in one litre vessels for miscible liquid systems using a typical anti-solvent/solution pair as the model system. A combined experimental and CFD approach was taken with a comparison made between the two approaches.

## 1.2 Thesis overview

This thesis is organised around three paper manuscripts (1 published, 2 to be submitted); corresponding to chapters 4,5 and 6 respectively. Chapter 2 provides background theory to diffusion models and gives a brief introduction to crystallisation. Chapter 3 shows the detailed derivation of a diffusive mixing model. Chapters 4 & 5 applies this model to anti-solvent systems. Chapter 6 investigates mixing in one litre vessels. Below is an overview of the thesis structure, with a brief summary of each chapter. The research aims and objectives are highlighted on a chapter by chapter basis.

### Chapter 1: Research context:

An introduction to the research carried out is provided, followed by the thesis overview, summarising the content of each chapter.

### Chapter 2: Background theory:

The background theory section discusses diffusive models and briefly introduces relevant crystallisation concepts.

## Chapter 3: Formulation of diffusion model:

To predict diffusive mixing in anti-solvent crystallisation, diffusion was modelled using a Maxwell-Stefan approach, the derivation of which is described here. With the thesis following a publication format, a detailed application of the model is described in the methodology sections in chapter 4 and 5.

## Chapter 4: Diffusive mixing in anti-solvent crystallisation:

Diffusion controls local concentration profiles at interfaces between segregated fluid elements during mixing processes. This is important for anti-solvent crystallisation, where it is often intuitively argued that local concentration profiles at interfaces between solution and anti-solvent fluid elements can give rise to significant supersaturation overshoots over and above that at the final mixture composition, potentially leading to poorly controlled nucleation.

Previous work on modelling diffusive mixing in anti-solvent crystallisation has relied on Fickian diffusion, where concentration gradients are the driving force for diffusion. This predicts large overshoots in the supersaturation at interfaces between solution and anti-solvent, as is often intuitively expected. However, chemical potential gradients provide a more physically realistic driving force for diffusion, and in highly non-ideal solutions, including those in anti-solvent crystallisation, this leads to “non-intuitive” behaviour. In particular, as solute diffusion towards anti-solvent is severely hindered, it can diffuse against its concentration gradient away from anti-solvent. a thermodynamically consistent diffusion model based on the multi-component Maxwell-Stefan formulation is applied to examine diffusive mixing in a non-ideal anti-solvent crystallisation system.

Large supersaturation overshoots above that at the final mixture composition are not found when thermodynamically consistent approach is used, demonstrating that these overshoots are modelling artefacts and are not expected to be present in physical systems.

In addition, for certain conditions, localised liquid-liquid spinodal demixing is predicted to occur during the diffusive mixing process, even when the final mixture composition is outside the liquid-liquid phase separation region. Intermittent spinodal demixing driven by diffusive mixing may provide a novel explanation for differences of nucleation behaviours among various anti-solvents.

### Chapter 5: Diffusive mixing in anti-solvent crystallisation: effect of anti-solvent and macroscopic mixing:

On the macro-scale, mixing occurs predominately through turbulent mechanisms in which velocity fields act to spatially rearrange fluid elements within the system. Turbulent dissipation leads to the reduction of these elements to the Batchelor length scale, in which diffusion becomes the prevalent mass transfer mechanism. with nucleation being sensitive to local solution composition, diffusion undoubtedly influences the outcomes of crystallisation processes.

In the previous chapter, a thermodynamically consistent diffusion model was developed and applied to an anti-solvent crystallisation system. It was found that activity gradients within the system resulted in the solute moving away from the solution/anti-solvent interface, and large overshoots in supersaturation were not experienced. Interestingly localised liquid-liquid phase separation (LLPS) was predicted to occur under conditions in which final composition would suggest otherwise.

This chapter further investigates diffusive mixing in anti-solvent crystallisation. LLPS occurrence within anti-solvent systems is further explored alongside the effect of anti-solvent choice on diffusive mixing. It was found that higher anti-solvent content within the system caused LLPS.

Periodic boundary conditions were used to approximate the case of multiple solution-anti-solvent layers in parallel to give a better representation of diffusive mixing in turbulent systems. A qualitative discussion is offered on the relation of the developed model to other micro-mixing models reported in literature. Diffusion mixing times were found to be comparable to Batchelor time-scales.

### Chapter 6: Mixing times of miscible liquid systems in agitated vessels:

This chapter focuses on mixing at the macro-scale in which mixing times were characterised for a one litre agitated vessel using a combined experimental and computational fluid dynamics (CFD) approach. Experimental mixing times were determined through the injection of a sodium chloride tracer and measuring the conductivity. Mixing times were then calculated from the resulting conductivity profiles in three ways; the 95% homogenisation method, and through fitting exponential and first order plus dead-time models. The geometry of the system was modelled and simulated using Mstar CFD (based on an large eddy simulation approach) to predict mixing times. Local and global mixing times were calculated by using a simulated probe, and the tracer concentration relative standard deviation throughout the vessel respectively.

Firstly, The variability of mixing times from the Mstar simulations for the addition of a tracer to water, including the effects of tracer repeats and addition location is explored. Following this, the experimental results are discussed, with a comparison of mixing time determination methods shown. Subsequently, the predicted and experimental results are compared. Effects of initial solvent composition on mixing times are then investigated. Lastly, we present the mixing times for the addition of ethanol to water, once more utilising both CFD and experimental conductivity method. Across all mixing time measurements, a wide variance was found to be present, highlighting the inherent variability associated with turbulent mixing processes.

### Chapter 7: Conclusions:

The findings from this research are summarised and discussed within the context if anti-solvent crystallisation discussed.

## 1.3 References

[1] D L. Marchisio, L Rivautella, and A A. Barresi. Design and scale-up of chemical reactors for nanoparticle precipitation. *AIChE J.*, 52(5):1877–1887, 2006.

[2] Emmanuela G., D. L. Marchisio, and A. A. Barresi. Cfd modelling and scale-up of confined impinging jet reactors. *Chem. Eng. Sci.*, 62(8):2228–2241, 2007.

[3] B Judat and M Kind. Morphology and internal structure of barium sulfate—derivation of a new growth mechanism. *J. Colloid Interface Sci.*, 269(2):341–353, 2004.

[4] L X and C G. Simplified Framework for Description of Mixing with Chemical Reactions I: Physical Picture of Micro- and Macromixing. *Chin. J. Chem. Eng.*, 4(4):311–321, 1996.

[5] J. Baldyga and J.R. Bourne. Simplification of micromixing calculations. i. derivation and application of new model. *J. Chem. Eng.*, 42(2):83–92, 1989.

[6] H H Shi et al. Progress of crystallization in microfluidic devices. *Lab Chip*, 17(13):2167–2185, 2017.

[7] Michael R. Thorson et al. Microfluidic approach to polymorph screening through antisolvent crystallization. *CrystEngComm*, 14(7):2404, 2012.

[8] Venkateswarlu Bhamidi et al. Antisolvent Crystallization and Polymorph Screening of Glycine in Microfluidic Channels Using Hydrodynamic Focusing. *Cryst Growth Des.*, 15(7):3299–3306, 2015.

# Chapter 2

# Background Theory

## 2.1 Fickian diffusion: binary systems

In 1831, Thomas Graham published some of the earliest studies into diffusive mass transfer.[1–3] Through experimentally observing the diffusion of gases escaping a glass cylindrical tube into air,[1] it was concluded that the rate of diffusion is inversely proportional to the square root of its density. Further work investigated diffusive phenomena in liquids[4] in which Graham related the diffusive flux of a species to its concentration gradient within a mixture. This relation was not formalised until 1855 by Adolf Fick.[5] As an analogy to the phenomenological laws of heat and electricity conduction, Fick postulated that the diffusive flux of species 'i' in a binary mixture of 'i' and 'j' is related to its concentration gradient through the linear relationship:

$$\boldsymbol{J_i} = -C_t D_{ij} \left( \frac{\partial x_i}{\partial z} \right) \tag{2.1}$$

Where $J$ is flux (mols/$m^2 s^2$), $C_t$ is total molar concentration of the system (mols/$m^3$), $x_i$ is mol fraction of 'i'. $\partial x_i / \partial z$ is thus the composition gradient of 'i' and describes the driving force for diffusion. The negative sign indicates that diffusion occurs from regions of high to low concentration. Following from this diffusion results in a uniform distribution of a species within a mixture.

$D_{ij}$ ($m^2/s$) is a proportionality constant and is known as the diffusion coefficient or diffusivity. The subscript 'ij' specifies that it is the diffusivity of species 'i' in 'j'. For a binary system there is only one independent composition gradient and flux. As a consequence the diffusion coefficients are symmetrical in binary systems, i.e. $D_{ij} = D_{ji}$. For liquid systems diffusivity is generally composition dependent and can be expressed as some function of composition. Given one composition gradient equation, the solution of equation 2.1 becomes straightforward and the diffusive flux can be estimated.

## 2.2 Maxwell-Stefan diffusion: binary systems

The Maxwell-Stefan (MS) approach to diffusion[6–10] was developed independently by James Maxwell[11] and Josef Stefan[12] in the second half of the 19th century. This approach can be derived through taking a force balance on the diffusing species. For isothermal diffusion within a bulk fluid phase, the driving force is taken as the chemical potential gradient throughout the system, which represent the deviations from thermodynamic equilibrium. The driving force ($d_i^{chem}$) can be expressed through equation 2.2.

$$d_i^{chem} = -\boldsymbol{\nabla_{T,P}\ \mu_i} \tag{2.2}$$

The chemical potential of a system can be defined as;

$$\beta\mu_i = \beta\mu^0 + Ln(x_i) + Ln(\gamma_i) \tag{2.3}$$

Where $\beta$ is $1/RT$, with R being the ideal gas constant ($jmol^-1K^-1$), and T is system temperature (K). Temperature is assumed to be constant. $\gamma$ denotes the activity coefficient of component i. Taking the derivative of equation 2.3 with respect to $x_i$ and rearranging for $\partial\mu$, we can express $d_i$ through equation 2.4.

$$d_i^{chem} = -RT\left(\frac{1}{x_i} + \frac{\partial ln(\gamma_i)}{\partial x_i}\right)\boldsymbol{\nabla_{T,P}\ x_i} \tag{2.4}$$

This driving force is balanced by the friction experienced as species i diffuses past species j. Assuming that the frictional forces ($f_i$) are proportional to the relative velocity of i to j, and to the concentration of j within the mixture, friction may be expressed as;

$$f_i = F_{ij} x_j \left(u_i - u_j\right) \tag{2.5}$$

$F_{ij}$ denotes the friction coefficient which can be related to the Maxwell-Stefan diffusion coefficient ($Đ_{ij}$) through $F_{ij} = \frac{RT}{Đ_{ij}}$.[9, 10] The Maxwell-Stefan diffusion coefficient can therefore be interpreted as the inverse drag coefficient. Equating $f_i$ and $d_i^{chem}$ and multiplying through by $x_i/RT$ we get;

$$-\left(1 + x_i \frac{\partial ln(\gamma_i)}{\partial x_i}\right) \boldsymbol{\nabla x_i} = \frac{1}{Đ_{ij}} x_i x_j \left(u_i - u_j\right) \tag{2.6}$$

Defining the thermodynamic factor $\Gamma$ as;

$$\Gamma_{ij} = \left(1 + x_i \frac{\partial ln(\gamma_i)}{\partial x_j}\right) \tag{2.7}$$

and noting the definition of flux as $J_i = C_t x_i (u_i - u)$ in which $C_t$ is total molar concentration and $u$ is the reference velocity (molar averaged in this case), equation 2.6 can be expressed as;

$$-\Gamma_{ij} \boldsymbol{\nabla x_i} = \frac{1}{C_t Đ_{ij}} \left(x_j \mathbf{J_i} - \mathbf{x_i J_j}\right) \tag{2.8}$$

Diffusive fluxes for each component are related through;

$$\sum_{i=1} \mathbf{J_i} = \mathbf{0} \tag{2.9}$$

Consequently, in a binary system $j_i$ = -$j_j$. Equation 2.8 can be transposed to yield an explicit formula for $j_i$.

$$\boldsymbol{J_i} = -C_t Đ_{ij} \Gamma_{ij} \boldsymbol{\nabla x_i} \tag{2.10}$$

Similarly to the Fickian coefficients, due to only one independent flux existing, the MS coefficients are symmetrical. Comparing this to the binary Fickian equation it is found that the Fickian and MS diffusivities are related through $\Gamma_{ij}$. That is $D_{ij} = \Gamma_{ij} Đ_{ij}$. Thus, if a free energy model is used to estimate the activity coefficient of a system conversion between the two diffusion coefficients is straightforward. In the simplest case of an ideal binary mixture, $\Gamma = 1$ & $D_{ij} = Đ_{ij}$ and equation 2.10 reduces to Fickian diffusion.

## 2.3 Multi-component diffusion

In the previous sections, the Fickian and Maxwell-Stefan diffusion equations were discussed for binary systems. Most chemical processes involve more than two components and to accurately model diffusion it becomes necessary to account for interactions between each diffusing species within the mixture. Fickian diffusion can be formally extended for multi-component interactions through[13, 14]

$$\mathbf{J_i} = -\mathbf{C_t} \sum_{\mathbf{j=1}}^{\mathbf{n-1}} \mathbf{D_{ij}} \boldsymbol{\nabla} \mathbf{x_i} \ , \ (\mathbf{i = 1....n-1}) \tag{2.11}$$

There are now (n-1) independent fluxes, with each now being dependent not only on its own composition gradient, but those of the other diffusion components as well. The diffusivity of the system is described by a $(n-1)^2$ matrix of diffusion coefficients. The expanded form of equation 2.11 is given below;

$$\begin{pmatrix} \mathbf{J_1} \\ \mathbf{J_2} \\ \vdots \\ \mathbf{J_{n-1}} \end{pmatrix} = -C_t \begin{pmatrix} D_{11} & D_{12} & \dots & D_{1,n-1} \\ D_{21} & D_{22} & \dots & D_{2,n-1} \\ \vdots & \vdots & \ddots & \vdots \\ D_{n-1,1} & D_{n-1,2} & \dots & D_{n-1,n-1} \end{pmatrix} \cdot \begin{pmatrix} \boldsymbol{\nabla x_1} \\ \boldsymbol{\nabla x_2} \\ \\ vdots \\ \boldsymbol{\nabla x_{n-1}} \end{pmatrix} \tag{2.12}$$

The main diffusivity refers to the diagonal of the matrix and relates the flux of a component with its own composition gradient. The off-diagonal of the matrix connects the flux of component to the other components, and referred to as the cross diffusivity. A few notes on the diffusion coefficients are worth mentioning. Generally, these diffusion coefficients are not symmetrical ($D_{ij} \neq D_{ji}$).[6] Further complicating the diffusion coefficients is that they are the results of complex multi-component interactions between all diffusing components in the mixture. The multi-component Fickian diffusion coefficients are therefore not relatable to the binary form. For example the diffusion coefficient 'ij' in the multi-component diffusivity does not equal $D_{ij}$ in the binary case. This complicates the experimental measurement of multi-component diffusivity matrix and limits the practicality of the equations.

The Maxwell-Stefan formulation provides a more convenient description of multi-component diffusion. The binary form can be extended for multi-component mixtures by considering the other components present when determining the frictional forces ($f_i$). In terms of fluxes, the generalised multi-component Maxwell-Stefan formulation is defined as;

$$-\frac{x_i}{RT}\boldsymbol{\nabla \mu_i} = \sum_{j \neq i}^{n} \frac{1}{C_t Đ_{ij}}(x_j\mathbf{J}_i - x_i\mathbf{J}_j) \tag{2.13}$$

The chemical potential gradients in the system must satisfy the Gibbs-Duhem relationship ($\sum_i^n \nabla\mu = 0$) resulting in only (n-1) independent driving forces existing. This property is used to reduce equation 2.13 into equation 2.14. Note we once more introduce the thermodynamic factor allowing for the driving force to be represented as the composition gradients.

$$-C_t\Gamma \begin{pmatrix} \nabla \mathbf{x_1} \\ \nabla \mathbf{x_2} \\ \vdots \\ \nabla \mathbf{x_{n-1}} \end{pmatrix} = B \begin{pmatrix} \boldsymbol{J_1} \\ \boldsymbol{J_2} \\ \vdots \\ \mathbf{J_{n-1}} \end{pmatrix} \tag{2.14}$$

$\Gamma$ and B represent (n-1) dimensional matrices for the thermodynamic factors and diffusivity respectively. $\Gamma$ is calculated through $\Gamma_{ij} = \left(\delta_{ij} + x_i \frac{\partial ln(\gamma_i)}{\partial x_j}\right)$, whilst the elements of B are given by;

$$B_{ii} = \frac{x_i}{Đ_{in}} + \sum_{k=1,k\neq i}^{n} \frac{x_k}{Đ_{ik}} \tag{2.15}$$

$$B_{ij} = -x_i \left(\frac{1}{Đ_{ij}} - \frac{1}{Đ_{in}}\right) \tag{2.16}$$

Equation 2.14 can be cast in to the more common Fickian form by the inversion of the diffusivity matrix, that is,

$$\begin{pmatrix} \boldsymbol{J_1} \\ \boldsymbol{J_2} \\ \vdots \\ \boldsymbol{J_{n-1}} \end{pmatrix} = -C_t\Gamma B^{-1} \begin{pmatrix} \boldsymbol{\nabla x_1} \\ \boldsymbol{\nabla x_2} \\ \vdots \\ \boldsymbol{\nabla x_{n-1}} \end{pmatrix} \tag{2.17}$$

Thus it is seen that the Fickian and MS diffusivity are related through $D = \Gamma B^{-1}$. An example for a ternary component system is given:

$$\begin{pmatrix} \boldsymbol{J_1} \\ \boldsymbol{J_2} \end{pmatrix} = -\frac{1}{\Delta} \begin{pmatrix} \frac{1}{Đ_{23}} + x_1\left(\frac{1}{Đ_{12}} - \frac{1}{Đ_{23}}\right) & x_1\left(\frac{1}{Đ_{12}} - \frac{1}{Đ_{13}}\right) \\ x_2\left(\frac{1}{Đ_{12}} - \frac{1}{Đ_{23}}\right) & \frac{1}{Đ_{13}} + x_2\left(\frac{1}{Đ_{12}} - \frac{1}{Đ_{13}}\right) \end{pmatrix} \Gamma \begin{pmatrix} \boldsymbol{\nabla x_1} \\ \boldsymbol{\nabla x_2} \end{pmatrix} \tag{2.18}$$

where;

$$\Delta = \frac{1}{Đ_{12}Đ_{13}} + \frac{1}{Đ_{12}Đ_{23}} + \frac{1}{Đ_{13}Đ_{23}} \tag{2.19}$$

In this form, one advantage is that the diffusivity is calculated as a weighted average of the binary MS diffusion coefficients. Although Fickian diffusion remains the standard for experimental measurement of binary diffusion coefficient, these are easily converted to their MS counterparts through the $\Gamma$. Another advantage is that MS diffusion coefficients are symmetrical. This reduces the number of diffusion coefficients to $n \times (n-1)/2$ as opposed to the $(n-1)^2$ in Fickian model. Lastly, MS coefficients are independent of reference frame used. With all this in consideration, multi-component diffusion can be practicably and properly described though equation 2.13.

## 2.4 Reference frames for diffusion

In the previous section on diffusion, the formulations were given in the molar reference frame. Diffusive flux is caused by chemical species having differing average velocities from each other. Thus, whilst the general form of the equations are independent of the reference frame used, diffusion is dependent on some reference average velocity. This sections aims to provide the formal definitions of velocity reference frames, and the mathematical basis for converting between different reference frames. We start with defining the total molar flux ($N_i$) of a species;

$$\boldsymbol{N_i} = c_i u_i \tag{2.20}$$

Where $c_i$ and $u_i$ are the molar concentration and mean velocity of species 'i' respectively. Noting that the total flux can be divided into the convective (reversible) and diffusive (thermodynamically irreversible — dissipative) contributions, equation 2.20 can be written as:

$$N_i = c_i u^a + \boldsymbol{J_i^a} \tag{2.21}$$

$u^a$ is the reference velocity based on the generalised reference frame 'a'. The diffusive flux ($\boldsymbol{J_i}$) can then be seen as the relative motion of species $i$ with respect to the reference velocity, and is dependent on the choice of reference frame. Denoting velocity of species 'i' as $u_i$ diffusive flux can be expressed as:

$$\boldsymbol{J_i^a} = c_i \left(u_i - u^a\right) \tag{2.22}$$

In general, for reference frame 'a', we have;

$$u^a = \frac{\sum_{j^n} c_j a_j u_j}{\sum_k^n c_k a_k} \tag{2.23}$$

With n being the number of components in the mixture and $a_i$ being an appropriate weighting property. Common reference frames definitions are given below:[15, 16]

**Molar reference frame (x)**;

$$\boldsymbol{J_i^x} = c_i \left(u_i - u^x\right), \quad u^x = \frac{\sum_j^n c_j u_j}{\sum_k^n c_k} = \sum_j^n x_j u_j \tag{2.24}$$

**Mass reference frame ($\omega$)**;

$$\boldsymbol{J_i^\omega} = c_i \left(u_i - u^\omega\right), \quad u^\omega = \frac{\sum_j^n c_j m_j u_j}{\sum_k^n c_k m_k} = \sum_j^n \omega_j u_j \tag{2.25}$$

**Volume reference frame ($\phi$)**;

$$\boldsymbol{J_i^\phi} = c_i \left(u_i - u^\phi\right), \quad u^\phi = \frac{\sum_j^n c_j V_j u_j}{\sum_k^n c_k V_k} = \sum_j^n \phi_j u_j \tag{2.26}$$

In the above definitions, $x_i$, $\omega_i$ and $\phi_i$ are the molar, mass and volume fraction of component $'i'$. $m_i$ is the molecular weight, whilst $V_i$ is the pure component molar volume. We can switch between reference velocities 'a' and 'b' by considering equations 2.22 & 2.23. $u^a$ can then be expressed through;

$$u^a = \frac{\sum_j^n c_j a_j u_j}{\sum_k^n c_k a_k} = \frac{\sum_j^n a_j \left(\boldsymbol{J_j^b} + c_j u^b\right)}{\sum_k^n c_k a_k} \tag{2.27}$$

And rearranging for $u^a$ - $u^b$;

$$u^a - u^b = \frac{\sum_j^n a_j \boldsymbol{J_j^b}}{\sum_k^n c_k a_k} \tag{2.28}$$

This allows for a relation of different fluxes to each other;

$$\boldsymbol{J_i^a} = c_i \left(u_i - u_i^a\right) = \boldsymbol{J_i^b} + c_i \left(u^b - u_i^a\right) \tag{2.29}$$

Substituting in equation 2.28 we obtain;

$$\boldsymbol{J_i^a} = \sum_j^n \left[\delta_{ij} - \frac{c_i a_j}{\sum_k^n c_k a_k}\right] \boldsymbol{J_j^b} \tag{2.30}$$

This is the generalised equation for switching between two reference frames. By selecting the appropriate property for 'a', we can swap to any arbitrary reference frame. For example, in the case of converting from the molar basis to volume basis, we use the molar volume $V$ as the choice of 'a'. This yields;

$$\boldsymbol{J_i^\phi} = \sum_j^n \left(\delta_{ij} - \phi_i \frac{V_j}{V_i}\right) \boldsymbol{J_j^x} \tag{2.31}$$

The relationship given in equation 2.30 can also be used to connect diffusivities defined using different reference velocities. We can use the Maxwell-Stefan formulation to relate chemical potential gradients and the diffusive flux. Once more we consider reference frames 'a' and 'b'.

$$\boldsymbol{J_i^b} = -\sum_j^n \left(Đ_{ij}^b c_j \beta \boldsymbol{\nabla \mu_j}\right) \tag{2.32}$$

Comparing equations 2.30 & 2.32, it is found;

$$\boldsymbol{J_i^a} = -\sum_j^n \left[\delta_{ij} - \frac{c_i a_j}{\sum_L^n c_L a_L}\right] \sum_k^n \left(Đ_{jk}^b c_k \beta \boldsymbol{\nabla \mu_k}\right) \tag{2.33}$$

This can be simplified to;

$$\boldsymbol{J_i^a} = -\sum_j^n \text{Đ}_{ij}^a c_j \beta \boldsymbol{\nabla \mu_j} \tag{2.34}$$

where,

$$\text{Đ}_{ij}^a = \sum_k \left( \delta_{ik} - \frac{c_i a_k}{\sum_L^n c_L a_L} \right) \text{Đ}_{kj}^b$$

We can therefore convert fluxes and diffusivities from one reference frame to another using equation 2.34. Continuing with the example of the conversion from molar to volume reference frame we get the following for the diffusivity;

$$\text{Đ}_{ij}^\phi = -\sum_k \left( \delta_{ik} - \phi_i \frac{V_k}{V_i} \right) \text{Đ}_{kj}^x \tag{2.35}$$

## 2.5 Introduction to crystallisation

In the pharmaceutical and chemical industry, crystallisation is an important separation process that is used to obtain pure active pharmaceutical ingredients or intermediate products. With crystal properties dictating physical properties such as solubility and compressibility, the control of crystal size, shape and polymorphic form becomes an important consideration for crystallisation processes.

For a new phase to from spontaneously from solution the system must be in a non-equilibrium state with respect to the solute molecules. It is therefore a requirement for the solution to be supersaturated. This can be achieved by lowering the solubility or increasing the concentration of a solute. The solubility can be lowered by cooling or by adding another solvent in which the solute solubility is low. The concentration can be increased by evaporating solvent or by causing reactive formation of solute in the solution. Following the formation of supersaturated solutions, An understanding for the nucleation process can be provided through classical nucleation theory (CNT)[17–22] in which dissolved solute molecules begin to cluster together into organised nuclei. These nuclei have a lower free energy than that of the dissolved solutes, however there is a free energy penalty associated with the creation of the solution/nuclei interface. For a spherical nucleus the overall free energy ($\Delta G$) change between a small solute particles and the solute in solution can be expressed through equation 2.36:[18]

$$\Delta G = -\frac{4}{3}\pi r^3 \Delta G_v + 4\pi r^2 \sigma \tag{2.36}$$

In which $\Delta G_v$ is the free energy change for the phase transformation of solute to solid crystal, $r$ is the radius of the nucleus (m), $\sigma$ is the inter-facial tension between the crystal surface and the solution. The first term in equation 2.36 describes the driving force towards aggregation of the solute molecules which reduces the free energy, whilst the second term represents the free energy increase due to the creation of an interface. The respective negative and positive signs of these terms reflect the contribution to the overall free energy change. Inspecting this equation we see that for small crystal radii, the positive term dominates the expression. Consequently $\Delta G$ is positive, and these nuclei are unstable and may redissolve into the solution. As the radius of the crystal becomes larger, a value is eventually reached in which further increases in radius size results in a reduction of free energy. This value is known as the critical size ($r_c$). Continued growth of the nucleus will result in $\Delta G$ becoming negative and will be a stabilising process. If $\partial(\Delta G)/\partial r$ is set to equal 0, we find the critical radius can be calculated through; $r_c = \frac{-2\sigma}{\Delta G_v}$. Note that $\Delta G_v$ is a negative property. Figure 2.1 illustrates the free energy change during nucleation graphically.

The number of nuclei formed per unit volume and time is referred to as the nucleation rate (J) and can be expressed in the form of an Arrhenius reaction rate equation.

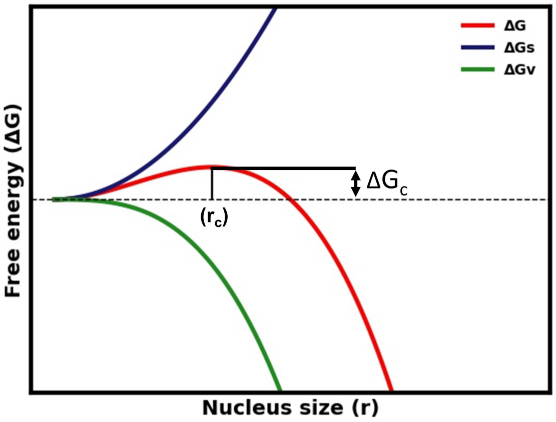

Figure 2.1: Graphical representation of the relationship between Free energy and nuclei size. $\Delta G$ is overall free energy change whilst $\Delta G_s$ & $\Delta G_v$ are the surface and phase transformation free energy respectively. The maximum value of $\Delta G$ occurs at the critical nucleus size ($r_c$). $\Delta G_c$ represents the barrier to nucleation.

The equation for $\Delta G_c$ can be obtained by substituting $r_c$ for $r$ in equation 2.36

$$J = A\, exp\left(\frac{\Delta G_c}{kT}\right) \tag{2.37}$$

Where $k$ is the Boltzmann constant ($R/N_a$, where $N_a$ is Avogadro constant) and $\Delta G_c$ can be considered as the barrier for nucleation.[18, 22, 23] To accurately predict the free energy associated with nucleation, the influence of inter-facial curvature must be considered. One method of doing this is through the inclusion of the Gibbs-Thomson relation.[24, 25] This modifies the solubility predicted by equilibrium thermodynamics through accounting for particle size. the Gibbs-Thomson effect is shown in equation 2.38. It is seen that for the case of a solution in which the excess solute particles are very small that solubility maybe be significantly higher than the equilibrium saturation value. For most aqueous solutions however, this effect is considered negligible for particle sizes greater than 1 micron.[18]

$$C_r = C^* \; exp\left(\frac{2\sigma V}{rRT}\right) \tag{2.38}$$

By substituting $r_c$ for r in equation 2.36 the critical Gibbs Free energy can be expressed through:

$$\Delta G_c = \frac{16\pi\sigma^3}{3(\Delta G_v)^2} \tag{2.39}$$

We can express $\Delta G_v$ as $\frac{-2\sigma}{r_c}$. Relating to equation 2.38:

$$\Delta G_v = \frac{kTln(S)}{v} \tag{2.40}$$

and finally inserting this into 2.37:

$$J = A \; exp\left[\frac{-16\pi\sigma^3 V^2}{3k^3T^3(lnS)^2}\right] \tag{2.41}$$

Where $V$ is the molar volume, R is the gas constant, $C_r$ is the solubility for particles of size r, and $C^*$ is the bulk solubility. S is supersaturation which is related to the solubility concentrations as $C_r/C^*$. The pre-exponential factor, $A$, is related to the rate of solute attachment to the critical nucleus.[19] As this is a function of molecular mobility in solution, it is highly temperature dependent. In practice, equation 2.41 is difficult to use as A and $r_c$ are typically unknown. By substituting in the constant $B$ as $\frac{16\pi\gamma^3V^2}{3K^3T^3}$ we obtain the simplified nucleation rate (equation 2.42). The constants $A$ and $B$ can then be estimated through fitting to experimental primary nucleation measurements.[26, 27]

$$J = A \; exp\left(\frac{B}{(lnS)^2}\right) \tag{2.42}$$

In the derivation of CNT, several simplifying assumptions are made. These include; the critical nuclei are taken as spherical droplets with physical properties identical to that of the macro-scale crystalline phase[18] and the surface of nuclei is modelled as an infinite plane with the effect of surface curvature on surface tension ($\gamma$) neglected.[28] Additionally, CNT assumes that growth of clusters occurs through the addition of single monomers, in which the ordering of the molecules within the nucleus reflects that of the nucleated crystal.

As a consequence of these assumptions CNT can fail to adequately provide a accurate representation of the nucleation process. For example, if polymorphism is exhibited for a particular system, the form of the initial nucleated crystal is likely to be the least stable form, closest in free energy to the original state in solution. Successive steps will then lead to formation of the stable crystal. The system thus takes path that minimises the free energy barrier to nucleation. This is known as the Ostwald step rule.[29, 30] Furthermore, the molecular organisation of the cluster/nuclei in solution does not necessarily need to have the same structure as the nucleated crystal.[17] With these limitations in mind, CNT does not necessarily capture a quantitative or qualitative description of many crystallisation systems but can provide basic insight into Crystal nucleation processes.

An alternative to CNT is the non-classical or two-step nucleation mechanism[17, 22, 31] where it is suggested that fluctuations in solute density lead to the formation of a highly concentrated, but disorganised droplet within the solution. This is is followed by structural organisation of nucleus with in the droplet, producing a nucleus above the critical size. The crystalline phase nucleates over time after these droplets are formed. Whilst the two-step nucleation mechanism can capture qualitative phenomena occurring in some systems, there has not been a generally accepted model for corresponding nucleation kinetics similar to that for CNT.

## 2.6 Solution non-ideality in anti-solvent crystallisation

The previous section discussed the nucleation process, and it was mentioned that supersaturation was a requirement for nucleation to occur. Crystallisation processes therefore aim to generate supersaturation throughout the system. This can achieved through lowering the solubility of a solute in a given solvent through either temperature reduction (cooling crystallisation) or the addition of a third solvent in which solute solubility is poor (anti-solvent crystallisation). This section will provide an overview of the latter, anti-solvent crystallisation.

Anti-solvent crystallisation relies on the solution non-ideality of the solution, and therefore it is first appropriate to discuss how ideal solutions are defined. In ideal solutions, interactions between solvent and solute molecules are assumed to be identical to that of the solvent molecules themselves. Additionally molecules of anti-solvent and solvent are assumed to behave identically as well. For ideal solutions, solubility can be estimated using the vant Hoff equation[32] (shown in equation 2.43).

$$ln(x) = \frac{\Delta H_f}{R}\left(\frac{1}{T_f} - \frac{1}{T}\right) \tag{2.43}$$

In which $x$ is the mol fraction of solute in solution, $T$ and $T_f$ are the solution and solute fusion temperature respectively (K), R is gas constant (8.314 $Jmol^{-1}K^{-1}$) and $\Delta H_f$ is the heat of fusion of the solute ($Jmol^-1$). The vant Hoff equation considers interactions between each different species as the equivalent of like-species, and consequently solvent composition has no effect on solubility. If the ideal solution model was applied to anti-solvent crystallisation, then we would predict that there would be no solubility change when the solvent and anti-solvent were mixed together. As a result no supersaturation would be generated and nucleation would not occur.

In reality, molecules of different species interact in a different manner than those of molecules of its on species. In the case of anti-solvent crystallisation, solute-anti-solvent interactions are far less favourable then solute-solution interactions. This results in deviations from ideal behaviour and the vant Hoff equation fails to represent the solute solubility. Figure 2.2 compares ideal solution solubility and experimental solubility as a function of composition for glycine in water/ethanol solvent mixtures. Note that we consider an isothermal solution at 298K.

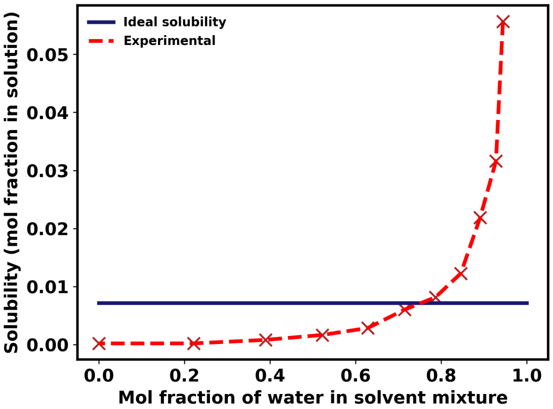

Figure 2.2: Comparison of experimental solubility and that predicted by the vant Hoff equation for ideal solution. Solubility given for a temperature of 298K. Both experimental solubility[33, 34] and Glycine thermodynamic properties for use in vant Hoff equation[35] taken from literature.

Figure 2.2 highlights the inherent non-ideality of anti-solvent processes. As anti-solvent fraction in the solvent mixture increases, solubility is seen to rapidly decrease due to the incompatibility of the solute molecule in anti-solvent. The decrease in solubility is caused by the increase in free energy of the solute due to interactions with the anti solvent molecules.

With molecule interactions forming the main principle behind anti-solvent crystallisation, it becomes necessary to model such processes as non-ideal solutions. One approach to including non-ideal effects is through the inclusion of an activity coefficients. In which the activity coefficient defined as $\gamma x$, where $\gamma$ is activity and $x$ is solute molar concentration in solution. For further explanation see section 4.2. The activity model used is detailed in chapter 3, section 2 (3.2)

## 2.7 On the role of diffusion in anti-solvent crystallisation

Crystallisation kinetics, and especially crystal nucleation, are driven by the local solution composition and the corresponding supersaturation and are thus strongly dependent on the composition heterogeneity. Accordingly, mixing plays a crucial role in the efficiency of crystallisation processes. This is particularly true for for anti-solvent crystallisation. Although in industrial processes the main mixing mechanism is turbulent, turbulent mixing can be subdivided into three cascading mechanisms; macro-mixing, meso-mixing and micro-mixing. Macro-mixing refers to the dispersion of fluids at a large scale within a vessel, facilitated by mean velocity fields. The mean velocity fields rearrange fluid elements spatially, whilst the concentrations of individual species remain unchanged within each element. In this way, macro-mixing controls the fluid element concentrations in which micro-mixing takes place, and moves these elements to different regions within the vessel, in which turbulent properties vary.[36]

These fluid elements are reduced to the Kolmogorov scale through turbulent dispersion. The Kolmogorov length (Lk) scale refers the smallest eddy length scale in turbulent flow below which viscous forces dominate mixing. Further reduction to the Bachelor scale by viscous deformation occurs in which the diffusion process is accelerated. The Batchelor length scale (Lk) describes the smallest length scales below which diffusive mixing becomes dominant. That is the time scales for molecular diffusion to homogenise fluid element compositions are significantly faster then further length scale reductions of fluid elements through viscous deformation. These length scales are discussed in greater detail in chapter 5 section 4.5 (section 5.4.). As turbulent processes eventually result in sub-bachelor scale fluid elements, diffusion therefore plays a crucial role in determining the efficiency of anti-solvent crystallisation processes, even in conditions characterised by turbulent mixing. With diffusion controlling the final nucleation environment, a better understanding of mixing related phenomena is required. For example, diffusive mixing can give rise to localised thermodynamically unstable compositions and local liquid-liquid phase separation.[33, 37–39] This can lead to the potential of micro-environments in which nucleation conditions differ from bulk conditions, especially in terms of solvent compositions. This can further complicate the control of crystallisation processes.

Recent developments in microfluidic platforms, where mixing is diffusion dominated has allowed for experimental observation on the effect of diffusive mixing on nucleation processes.[40, 41] Whilst a variety of modelling approaches to simulate diffusive mixing have been used within the literature, investigation of diffusive mixing applied within the anti-solvent crystallisation has been limited. In the previous studies,[42, 43] diffusive mixing is described within a Fickian framework, where concentration gradients are used as the driving force, with intuitions developed based on this. However, the driving force for diffusion are more physically rooted in chemical potential gradients, and non-ideal thermodynamic solution behaviour needs to be taken into account.[9] Hence, Fickain descriptions can fail to predict to the behaviour of the solute within the anti-solvent solution mixture. One expectation would be that the solute would not so freely diffuse into the anti-solvent, as this would increase the chemical potential of the solute. Instead, one would expect the movement of the solute towards the anti-solvent to be severely hindered by chemical potential gradients within the system. Moreover, the solute may retreat further into the solution to avoid the anti-solvent/solution interface. The first part of this thesis aims to apply a thermodynamically consistent diffusion model to anti-solvent systems based on the multi-component Maxwell-Stefan framework. This will provide insight and further understanding into the diffusive mixing in anti-solvent processes and assist in development, scale up, and control of such processes.

## 2.8 References

[1] Thomas Graham. On the law of the diffusion of gases. *Trans. R. Soc. Edinburgh*, 2:175–190,269–276,351–358, 1833.

[2] Thomas Graham. On the motion of gases. *Philos. Trans. R. Soc. Lond., B, Biol. Sci*, 136:573–671, 1845.

[3] Thomas Graham. On the molecular mobility of gases. *Proc. R. Soc. Lond*, 12:611–623, 1862.

[4] Thomas Graham. The bakerian lecture: On the diffusion of liquids. *Philos. Trans. R. Soc. Lond., B, Biol. Sci*, 140:1–46, 1850.

[5] Adolf Fick. Über diffusion (about diffusion). *Ann Phys*, 170:59–86, 1850.

[6] Oleg Medvedev. *Diffusion Coefficients in Multi-Component Mixtures.* PhD thesis, Technical University of Denmark, 2005.

[7] E. L. Cussler and E. L. Cussler. *Multicomponent Diffusion.* Elsevier Science, 1976.

[8] R Krishna and J A Wesselingh. Review Article Number 50:The Maxwell-Stefan Approach to Mass Transfer. *Chem. Eng. Sci.*, 52(6):861–911, 1997.

[9] Rajamani Krishna. Uphill Diffusion in Multicomponent Mixtures. *Chem. Soc. Rev,*, 44(10):2812–2836, 2015.

[10] Dieter Bothe. *On the Maxwell-Stefan Approach to Multicomponent Diffusion*, pages 81–93. Springer Basel, Basel, 2011.

[11] James Maxwell. On the dynamical theory of gases. *Philos. Trans. R. Soc. Lond., B, Biol. Sci*, 157:49–88, 1867.

[12] Josef Stefan. Über das gleichgewicht und die bewegung, insbesondere die diffusion von gasgemengen (about the equilibrium and the movement, especially the diffusion of gas mixtures). *Sitzungsberichte Der Akademie Der Wissenschaften Mathematisch-Naturwissenschaftliche Klasse*, 63:63–124, 1871.

[13] Lars Onsager. Theories and problems of liquid diffusion. *Ann. N. Y. Acad. Sci*, 46(5):241–265, 1945.

[14] J. Wambui Mutoru and Abbas Firoozabadi. Form of multicomponent fickian diffusion coefficients matrix. *J. Chem. Thermodyn.*, 43(8):1192–1203, 2011.

[15] D G. Miller, V Vitagliano, and R Sartorio. Some comments on multicomponent diffusion: Negative main term diffusion coefficients, second law constraints, solvent choices, and reference frame transformations. *J. Org. Chem.*, 90(8):1509–1519, 1986.

[16] José M. Ortiz de Zárate and Jan V. Sengers. Frame-invariant fick diffusion matrices of multicomponent fluid mixtures. *Phys. Chem. Chem. Phys.*, 22:17597–17604, 2020.

[17] Jie Chen, Bipul Sarma, James M. B. Evans, and Allan S. Myerson. Pharmaceutical crystallization. *Cryst. Growth Des.*, 11(4):887–895, 2011.

[18] J. W. (John William) Mullin. *Crystallization.* Butterworth-Heinemann, Oxford, UK, 1961.

[19] Deniz Erdemir, Alfred Y. Lee, and Allan S. Myerson. Nucleation of crystals from solution: Classical and two-step models. *Acc. Chem. Res.*, 42(5):621–629, 2009.

[20] *Handbook of Industrial Crystallization.* Cambridge University Press, 3 edition, 2019.

[21] Isabelle Weissbuch, Meir Lahav, and Leslie Leiserowitz. Toward stereochemical control, monitoring, and understanding of crystal nucleation. *Cryst. Growth Des.*, 3(2):125–150, 2003.

[22] S. Karthika, T. K. Radhakrishnan, and P. Kalaichelvi. A review of classical and nonclassical nucleation theories. *Cryst. Growth Des.*, 16(11):6663–6681, 2016.

[23] Maria Lucia Briuglia. *Primary and Secondary Crystal Nucleation of Pharmaceutics.* PhD thesis, University of Strathclyde, 2005.

[24] David A Porter and Kenneth E Easterling. *Phase transformations in metals and alloys.* CRC press, 2009.

[25] Michel Perez. Gibbs–thomson effects in phase transformations. *Scr. Mater.*, 52(8):709–712, 2005.

[26] Clément Brandel and Joop H. ter Horst. Measuring induction times and crystal nucleation rates. *Faraday Discuss.*, 179:199–214, 2015.

[27] S. Auer and D , Frenkel. Prediction of absolute crystal-nucleation rate in hard-sphere colloids. *Nature*, 409:1020–1023, 2001.

[28] Ari Laaksonen and Ismo Napari. Breakdown of the capillarity approximation in binary nucleation: A density functional study. *J. Phys. Chem. B*, 105(47):11678–11682, 2001.

[29] R. A. Van Santen. The ostwald step rule. *J. Phys. Chem.*, 88(24):5768–5769, 1984.

[30] W. Z. Ostwald. The ostwald step rule. *Phys. Chem.*, 22:289, 1879.

[31] Roger J. Davey, Sven L. M. Schroeder, and Joop H. ter Horst. Nucleation of organic crystals—a molecular perspective. *Angew. Chem., Int. Ed.*, 52(8):2166–2179, 2013.

[32] J. H. Van't Hoff. *Etudes de dynamique chimique (Studies in Chemical Dynamics)*. Frederik Müller, 1884.

[33] J McGinty et al. Effect of process conditions on particle size and shape in continuous antisolvent crystallisation of lovastatin. *Crystals*, 10(10):1–17, 2020.

[34] R Miller, J Sefcik, and L Lue. Modeling Diffusive Mixing in Antisolvent Crystallization. *Cryst. Growth Des*, 22(4):2192–2207, apr 2022.

[35] Christoph Held, Luca F. Cameretti, and Gabriele Sadowski. Measuring and modeling activity coefficients in aqueous amino-acid solutions. *Ind. Eng. Chem. Res*, 50(1):131–141, 2011.

[36] J. Bałdyga and R. Pohorecki. Turbulent micromixing in chemical reactors — a review. *Chem. Eng. J. Biochem. Eng. J.*, 58(2):183–195, 1995.

[37] G Das et al. Time-Resolved X-ray Phase-Contrast Imaging (XPCI) of Nucleation and Crystal Growth in the Anti-Solvent Crystallization of Lovastatin. *ChemRxiv.*

[38] Z Meng, Y Huang, S Cheng, and J Wang. Investigation of oiling-out phenomenon of small organic molecules in crystallization processes: A review. *ChemistrySelect*, 5(26):7855–7866, jul 2020.

[39] E Deneau and G Se. An in-line study of oiling out and crystallization. *Org Process Res Dev*, 9(6):943–950, 2005.

[40] J Puigmartí-Luis. Microfluidic platforms: a mainstream technology for the preparation of crystals. *Chem. Soc. Rev.*, 43:2253–2271, 2014.

[41] H H Shi et al. Progress of crystallization in microfluidic devices. *Lab Chip*, 17(13):2167–2185, 2017.

[42] Michael R. Thorson et al. Microfluidic approach to polymorph screening through antisolvent crystallization. *CrystEngComm*, 14(7):2404, 2012.

[43] Venkateswarlu Bhamidi et al. Antisolvent Crystallization and Polymorph Screening of Glycine in Microfluidic Channels Using Hydrodynamic Focusing. *Cryst Growth Des.*, 15(7):3299–3306, 2015.

# Chapter 3

# Formulation of Diffusion model

## 3.1 Introduction

In chapters 4 & 5 diffusion in anti-solvent crystallisation is modelled with the methodology and simulation details provided within the respective chapters. With this in consideration, it is not the aim of this chapter to detail the application of the diffusion model, but rather to provide the derivation of the model.

## 3.2 Free energy model

Anti-solvent crystallisation is by definition highly non-ideal process and as such a free energy model is necessary to describe solution non-ideality, and to allow for diffusive mixing to be modelled based on physically correct driving forces; activity gradients. To represent the thermodynamics of anti-solvent systems the extended Scatchard-Hildebrand model,[1] which includes a Flory-Huggins term to account for the effect of asymmetry in the entropy of mixing in the standard regular solution model was used.[2] In this model, the Gibbs free energy takes the form:

$$\beta G = \sum_{i} x_i \left(\beta\mu_i^o + ln\varphi_i\right) + \frac{1}{2}\frac{\nu}{\nu_{ref}}\sum_{ij}\varphi_i\varphi_j\chi_{ij} \tag{3.1}$$

Where $\beta$ is $1/(RT)$, R is gas constant and T is the absolute temperature (K). $\nu$ is molar volume of the solution and is calculated through $\nu = \sum_{i=1}^{N} x_i v_i$ with $x_i$ and $v_i$ being the component molar fraction and 'effective component molar volume in solution respectively. The effective molar volume describes the species molar volume in a given solution mixture. The molar volume of solution is divided through by a reference volume. This is taken to be the molar volume of the solvent. The volume fraction ($\varphi$) of component i can then be calculated through $\frac{x_i v_i}{\nu}$. Note that is the volume fraction of component 'i' based on the effective molar volumes. To distinguish from volume fraction based on pure component volume ($\phi$), we assign effective volume fraction the symbol $\varphi_i$. $\chi_{ij}$ describes the interaction between species i and j and is known as the binary interaction parameter. A higher value represents greater extent on non-ideality between the two species, and physically represents the incompatibility between the species. That is, greater values of $\chi$, the greater tendency for components i and j to demix. These parameters are symmetric ($\chi_{ij} = \chi_{ji}$) and there is no interaction between like species ($\chi_{ii} = 0$).

The chemical potential $\mu_i$ of component $i$ can be written as:

$$\beta\mu_i = \beta\mu_i^\circ + \ln x_i + \ln\gamma_i \tag{3.2}$$

where $\gamma_i$ is the activity coefficient of $i$. The sum of the first two terms is the chemical potential of component $i$ in an ideal solution, while the final term represents the contribution of solution non-ideality. In an ideal solution, $\gamma_i = 1$ for all species.

The activity coefficient of species 'i' ($\gamma_i$) is defined as the partial molar property of component 'i' with respect to $\beta$G, i.e. the partial molar excess Gibbs energy of component i ($G_i$).[3] Equation 3.3 shows this definition.

$$ln(\gamma_i) = \beta G_i = \left(\frac{\partial(n\beta G)}{\partial n_i}\right)_{T,P,N_{J\neq i}} \tag{3.3}$$

Inserting equation 3.1 into equation 3.3 yields the generalised form of the activity coefficient of component i in a multi-component mixture:

$$\ln\gamma_i = \ln\frac{\varphi_i}{x_i} + \sum_j\left(1 - \frac{v_i}{v_j}\right)\varphi_j + \frac{v_i}{v_{\text{ref}}}\left(\sum_j \chi_{ij}\varphi_j - \frac{1}{2}\sum_{jk}\chi_{jk}\varphi_j\varphi_k\right). \tag{3.4}$$

In this work we deal with binary and ternary component systems and shown below are the corresponding activity coefficient equations. Note equation 3.4 can be easily expanded to an arbitrary N-component system.

**Activity coefficient for binary system:**

$$ln(\gamma_1) = ln\left(\frac{\varphi_1}{x_1}\right) + \left(1 - \frac{\nu_1}{\nu_2}\right)\varphi_2 + \frac{\nu_1}{\nu_{ref}}\chi_{12}\varphi_2^2 \tag{3.5}$$

**Activity coefficient for ternary system:**

$$ln(\gamma_1) = ln(\frac{\varphi_1}{x_1}) + \left(1 - \frac{\varphi_1}{x_1}\right) + \frac{\nu_1}{\nu_{ref}}\left[\chi_{12}\varphi_2^2 + \chi_{13}\varphi_3^2 + (\chi_{12} + \chi_{13} - \chi_{23})\,\varphi_2\varphi_3\right] \tag{3.6}$$

Equations 3.5 & 3.6 are then used to calculate the matrix of thermodynamic factors used in the Maxwell-Stefan formulation which represents the solution non-ideality of the system. The details of this are discussed in the following section along with the formulation of the diffusion model used in this work.

## 3.3 Supersaturation definition

The driving force for crystallisation is referred to as supersaturation. in ideal solutions, this is simply calculated by dividing the local solute concentration by the solubility at the local solvent composition. In non-ideal mixtures, such as those involved in anti-solvent mixtures, it is more appropriate to define supersaturation based on chemical potential. We consider the solubility curve of a typical anti-solvent system. Along the solubility curve, the chemical potential of the solute within the liquid mixture is the same as that for the pure crystalline solute, which leads to the relation:

$$x_0\gamma_0 = e^{\beta(\mu_0^s - \mu_0^\circ)} \tag{3.7}$$

where $\mu_0^s$ is the chemical potential of the pure solid solute.

The right side of Eq. (4.4) is independent of solution composition, and a solubility constant is defined as $\beta(\mu_0^s - \mu_0^\circ)$. Its value will be dependent upon the solute used, along with the temperature and pressure of the system. The left side of Eq. (4.4) is the activity of the solute. When it becomes larger than the right side of Eq. (4.4), the solution is supersaturated, and solutes will tend to crystallise from solution. We define the supersaturation ratio as $S = x_0\gamma_0 e^{-\beta(\mu_0^s - \mu_0^\circ)}$. When $S < 1$, the solution is under saturated, when $S = 1$, the solution is saturated, and when $S > 1$, the solution is supersaturated.

## 3.4 Derivation of diffusion model

In chapters 4 and 5 we model the diffusive mixing in ternary component anti-solvent crystallisation systems. Hence it is necessary to model multi-component diffusion in non-ideal solutions. To do this, the Maxwell-Stefan formulation is employed,[4] with the generalised multi-component form given below;

$$c_i \nabla \beta \mu_i = -\sum_j \frac{1}{Đ_{ij}} (x_j \mathbf{J}_i - x_i \mathbf{J}_j) \tag{3.8}$$

The ternary component form of Fickian form of the fluxes can be expressed as:

$$\begin{pmatrix} \mathbf{J}_1 \\ \mathbf{J}_2 \\ \mathbf{J}_3 \end{pmatrix} = -\frac{1}{\Delta} \begin{pmatrix} \frac{1-x_1}{Đ_{23}} & -\frac{x_1}{Đ_{13}} & -\frac{x_1}{Đ_{12}} \\ -\frac{x_2}{Đ_{23}} & \frac{1-x_2}{Đ_{13}} & -\frac{x_2}{Đ_{12}} \\ -\frac{x_3}{Đ_{23}} & -\frac{x_3}{Đ_{13}} & \frac{1-x_3}{Đ_{12}} \end{pmatrix} \begin{pmatrix} c_1 \boldsymbol{\nabla\beta\mu_1} \\ c_2 \boldsymbol{\nabla\beta\mu_2} \\ c_3 \boldsymbol{\nabla\beta\mu_3} \end{pmatrix} \tag{3.9}$$

where $\Delta$ is;

$$\Delta = \frac{x_1}{Đ_{12}Đ_{13}} + \frac{x_2}{Đ_{12}Đ_{23}} + \frac{x_3}{Đ_{13}Đ_{23}}$$

$Đ_{ij}$ represents the Maxwell-Stefan diffusion coefficient. The system to be modelled is a sealed liquid system, and there is minimal volume change upon mixing, molar volume can be considered constant. For convenience, velocity based on the volume reference frame is used.[5] Section 2.4 provides a detailed description of reference frames. The Maxwell-Stefan equations are in the molar reference frame, and the diffusivity $\mathbb{D}$ must be converted to the volume basis. This is achieved equation 2.35, which for a ternary component system gives;

$$\mathbb{D}^{\phi} = \begin{pmatrix} 1-\phi_1 & -\phi_1 V_2/V_1 & -\phi_1 V_3/V_1 \\ -\phi_2 V_1/V_2 & 1-\phi_2 & -\phi_2 V_3/V_2 \\ -\phi_3 V_1/V_3 & -\phi_3 V_2/V_3 & 1-\phi_3 \end{pmatrix} \mathbb{D}^{x} \tag{3.10}$$

Where $V_i$ is the pure component molar volume of species i. Note that this distinct from the adjusted molar volumes that are used in the free energy model. The corresponding fluxes in the volume reference frame is given by;

$$\begin{pmatrix} \mathbf{J}_1^{\phi} \\ \mathbf{J}_2^{\phi} \\ \mathbf{J}_3^{\phi} \end{pmatrix} = -\frac{1}{\Delta} \begin{pmatrix} \frac{1-\phi_1}{Đ_{23}} & -\frac{\phi_1 V_2}{Đ_{13}V_1} & -\frac{\phi_1 V_3}{Đ_{12}V_1} \\ -\frac{\phi_2 V_1}{Đ_{23}V_2} & \frac{1-\phi_2}{Đ_{13}} & -\frac{\phi_2 V_3}{Đ_{12}V_2} \\ -\frac{\phi_3 V_1}{Đ_{23}V_3} & -\frac{\phi_3 V_2}{Đ_{13}V_3} & \frac{1-\phi_3}{Đ_{12}} \end{pmatrix} \begin{pmatrix} c_1 \boldsymbol{\nabla\beta\mu_1} \\ c_2 \boldsymbol{\nabla\beta\mu_2} \\ c_3 \boldsymbol{\nabla\beta\mu_3} \end{pmatrix} \tag{3.11}$$

The gradients of chemical potential are related through the Gibbs-Duhem equation;

$$\sum_{\alpha} c_{\alpha} \nabla \beta \mu_{\alpha} = 0 \tag{3.12}$$

From equation 3.12 it is apparent for a ternary component system there is only is two independent fluxes. The flux of the third component ($J_1$) can be eliminated by making the substitution;

$$c_1 \nabla \beta \mu_1 = -c_2 \nabla \beta \mu_2 - c_3 \nabla \beta \mu_3 \tag{3.13}$$

The two independent fluxes are then calculated through;

$$\begin{pmatrix} \mathbf{J}_2^{\phi} \\ \mathbf{J}_3^{\phi} \end{pmatrix} = - \begin{pmatrix} \mathbb{D}_{22}^{\phi} - \mathbb{D}_{21}^{\phi} & \mathbb{D}_{23}^{\phi} - \mathbb{D}_{21}^{\phi} \\ \mathbb{D}_{32}^{\phi} - \mathbb{D}_{31}^{\phi} & \mathbb{D}_{33}^{\phi} - \mathbb{D}_{31}^{\phi} \end{pmatrix} \begin{pmatrix} c_2 \boldsymbol{\nabla \beta \mu_2} \\ c_3 \boldsymbol{\nabla \beta \mu_3} \end{pmatrix}$$

And equation 3.11 is reduced to;

$$\begin{pmatrix} \mathbf{J}_2^{\phi} \\ \mathbf{J}_3^{\phi} \end{pmatrix} = -\frac{1}{\Delta} \begin{pmatrix} \dfrac{(1-\phi_2)\,V_2}{\text{Đ}_{13}} + \dfrac{\phi_2 V_1}{\text{Đ}_{23}} & -\phi_2 \left( \dfrac{V_3}{\text{Đ}_{12}} - \dfrac{V_1}{\text{Đ}_{23}} \right) \\ -\phi_3 \left( \dfrac{V_2}{\text{Đ}_{13}} - \dfrac{V_1}{\text{Đ}_{23}} \right) & \dfrac{(1-\phi_3)\,V_3}{\text{Đ}_{12}} + \dfrac{\phi_3 V_1}{\text{Đ}_{23}} \end{pmatrix} \begin{pmatrix} c_2 \boldsymbol{\nabla \beta \mu_2} \\ c_3 \boldsymbol{\nabla \beta \mu_3} \end{pmatrix} \tag{3.14}$$

It is inconvenient to work in chemical potential, and it is useful to express these as volume fraction gradients by introducing an (N-1) x (N-1) of matrix of thermodynamic factors, ($\Gamma_{ij}$).

$$\Gamma_{ij} = c_i \frac{\partial \beta \mu_i}{\partial \phi_j}. \tag{3.15}$$

$\Gamma_{ij}$ can be calculated by inserting the free energy model given in section 3.2. The final form of the model used in this work is given below:

$$\begin{pmatrix} \mathbf{J}_2^{\phi} \\ \mathbf{J}_3^{\phi} \end{pmatrix} = -\frac{1}{\Delta} \begin{pmatrix} \dfrac{(1-\phi_2)\,V_2}{Đ_{13}} + \dfrac{\phi_2 V_1}{Đ_{23}} & -\phi_2 \left( \dfrac{V_3}{Đ_{12}} - \dfrac{V_1}{Đ_{23}} \right) \\ -\phi_3 \left( \dfrac{V_2}{Đ_{13}} - \dfrac{V_1}{Đ_{23}} \right) & \dfrac{(1-\phi_3)\,V_3}{Đ_{12}} + \dfrac{\phi_3 V_1}{Đ_{23}} \end{pmatrix} \begin{pmatrix} \Gamma_{11} & \Gamma_{12} \\ \Gamma_{21} & \Gamma_{22} \end{pmatrix} \begin{pmatrix} \boldsymbol{\nabla \phi_2} \\ \boldsymbol{\nabla \phi_3} \end{pmatrix} \tag{3.16}$$

In which the $\Gamma$ matrix entries are defined as follows;

$$\Gamma_{11} = \frac{1}{v_2} + \varphi_2 \left( \left( \frac{1}{v_1} - \frac{1}{v_2} \right) + (\chi_{12} + \chi_{13} - \chi_{23})\,\varphi_3 - 2\chi_{12}\,(1-\varphi_2) \right)$$

$$\Gamma_{12} = \varphi_2 \left( \left( \frac{1}{v_1} - \frac{1}{v_3} \right) + (\chi_{23} - \chi_{12} - \chi_{13})\,(1-\varphi_2) + 2\chi_{13}\varphi_3 \right)$$

$$\Gamma_{21} = \varphi_3 \left( \left( \frac{1}{v_1} - \frac{1}{v_2} \right) + (\chi_{23} - \chi_{12} - \chi_{13})\,(1-\varphi_3) + 2\chi_{12}\varphi_2 \right)$$

$$\Gamma_{22} = \frac{1}{v_3} + \varphi_3 \left( \left( \frac{1}{v_1} - \frac{1}{v_3} \right) + (\chi_{12} + \chi_{13} - \chi_{23})\,\varphi_2 - 2\chi_{13}\,(1-\varphi_3) \right)$$

In above equations, nomenclature match the symbols previously defined. Note that $\phi$ is used in diffusion model, and $\varphi$ is used in activity model to distinguish these values. The diffusive model uses pure component molar volumes, whilst in the activity model these are taken as fitted parameters and do not necessarily equal the pure component molar volumes.

## 3.5 Comments on model assumptions

It was assumed that M-S diffusion coefficients are independent of composition. Ternary Fickian coefficients for our anti-solvent system had not been previously measured in literature, and the approach chosen calculates these through a weighted average of the binary MS values. A reason for taking these values to be composition independent is due to the complexity in determining how the binary coefficient varied with composition in a ternary component mixture. Furthermore, the chosen approach includes thermodynamic correction factor in the diffusivity matrix. This allows for the composition of the ternary component system to be accounted for in the calculation of ternary diffusion coefficient.

The sensitivity of the predicted diffusive profiles on the selected diffusion coefficient values was determined through a parametric study on binary coefficients. Discussed in section 4.5.4. The results of this study indicated that whilst there are quantitative differences in calculated profiles, there were no qualitative differences found. For all combinations, there was no overshoot in supersaturation at the anti-solvent/solution interface as expected from intuition. Glycine was found to diffuse 'uphill' of its concentration gradient in all cases, highlighting importance of modelling chemical potential gradients as opposed to concentration. Therefore, that while the choice of binary diffusion coefficients effect quantitative mixing profiles, the main conclusions and outcomes of this work are independent of these values.

Similarly, to ternary diffusion coefficients, volume of mixing for our ternary component system was not available. Thus, the addition of this would complicate modelling efforts. With respect to binary system of water/ethanol, the maximum volume change upon mixing is -5%.[6] The small volume changes would not be expected to change mixing profiles significantly. Additionally, with driving force modelled as chemical potential, whilst exact diffusive composition trajectories might differ slightly, inclusion of small volume changes upon mixing would unlikely alter the conclusions found in this work.

## 3.6 References

[1] E Wilhelm. Mitigating Complexity: Cohesion Parameters and Related Topics. I: The Hildebrand Solubility Parameter. *J Solution Chem*, 47(10):1626–1709, 2018.

[2] T Lindvig, M L Michelsen, and G M Kontogeorgis. Fluid phase equilibria. 203:247–260, 2002.

[3] E Wilhelm. Solubilities, fugacities and all that in solution chemistry. *J Solution Che*, 44:1004–1061, 2015.

[4] R Krishna. Uphill Diffusion in Multicomponent Mixtures. *Chem. Soc. Rev,*, 44(10):2812–2836, 2015.

[5] D G. Miller, V Vitagliano, and R Sartorio. Some comments on multicomponent diffusion: Negative main term diffusion coefficients, second law constraints, solvent choices, and reference frame transformations. *J. Org. Chem.*, 90(8):1509–1519, 1986.

[6] J.-P.E. Grolier and E Wilhelm. Excess volumes and excess heat capacities of water + ethanol at 298.15 k. *Fluid Phase Equilib*, 6(3):283–287, 1981.

# Chapter 4

# Diffusive Mixing in Anti-solvent Crystallisation

## 4.1 Introduction

Mass transfer phenomena play an important role in many chemical and physical processes, such as crystallisation, and, therefore, it is essential to develop a better fundamental understanding of mass transfer effects in order to design more efficient crystallisation processes. This paper focuses on the molecular diffusion aspect of mass transfer and on diffusive mixing in the context of anti-solvent crystallisation. This is a commonly employed crystallisation process, in which the solute is crystallised from solution via the addition of a secondary solvent with poor solute solubility (anti-solvent). The solubility in the resulting mixture is significantly lowered and crystallisation of the solute is induced. Anti-solvent crystallisation offers flexibility in terms of acquiring the desired supersaturation profiles through addition of a selected anti-solvent to the solution. Multiple techniques are available to perform anti-solvent addition allowing for further control over the mixing process. These include continuous static mixers or the injection of the anti-solvent into a vessel containing the solution or vice versa.[1–3]

The development of effective crystallisation processes requires careful thought of process parameters. For anti-solvent processes these include initial solute concentration in the solution, anti-solvent composition, anti-solvent addition rate and mixing regime. To assist in the selection of these parameters, a modelling approach can be taken to provide insight into effects of these parameters on crystallisation outcomes. Models can be developed to simulate the mixing process, and mixing models can be further combined with population balance models to develop integrated process models of anti-solvent crystallisation processes.[4]

Thermodynamically, the driving force for crystallisation is the chemical potential difference between the solid phase and the solution. In crystallisation, the driving force is generally expressed as supersaturation. Crystal nucleation and growth rates are sensitive functions of supersaturation, and therefore the resulting crystal properties such as solid form, crystal size distribution and shape are strongly influenced by supersaturation.[5] During the mixing process during anti-solvent addition, the composition of the system is not uniform and regions of high supersaturation are intuitively expected to exist, where the local supersaturation can exceed the final supersaturation value corresponding to the fully mixed solution. Nucleation would be more likely to occur in these localised regions of high supersaturations and different solvent compositions than under prevailing conditions in the fully mixed solution. Furthermore, the crystals produced may have solid forms differing from those expected. Local composition profiles are controlled via the mixing process, and therefore an effective control of mixing is required for the design and operation of efficient anti-solvent crystallisation processes.[2]

Mixing can occur via two main mechanisms: diffusive and advective. Diffusion can be seen as mixing at a molecular level and occurs via random thermal motion, while advection is mixing at a bulk scale. The Peclet number is a dimensionless number that characterises the ratio of convective to diffusive mixing and is expressed through $\mathrm{Pe} = Lu/D$, where $L$ is a characteristic length, $u$ is a local fluid velocity, and $D$ is diffusion coefficient. If the Peclet number is much less than unity, then mass transfer is considered diffusion dominated. Recently, applications of microfluidic crystallisation have seen increased interest due to the high level of control offered.[6] With length scales in microns, mixing can occur under conditions of free inter-facial diffusion, resulting in strict control over supersaturation profiles and hence crystal properties. For Peclet number significantly greater than one, mixing is governed by two sequential processes, fluid bulk motion and molecular diffusion.[7] Fluid motion acts to rearrange the spatial location of fluid elements, with the concentration of each species remaining unchanged within the element. Exchange of species between neighbouring elements occurs via molecular diffusion and at sufficiently small length scales, mixing becomes dominated by diffusion.

A variety of modelling approaches to simulate diffusive mixing have been used within the literature, however investigation of diffusive mixing applied within the anti-solvent crystallisation has been very limited. In a study on applications of microfluidics to polymorphic screening during anti-solvent crystallisation,[8] the diffusive mixing during the anti-solvent crystallisation process was modelled using a Fickian approach assuming thermodynamically ideal solutions. Insights obtained from this modelling were qualitatively compared to experimental observations on crystallisation in microfluidic wells composed of two adjacent chambers, one with filled with anti-solvent and the other with an indomethacine solution, where diffusive mixing occurred at the interface between the two chambers. The wells allowed for various ratios of anti-solvent to solution to be used, and the effect on nucleation outcomes were investigated. It was concluded that the development of the spatiotemporal supersaturation profiles plays a key role in the formation of crystals, in terms of both properties and location of crystallisation, although relationships between calculated supersaturation profiles and observed nucleation outcomes were not straightforward.

In a later study,[9] a continuous microfluidic platform was used in the polymorphic screening of glycine. Glycine was crystallised through anti-solvent crystallisation in which diffusive mixing takes place at laminar flow interfaces. The mixing process was modelled by solving the steady-state Navier-Stokes equation to obtain the velocity profile of the streams, which was then inserted into the steady-state convective-diffusive equation, again using a Fickian approach assuming thermodynamically ideal solutions. This approached was used to calculate the concentration and supersaturation profiles of the microfluidic channel. The model prediction showed a wide variation in the local supersaturation throughout the channel, including significant overshoots above supersaturation of the final mixed solution. This would then imply the possible formation of several different glycine polymorphs, where both $\alpha$- and $\beta$-glycine were observed in corresponding experiments.

In the previous studies, diffusive mixing is described within a Fickian framework, where concentration gradients are used as the driving force, with intuitions developed based on this. However, the driving force for diffusion are more physically rooted in chemical potential gradients, and non-ideal thermodynamic solution behaviour needs to be taken into account.[10] For example, the solute would not be expected to diffuse into the anti-solvent, as this would be against the thermodynamic driving force, while it would be allowed in the Fickian diffusion framework.

In this work, multi-component diffusion is modelled within the Maxwell-Stefan framework, where diffusion is driven through chemical potential gradients.[10] To study diffusive mixing in anti-solvent crystallisation, ternary solutions of glycine (0), water (1), and ethanol (2) are considered. Glycine is the solute, water is the solvent, and ethanol or a mixture of ethanol/water is used as the anti-solvent. This specific anti-solvent crystallisation system was chosen because it is well studied experimentally in the literature and thermodynamic data are readily available. Furthermore, this system is representative of typical anti-solvent systems, placing this work in the wider context of anti-solvent particle formation processes. Composition and supersaturation profiles will be calculated across diffusion interfaces and ternary phase diagrams. While crystallisation as such is not modelled in this work, relationships between process parameters and crystallisation outcomes can be inferred from the corresponding supersaturation profiles. A comparison will be made between diffusive mixing in ideal and non-ideal solutions, revealing qualitative differences in their respective behaviours and challenging previous intuitions based on a Fickian framework. This work provides novel insights into the role of activity gradients in diffusive mixing during anti-solvent crystallisation which will assist in the development and design of more efficient crystallisation processes.

The remainder of this chapter is organised as follows. In the following chapter sections, we present the free energy model used to describe the solution thermodynamics of the system and its parameterisation. In 4.3, the details of the Maxwell-Stefan diffusion model are presented, and the parameters of the model, such as the mutual diffusion coefficients, are determined. The details of the diffusion simulations are provided in chapter 4.4. Chapter 4.5 then compares the results between ideal solutions, where diffusion is driven by concentration gradients, and non-ideal solutions, where diffusion is driven by chemical potential gradients. Finally, the main findings of the work are summarised in the chapter conclusions ( 4.6).

## 4.2 Thermodynamics of glycine/water/ethanol/mixtures

### 4.2.1 Thermodynamic model

The extended Scatchard-Hildebrand model,[11] which includes the effect of size asymmetry in the entropy of mixing in the standard regular solution model,[12] is used to describe the thermodynamics of the ternary water/ethanol/glycine mixtures. The molar Gibbs free energy $G$ is given by:

$$\beta G = \sum_i x_i \left(\beta \mu_i^\circ + \ln \varphi_i\right) + \frac{1}{2} \frac{v}{v_{\mathrm{ref}}} \sum_{ij} \varphi_i \varphi_j \chi_{ij} \tag{4.1}$$

where $\mu_i^\circ$ is the chemical potential of pure component $i$ in the liquid state at the system temperature, $\beta = 1/(RT)$, $R$ is the gas constant, $T$ is the absolute temperature, $v_{\mathrm{ref}}$ is the reference volume (which we will take to be the solvent volume), $v = \sum_{i=1}^{N} x_i v_i$ is the molar volume of the solution, $x_i$ and $v_i$ are the mole fractions and effective component molar volume, respectively, $\varphi_i = x_i v_i / v$ is the volume fraction of species $i$, and $\chi_{ij}$ is a binary interaction parameter between species $i$ and $j$. The binary interaction parameters are symmetric (i.e. $\chi_{ij} = \chi_{ji}$), and $\chi_{ii} = 0$. Physically, they represent the incompatibility between species; the larger the value of $\chi_{ij}$, the greater the tendency for components $i$ and $j$ to demix. The effective molar volumes $v_i$ and the binary interaction $\chi_{ij}$ are taken as adjustable parameters of the thermodynamic model and are obtained by fitting available experimental data. The ideal solution model corresponds to the situation where all the species volumes $v_i$ have the same value and the binary interactions $\chi_{ij}$ are equal to zero.

The chemical potential $\mu_i$ of component $i$ can be written as:

$$\beta\mu_i = \beta\mu_i^\circ + \ln x_i + \ln\gamma_i \tag{4.2}$$

where $\gamma_i$ is the activity coefficient of $i$. The sum of the first two terms is the chemical potential of component $i$ in an ideal solution, while the final term represents the contribution of solution non-ideality. In an ideal solution, $\gamma_i = 1$ for all species. In the extended Scatchard-Hildebrand model, the corresponding expression for the activity coefficient of component $i$ in a multi-component mixture:

$$\ln\gamma_i = \ln\frac{\varphi_i}{x_i} + \sum_j\left(1 - \frac{v_i}{v_j}\right)\varphi_j + \frac{v_i}{v_{\mathrm{ref}}}\left(\sum_j \chi_{ij}\varphi_j - \frac{1}{2}\sum_{jk}\chi_{jk}\varphi_j\varphi_k\right). \tag{4.3}$$

Along the solubility curve, the chemical potential of glycine in the liquid mixture is the same as that for pure crystalline glycine, which leads to the relation

$$x_0\gamma_0 = e^{\beta(\mu_0^s - \mu_0^\circ)} \tag{4.4}$$

where $\mu_0^s$ is the chemical potential of pure solid glycine.

The right side of Eq. (4.4) is independent of solution composition, and a solubility constant is defined as $\beta(\mu_0^s - \mu_0^\circ)$. This constant and the glycine/ethanol binary interaction parameter (i.e. $\chi_{02}$) were fitted to solubility data for glycine in water/ethanol solvent mixtures. The solubility data used were a combination of literature values[2] and solubility measured in this work.

The left side of Eq. (4.4) is the activity of glycine. When it becomes larger than the right side of Eq. (4.4), the solution is supersaturated, and glycine will tend to crystallise from solution. We define the supersaturation ratio as $S = x_0\gamma_0 e^{-\beta(\mu_0^s - \mu_0^\circ)}$. When $S < 1$, the solution is under saturated, when $S = 1$, the solution is saturated, and when $S > 1$, the solution is supersaturated.

### 4.2.2 Fitted model parameters

For a ternary solution, there are three binary interaction parameters. The glycine/water interaction parameter $\chi_{01}$ and glycine volume relative to water $v_0/v_1$ were fitted to vapour pressure measurements for glycine/water mixtures.[13] Values for the binary interaction $\chi_{12}$ and ethanol volume with respect to water $v_2/v_1$ were obtained by fitting experimental VLE data for water/ethanol mixtures,[14–16] across a wide composition range. The fits of the thermodynamic model are shown in Figs. 4.1(a) and (b). For both cases, the activity model fits the data well, and a reasonable estimate of the the parameters was obtained.

Measurements were performed using gravimetric analysis to obtain accurate solubility data for glycine in water-ethanol mixtures, which are required to parameterise the thermodynamic model used in this work. Glycine ($\geq$ 99%) was sourced from Sigma Aldrich, ethanol ($\geq$ 99.8%) was supplied by VWR. De-ionised water was used to prepare the aqueous glycine solution. Slurries of glycine in water/ethanol mixtures were added to 8 mL vials containing magnetic stirrer bars and the vials were placed on a submersible stirrer plate in a water bath set to 25°C. The stirring speed was set to 700 rpm. At least 3 vials for each solvent composition were used, with more vials used for solvent mixtures containing low amounts of water, to ensure results were reproducible. The vials were left for 72 hours to allow the slurry to reach equilibrium. After 72 hours, a syringe was used to withdraw 2 mL of the clear mother liquid and inject into an empty pre-weighed vial. A syringe filter was used to ensure no undissolved glycine was transferred into the new vial. The new vials containing the clear mother liquor were placed in a vacuum oven to evaporate the solvent. Once all solvent had been evaporated, the mass of glycine was determined and the solution concentration was calculated from material balances.

The measured solubilities, together with data previously reported in the literature,[2, 16–19] are shown in Fig. 4.1(c). The solubility measured in this work (green squares) is in a good agreement with the literature values.

Some variation of solubility was observed at low water mass fractions in the solvent mixture, as highlighted in Fig. 4.1(d). This is due to the challenges associated with measuring the extremely low glycine concentrations in mixtures with little water content. The glycine/ethanol interaction parameter $\chi_{02}$ and the solubility constant $\beta(\mu_0^s - \mu_0^\circ)$ were determined by fitting the solubility of glycine in water/ethanol solvent mixtures measured in this work. The red dotted line shows the predictions of the fitted thermodynamic model.

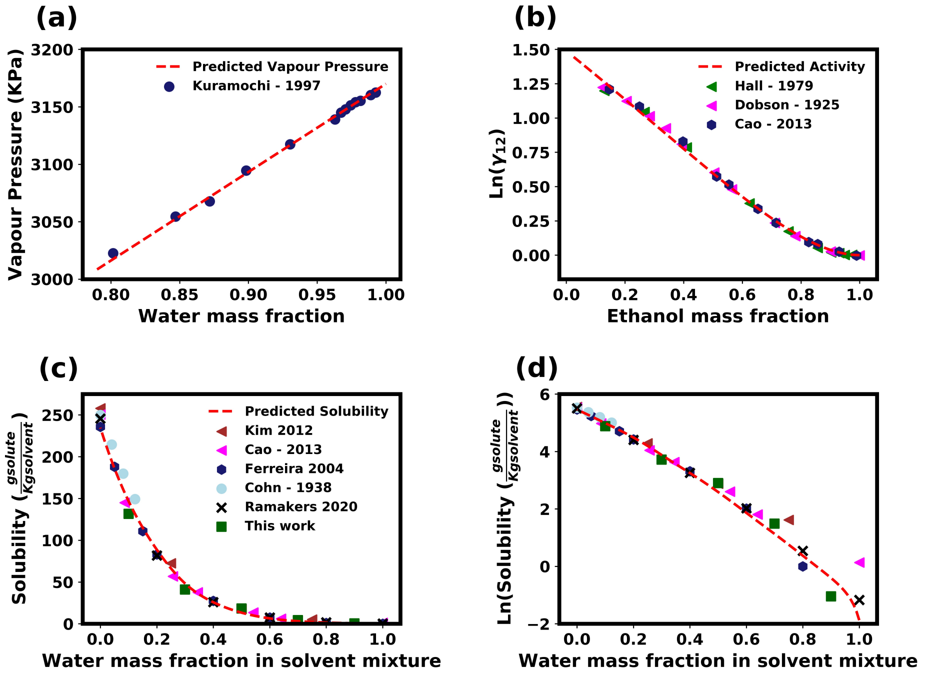

Figure 4.1: (a) Comparison of the predicted vapour pressure with measurements from the literature for water/glycine binary system. (b) Predicted activity coefficient of ethanol in water/ethanol mixtures compared to values derived from experimental VLE data taken from literature. (c) Solubility of glycine in water/ethanol mixtures as predicted by the thermodynamic model at 298 K. Green squares show the solubility measured in this work through gravimetric analysis. (d) Solubility shown on a logarithmic scale.

Table 4.1: Values of the parameters used in the thermodynamic model.

| Parameter | | Value |
|---|---|---|
| water/glycine binary interaction parameter | $\chi_{01}$ | 0.59 |
| ethanol/glycine binary interaction parameter | $\chi_{02}$ | 2.075 |
| water/ethanol binary interaction parameter | $\chi_{12}$ | 1.07 |
| solubility constant | $\beta(\mu_0^s - \mu_0^\circ)$ | $-2.2$ |
| glycine relative volume | $v_0/v_1$ | 3.58 |
| ethanol relative volume | $v_2/v_1$ | 1.50 |

The values of the fitted parameters used in the thermodynamic model are summarised in Table 4.1. The ternary phase diagram for our system can be calculated from the free energy model (i.e. Eq . (4.1) with parameters given in Table 4.1).

The requirement for phase stability is that the eigenvalues of the thermodynamic factor ($\Gamma$, discussed in chapter 2.3) must be positive (i.e. $\det \Gamma > 0$).[10] This property was used to determine compositions where the solution is predicted to be unstable. The binodal curve is determined by equating the chemical potential of each species in both coexisting phases phases. The predicted phase diagram is shown in Fig. 4.2 on a mass fraction basis. The glycine solubility curve is given by the blue line. There is a liquid-liquid phase coexistence region predicted by the thermodynamic model, which is shaded in red; the lightly shaded region is the binodal, where the solution is metastable, while the darkly shaded region is the spinodal, where the solution is unstable and will spontaneously split into two phases. Note that this entire two-phase region is metastable with respect to glycine crystallisation.

The thermodynamic model (i.e. Eq. (4.1) with parameters given in Table 4.1) predicts a region of liquid-liquid phase separation, which is metastable with respect to the solid-liquid phase coexistence. The spinodal curve associated with this liquid-liquid phase separation is shown in red. For concentrations within the region enclosed by this curve, the solution is unstable and will spontaneously separate into two liquid phases. Consequently, the model predicts that liquid-liquid phase separation (LLPS) can occur under certain conditions during the anti-solvent crystallisation processes, which may be experimentally observed as “oiling out” of the solution under certain conditions.

In Figure 4.2 the binodal region is depicted in light red. Compositions within this region are considered meta-stable and liquid demixing can take place. This means that as the composition enters the binodal region during the mixing process there is the potential for LLPS to occur. The possibility for phase separation would then be dependent on the relative size of the mixing and phase separation kinetics. Demixing kinetics for our system have not been reported in literature, and kinetics for anti-solvent systems could not be found. This makes a comparison between these competing process difficult. However, it is important to note that whilst we do not model phase separation in our model,any compositions that lie within the binodal region have the potential for LLPS to occur, complicating the control of nucleation.

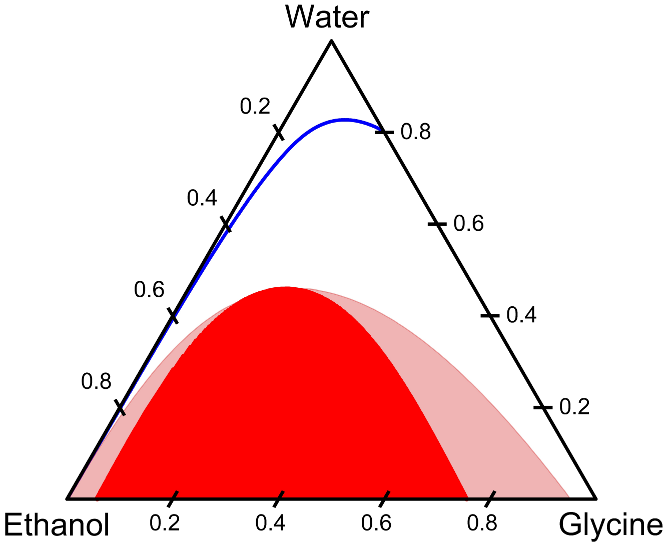

Figure 4.2: Ternary phase diagram for the glycine/water/ethanol system on a mass basis. The calculated glycine solubility curve is shown with the blue line. The binodal region is shown as the light red shaded area, and the spinodal region is shown as the dark red shaded area on the ternary phase diagram.

## 4.3 Multi-component diffusion in water/ethanol/glycine mixtures

The dynamics of the species in solution are governed by the conservation equation, which relates the local accumulation of a species to its local flux.

$$\frac{\partial c_i}{\partial t} + \nabla \cdot \mathbf{N}_i = 0. \tag{4.5}$$

where $c_i$ is the local molar concentration of species $i$. The total species flux $\mathbf{N}_i$ can be separated into a convective and a diffusion contribution as

$$\mathbf{N}_i = c_i\mathbf{v} + \mathbf{J}_i \tag{4.6}$$

where $\mathbf{v}$ is a fluid velocity, and $\mathbf{J}_i$ is the diffusive flux. The division between the two types of fluxes is somewhat arbitrary and dependent of the choice of the definition of the fluid velocity, such as a centre of mass velocity, molar velocity, or solvent velocity.[20] While the choice of reference frame does not impact the physics of a system, some choices are more convenient than others depending on its particular boundary conditions. In this work, we deal with a sealed liquid systems, where there is little volume change of mixing, so the molar volumes of each component can be assumed to be constant (and equal to its volume in the pure state). In this case, it is natural to use the fluid velocity based on the volume reference frame, which is defined by

$$\mathbf{v} = \sum_j V_j \mathbf{N}_j \tag{4.7}$$

where $V_j$ is the volume occupied by species $j$. The corresponding diffusive fluxes satisfy the relation:

$$\sum_i V_i \mathbf{J}_i = 0. \tag{4.8}$$

Note that the component volumes $V_i$ used in the definition of the volume reference frame are distinct from the volumes $v_i$ used in the free energy model developed in chapter 3.2. In this work, $V_i$ is taken to be the molar volume of the pure component $i$ and represents the space occupied by a molecule; their values are summarised in Table 4.2. The volumes $v_i$ are considered to be fitting parameters in the free energy model that are chosen to reproduce the thermodynamic properties of the system, such as the species activity coefficients.

In this work, the Maxwell-Stefan approach is used to describe the molecular diffusion in the system.[10, 21] Within this theoretical framework for an isothermal system, the diffusive fluxes of each molecular species $\mathbf{J}_i$ are driven by the gradients in the chemical potentials $\mu_i$ through the relations:

$$c_i \nabla \beta \mu_i = \sum_j \frac{1}{Đ_{ij}} (x_j \mathbf{J}_i - x_i \mathbf{J}_j) \tag{4.9}$$

where $c_i$ is the concentration of species $i$, and $Đ_{ij}$ is the mutual diffusion coefficient between species $i$ and $j$. For a ternary mixture, this can be formally inverted to give explicit formulas for the diffusive fluxes in the volume reference frame:[20]

$$\begin{pmatrix} \mathbf{J}_1 \\ \mathbf{J}_2 \end{pmatrix} = -\frac{1}{\Delta} \begin{pmatrix} \frac{(1-\phi_1) V_1}{Đ_{02}} + \frac{\phi_1 V_0}{Đ_{12}} & -\phi_1 \left( \frac{V_2}{Đ_{01}} - \frac{V_0}{Đ_{12}} \right) \\ -\phi_2 \left( \frac{V_1}{Đ_{02}} - \frac{V_0}{Đ_{12}} \right) & \frac{(1-\phi_2) V_2}{Đ_{01}} + \frac{\phi_2 V_0}{Đ_{12}} \end{pmatrix} \begin{pmatrix} c_1 \boldsymbol{\nabla \beta \mu_1} \\ c_2 \boldsymbol{\nabla \beta \mu_2} \end{pmatrix} \tag{4.10}$$

where $\phi_i$ is the volume fraction of species $i$ defined in terms of the volumes $V_i$.

More commonly, Fick's law is used to relate the diffusive flux to the composition gradient within a mixture. For a ternary component system, diffusive flux $\mathbf{J}_i$ of component $i$ is given by :[22]

$$\begin{pmatrix} \mathbf{J}_1 \\ \mathbf{J}_2 \end{pmatrix} = - \begin{pmatrix} D_{11} & D_{12} \\ D_{21} & D_{22} \end{pmatrix} \begin{pmatrix} \boldsymbol{\nabla \phi_1} \\ \boldsymbol{\nabla \phi_2} \end{pmatrix} \tag{4.11}$$

where $D_{ij}$ is the Fickian diffusion coefficient of component $i$ in $j$.

The Maxwell-Stefan expression for the diffusive fluxes, given in Eq. (4.10), can be recast in the Fickian form for diffusion, providing a relation between the Fickian diffusion coefficients are related to the Maxwell-Stefan diffusion coefficients:

$$\begin{pmatrix} \mathbf{J}_1 \\ \mathbf{J}_2 \end{pmatrix} = -\frac{1}{\Delta} \begin{pmatrix} \frac{(1-\phi_1) V_1}{Đ_{02}} + \frac{\phi_1 V_0}{Đ_{12}} & -\phi_1 \left( \frac{V_2}{Đ_{01}} - \frac{V_0}{Đ_{12}} \right) \\ -\phi_2 \left( \frac{V_1}{Đ_{02}} - \frac{V_0}{Đ_{12}} \right) & \frac{(1-\phi_2) V_2}{Đ_{01}} + \frac{\phi_2 V_0}{Đ_{12}} \end{pmatrix} \begin{pmatrix} \Gamma_{11} & \Gamma_{12} \\ \Gamma_{21} & \Gamma_{22} \end{pmatrix} \begin{pmatrix} \boldsymbol{\nabla \phi_1} \\ \boldsymbol{\nabla \phi_2} \end{pmatrix} \tag{4.12}$$

where $\Gamma_{ij}$ is known as the matrix of thermodynamic factors and is defined as

$$\Gamma_{ij} = c_i \frac{\partial \beta \mu_i}{\partial \phi_j}. \tag{4.13}$$

The matrix $\Gamma$ describes the impact of non-ideal solution behaviour on diffusion and can be calculated from a thermodynamic model, such as the one developed in chapter 3.2. For an ideal solution, $\Gamma$ reduces to the identity matrix. In this work, the ideal solution is defined for the case $\chi_{01} = \chi_{02} = \chi_{12} = 0$ and $v_0 = v_1 = v_2$. This ignores the contribution due to the size differences of the molecules and their mutual interactions, and results in an activity coefficient of 1.

The Maxwell-Stefan approach has several advantages to the more commonly used Fickian description of diffusion. Unlike the Fickian diffusion coefficients, the Maxwell-Stefan coefficients $Đ_{ij}$ are symmetric;[10] therefore, for a ternary mixture, only three diffusion coefficients are required. In addition, the Fickian diffusion coefficients ($D_{ij}$ in Eq. (4.11)) are dependent on the reference frame; their values depend on the particular reference frame that is selected. Furthermore, these values are dependent on concentration, pressure and temperature.[22] For binary mixture, the simplicity of Fickian diffusion has seen it become the standard for interpreting experimental measurements, and binary diffusion coefficients are typically reported in terms of Fickian diffusivity. For multi-component mixtures, the situation becomes more complicated with the diffusivity being expressed by a non-symmetric $(n-1) \times (n-1)$ matrix for an $n$-component mixture.

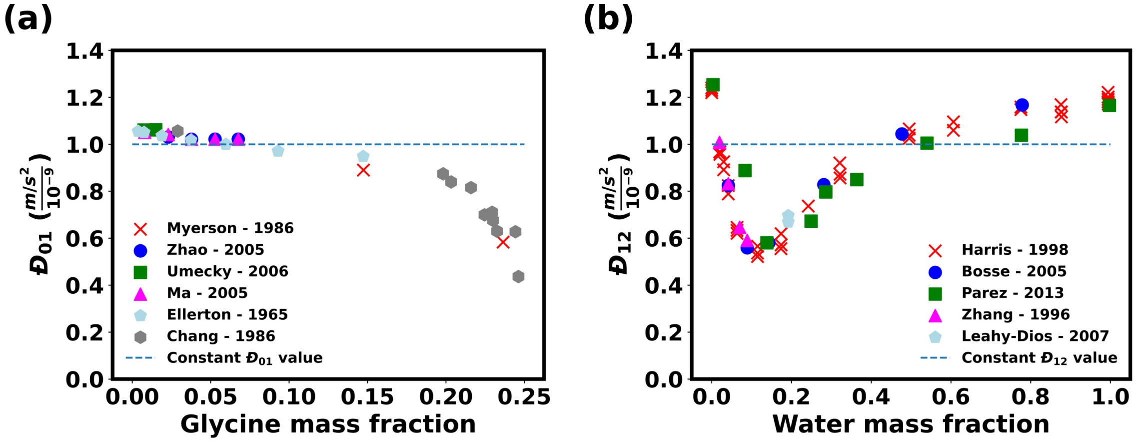

Figure 4.3: Maxwell-Stefan diffusion coefficients for (a) water/glycine $Đ_{01}$ and (b) water/ethanol $Đ_{12}$. The grey dashed line indicates the representative value for the diffusion coefficient used in this work.

Estimates for the Maxwell-Stefan diffusion coefficients were obtained from Fickian diffusion coefficients reported in the literature for binary glycine-water[23–28] and ethanol-water[29–33] mixtures, through the use of Eqs. (4.11), (4.12), and (4.13), combined with the thermodynamic model developed in section. 4.2. The results are shown in Fig. 4.3.

For simplicity in the calculations in this work, the Maxwell-Stefan diffusion coefficients were assumed to be independent of composition, and a nominal value of $10^{-9}\mathrm{m}^2\,\mathrm{s}^{-1}$ was selected for each pair of binary diffusion coefficients. The diffusion coefficient for ethanol/glycine was unknown, and it was chosen to be of a similar magnitude. To explore the range of plausible behaviours, a parametric study was performed for the values of diffusion coefficients used. The value ranges selected were based on the maximum and minimum values experienced over the compositions ranges for water/ethanol and water/glycine. The range of values for the ethanol/glycine were selected to be of similar magnitudes. This analysis was carried out for both ideal and non-ideal diffusion. Table 4.2 summarises the

Table 4.2: Parameters of the diffusion model.

| parameter | value | values investigated |
|---|---|---|
| Glycine relative molar volume: $V_0/V_1$ | 3.58 | — |
| Ethanol relative molar volume: $V_2/V_1$ | 3.23 | — |
| $Đ_{01}$ / $10^{-9}\,\mathrm{m}^2\,\mathrm{s}^{-1}$ | 1 | 0.40, 1.00, and 1.25 |
| $Đ_{02}$ / $10^{-9}\,\mathrm{m}^2\,\mathrm{s}^{-1}$ | 1 | 0.40, 1.00, and 1.25 |
| $Đ_{12}$ / $10^{-9}\,\mathrm{m}^2\,\mathrm{s}^{-1}$ | 1 | 0.40, 1.00, and 1.25 |

values of diffusion coefficients used in the model.

## 4.4 Simulation details

We examined systems confined within a closed, rigid channel of width 1 mm. The size of the channel was chosen for simplicity. The left side is initially filled with an aqueous glycine solution, and the right side is initially filled with the anti-solvent or an anti-solvent/solvent mixture. An example of the initial volume fraction profile is given in appendix A.1. The solution and anti-solvent were allowed to freely diffuse into each other, with no convective mixing taking place. The system was assumed to have one-dimensional symmetry.

The temperature was assumed to be constant at 298 K, and heat of mixing was neglected. The components chosen in this work form a non-ideal mixture; however, to simplify the model, the volume change upon mixing was not considered. Nucleation is not considered in this model, although the calculated supersaturation profiles will provide qualitative insight into the propensity for crystal formation. Diffusive mixing is firstly assumed to be ideal, before accounting for non-idealities via the inclusion of the thermodynamic model.

Diffusive mixing in anti-solvent crystallisation was modelled by using Eq. (4.5). In this work, the system is approximately incompressible, and the convective flux in the volume frame is nearly stationary (i.e. $\mathbf{v} \approx 0$). In this case, it is natural to use the diffusive fluxes in the volume frame. The species conservation equation then becomes:

$$\frac{\partial \phi_i}{\partial t} = -\nabla \cdot (V_i \, \mathbf{J}_i).$$

This formulation ensures that $\sum_i \phi_i(\mathbf{r}, t) = 1$. Neumann boundary conditions were imposed on the channel walls: $\hat{\mathbf{n}} \cdot \nabla \phi_i = 0$ (i.e. no flux at channel walls). The parameters of the diffusion model are summarised in Table 4.2.

These diffusion equations were numerically solved using the finite volume solver FiPy v3.4[34] on a regular one dimensional domain with 1024 mesh points and a time step of 0.1 s. The number of mesh points and size of the time step were varied to ensure that the solution was accurate and independent of their particular choice. See appendix A.3 for details.

To study the effect of key process parameters on supersaturation profiles, the initial volume fraction profile of the channel was varied. The parameters investigated were the initial anti-solvent composition, ratio of anti-solvent to solution within the channel and the initial glycine concentration in the aqueous glycine solution. Table 4.3 summarises the parameters and the ranges of values used. The anti-solvent was a mixture of water and ethanol. Supersaturation profiles were calculated from the volume fraction profiles obtained from the model using the thermodynamic model described in chapter 4.2. In this work, the supersaturation of glycine is defined as the ratio between the its local activity in the solution and its activity in a saturated solution with the same local solvent composition (i.e. $S = x_0 \gamma_0 e^{-\beta(\mu_0^s - \mu_0^\circ)}$). The activity coefficient of glycine in the solvent mixture is calculated via Eq. (4.3).

Diffusion in non-ideal liquid mixtures was simulated and compared both qualitatively and quantitatively to the ideal case. With nucleation most likely to occur within the region of peak supersaturation, the compositional trajectories of the peaks were plotted

Table 4.3: Key process parameters

| **Process Parameter** | **Range** |
|---|---|
| Initial anti-solvent composition | Pure ethanol–50 vol% ethanol |
| Anti-solvent: solution ratio in channel | 9 : 1–3 : 7 |
| Initial glycine volume fraction in solution | 0.08–0.23 |

on a phase diagram for both ideal and non-ideal diffusion. This highlights the qualitative differences in the mixing process, and in particular the differences in local composition of the peak supersaturation. The phase diagram indicates the spinodal region, and based on the trajectory of the peak supersaturation, spinodal decomposition can be predicted to occur. In terms of crystallisation, nucleation could occur in the oiled out phase, thus significantly effecting local composition and therefore nucleation outcomes.

In the diffusion simulations, crystal nucleation was not modelled. One consequence of this is that the effect of glycine solute removal through nucleation is not accounted for. The aim of this study is to qualitatively assess the behaviour of solutes in anti-solvent systems.Although nucleation would act to dampen the predicted supersaturation profiles, particularly at longer times, however the predicted behaviour of glycine within the system would not expected to change.

## 4.5 Results and discussion

### 4.5.1 Ideal parametric study

Here we explore the range of behaviours predicted by the ideal diffusion model across typical anti-solvent crystallisation conditions. Key process parameters were varied, namely anti-solvent composition, ratio of solution to anti-solvent and the initial supersaturation. Figure 4.4 summarises the results of this study. To quantify the comparisons across the parameter values, the maximum supersaturation attained during mixing is plotted along with the fully mixed supersaturation. This gives insight into how nucleation conditions are impacted by

Table 4.4: Key process 'centre point' values. This indicates the values of key process parameters used when not being varied. Anti-solvent is mixture of ethanol and water.

| Parameter | Value |
|---|---|
| Ethanol mass fraction in anti-solvent | 0.80 |
| Solution:Anti-solvent ratio | 1:1 |
| Initial Supersaturation | 0.85 |

the relative parameter, along with the relative size of the 'overshoot' in supersaturation. As one parameter is varied, the others are held constant at 'centre point' values. Table 4.4 summarises this.

Figure 4.4a shows how the peak supersaturation is effected by initial anti-solvent composition. A clear trend is observed, with anti-solvent with higher ethanol content relating to greater supersaturations. The trend in the ratio of peak to final supersaturation is more apparent in figure 4.5b. Larger overshoots are present in the pure anti-solvent, which becomes increasingly lower as the water content increases. From intuition this is expected. In the ideal model, supersaturation reduces to the ratio of mol fraction of glycine and the saturated value, i.e. solubility. Glycine diffuses down its composition gradient and the overshoot in supersaturation will be dictated by the local solubility of the anti-solvent. Solubility is extremely low in the pure anti-solvent and thus large overshoots are predicted. For anti- solvents that have higher water content and therefore solubility, the peak supersaturation decreases with respect to the final value. This again reflects that in the ideal model supersaturation is dependent on local solution solubility.

Figure 4.4c depicts the effect of varying the solution:anti-solvent ratio. The peak supersaturation at early times was found to be independent of this ratio. This agrees with the study by Thorson.[8] In terms of diffusion, this can be explained by considering short time behaviour at the interface. Immediately after the onset of mixing glycine diffuses into the anti-solvent and an overshoot in supersaturation is observed. At distances away from the interface, the glycine does not start to diffuse until there is sufficient driving force present.

As diffusion proceeds at the interface a compositional gradient is generated, as glycine moves into the anti-solvent. The same reasoning can be applied to the diffusion of water and ethanol. At long times, the ratio of solution:anti-solvent impacts the supersaturation profile, which can be seen in the final supersaturation. A straight forward relationship is seen, with more anti-solvent leading to higher final supersaturations. This is simply due to the lower solubility of the solvent mixture. One limitation of this study is the exclusion of nucleation. Nucleation would act to dampen the supersaturation, and if it is sufficiently high at the interface, then long term predicted profiles could fail to represent the physical system.

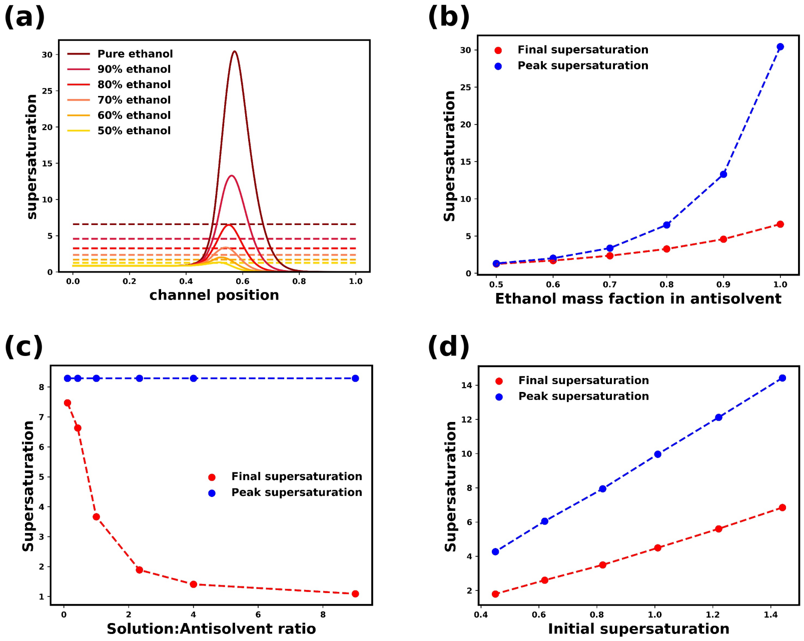

Figure 4.4: Summary of effect of key process parameters. (a) Effect of anti-solvent composition after 1s after mixing. Dotted lines indicate 'final fully mixed' supersaturation. (b) - (d) show the highest supersaturation that is experienced during the mixing process (blue), in comparison to the final value (red). This assumes no crystallisation. Dotted lines are aesthetic only, and do not represent a predictive model. (b): initial anti-solvent composition, (c): Solution to anti-solvent ratio & (d) initial supersaturation. All supersaturations are expressed in the ratio of local activity to saturation activity.

The last parameter investigated was the initial supersaturation, which is equivalent to the initial mass fraction of glycine in the solution. The trends in both peak and final supersaturation are once more what would be expected from intuition. That is, increased glycine in the initial solution results in an increased supersaturation in the fully mixed system. The peak supersaturation follows the same trend. This is caused by the increased driving force for the diffusion of glycine. This means more glycine would be present in the anti-solvent thus, greater degree of supersaturation. The evolution of the spatiotemporal supersaturation profiles are shown in appendix A.4.1

### 4.5.2 Effect of non-ideality on diffusive mixing

In previous work on modelling of diffusive mixing in anti-solvent crystallisation processes, the solutions are usually assumed to be ideal, and the diffusion of a species is taken to be driven by its local concentration gradient. However, anti-solvent crystallisation systems are necessarily highly non-ideal, and the assumption of ideality fails to properly represent the key feature of the system — the tendency of the solute to avoid mixing with the anti-solvent. Chemical potential (or equivalently activity) gradients, rather than the composition gradients, fundamentally drive species diffusion,[10, 21] and so non-ideal mixing is expected to play a significant role in the dynamics of the system.

To examine the influence of non-ideal mixing on diffusion, the time evolution of the concentration profiles are compared in Figs. 4.5(a), (c), (e), and (g). The solid lines correspond to the ideal systems, while the dashed lines correspond to the non-ideal systems. The corresponding supersaturation profiles are shown in Figs. 4.5(b), (d), (f), and (h).

Differences in the diffusion between the ideal and non-ideal mixtures are most apparent in the concentration profile of glycine. In the ideal mixture, the driving force is the composition gradient (which is identical to the activity in this case), and glycine diffuses from a region of relatively high concentration in the solvent to a region of relatively low concentration in the anti-solvent. Due to the low solubility of glycine in the anti-solvent mixture, a large peak in supersaturation is rapidly generated at the interface between the glycine solution and the anti-solvent. At 1 s (see Figs. 4.5(a) and (b)), a large overshoot in supersaturation is observed (i.e. a peak above the value of the supersaturation in the final fully mixed system). As mixing proceeds, the "peak" of supersaturation curve moves towards the anti-solvent side of the channel.

This supersaturation peak slowly flattens and eventually vanishes as water diffuses into the anti-solvent, increasing the local solubility of glycine. On the solution side of the channel, inter-diffusion of the solution and the ethanol leads to a reduction of solubility. As a consequence, the supersaturation of glycine gradually increases to the final, fully mixed value. By 500 s, the supersaturation becomes uniform across the channel as the composition gradients within the system relax.

In the non-ideal mixture, activity gradients drive the diffusion, and glycine will diffuse away from the anti-solvent, which is "uphill" with respect to its composition gradient. As water inter-diffuses with the ethanol, glycine is dragged with the water into the anti-solvent. This generates a peak in the supersaturation profile at the solution/anti-solvent interface, however, due to the tendency of the glycine to diffuse away from ethanol, this does not lead to an overshoot, where supersaturation exceeds the final, fully mixed value (denoted by the dashed dark purple line) due to the relatively low concentration of glycine in the anti-solvent. This is one obvious difference from the ideal system.

Another difference between the two, is that the concentration profiles evolve more slowly in the non-ideal system. Considering Figs. 4.5(g) and (h), while the supersaturation profile within the channel are nearly uniform, approaching that of the fully mixed system, composition gradients are still present. This emphasises that the physical system acts primarily to smooth out any gradients in chemical potential as opposed to compositional gradients. As the activity gradient flattens, the driving force for diffusion decreases, which

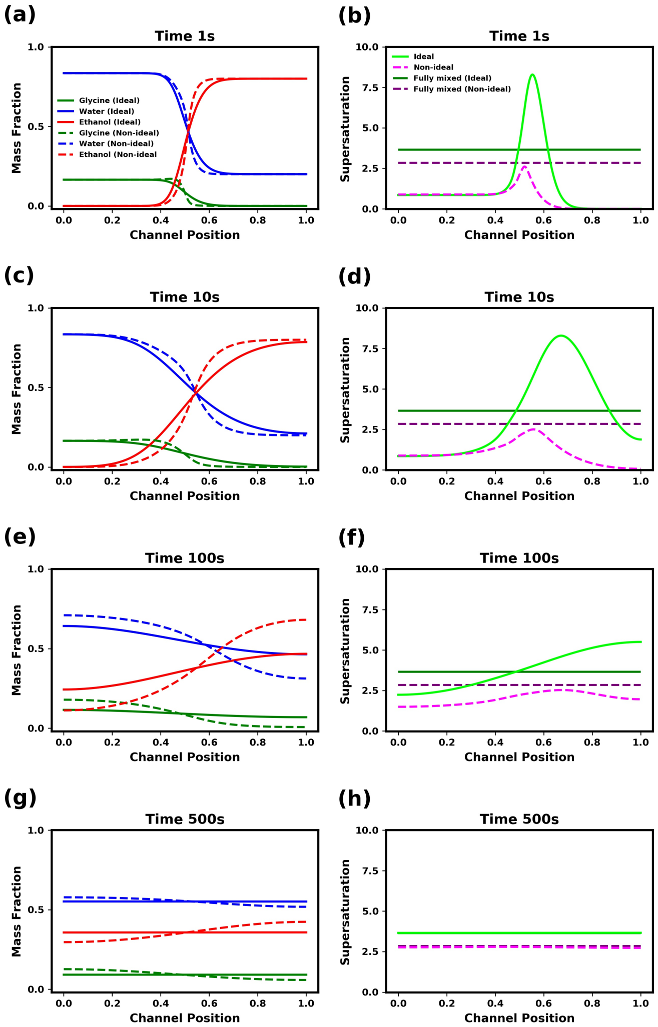

Figure 4.5: Comparison of diffusion mixing in ideal and non-ideal solutions. The volume fraction and supersaturation profiles are shown at various times for ideal (solid lines) and non-ideal (dashed lines) diffusion. The initial supersaturation in the solvent is 0.85 for the ideal model and 0.89 for the non-ideal model. The initial anti-solvent composition was 80 wt% ethanol and 20 wt% water. The mutual diffusion coefficients were all $10^{-9}\,\mathrm{m}^2\,\mathrm{s}^{-1}$. The channel position is in reference to simulated channel described in the section 4.4. The initial solution/anti-solvent interface is at 0.5 mm.

is reflected in the comparatively longer times for the composition profiles to become uniform in the non-ideal systems, as compared to faster relaxation in ideal systems.

### 4.5.3 Non-ideal parametric study

The effects of key processes parameters were previously discussed for mixing in ideal solutions. Through the inclusion of a free energy model we find that the ideal model fails to represent the physical process, and diffusion behaviour is qualitatively very different when non-ideal solutions are considered. Figure 4.6 summarises the effect of key process parameters, this time, with the effect of solution non-ideality included.

Anti-solvent composition (4.6b) indicates that the peak supersaturation experienced is only slightly greater than the final value. Additionally the large 'overshoot' is no longer present initially after mixing as is with the ideal case. This suggests that large overshoots in supersaturation as expected through intuition do not occur. However, figure 4.6a highlights that the initial peak supersaturation increases with increasing ethanol wt % in the anti-solvent, similarly to the ideal case, as does the value of the maximum supersaturation attained during mixing.

The ratio of solution:anti-solvent again produced results similar to the ideal model. For ratios of 1:1 or greater the peak supersaturation is approximately constant. For these ratios the initial peak is located at the interface between the solution and anti-solvent, and was found to be independent of solution: anti-solvent ratio. At small time scales, mixing is only experienced at the interface and this is expected. Low amounts of relative anti-solvent lead to the final supersaturation being relatively low, and the initial peak is found to be the highest in magnitude. For ratios less than one, the peak value is realised due to high anti-solvent composition in the final mixture. For the ratio of 1:3 (solution:anti-solvent) the largest overshoot occurs as the anti-solvent mixes into the solution. Glycine moves relatively slow in comparison to the water/ethanol intermixing and hence supersaturation

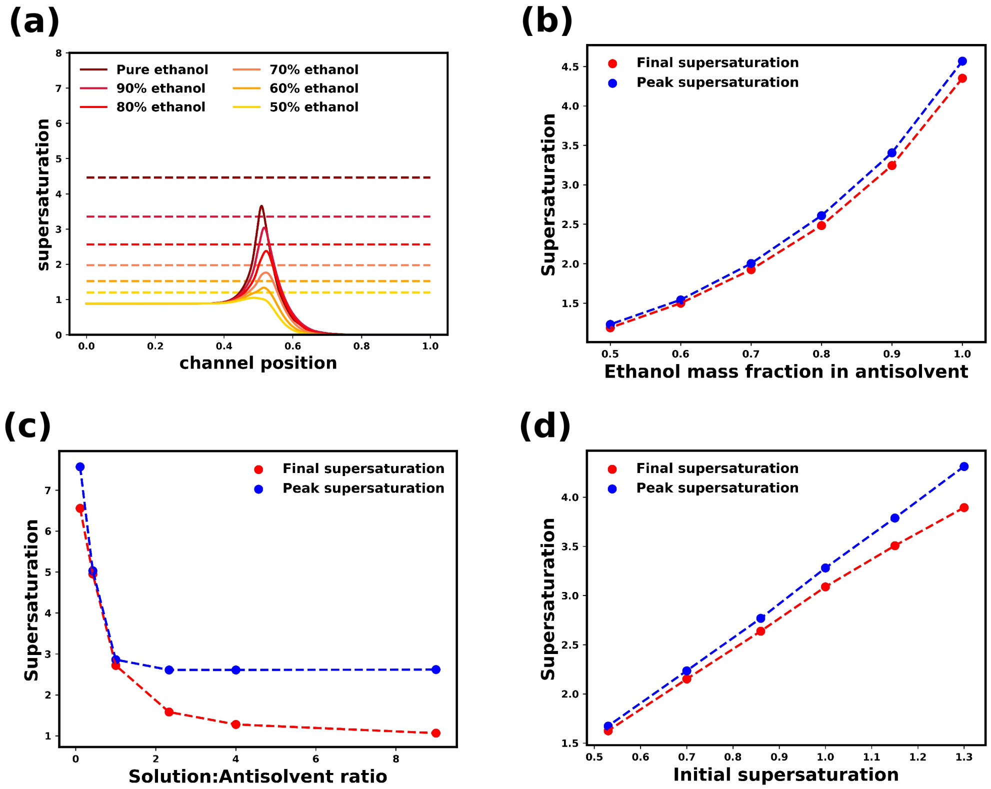

Figure 4.6: Summary of effect of key process parameters. (a) Effect of anti-solvent composition after 1s after mixing. Dotted lines indicate 'final fully mixed' supersaturation. (b) - (d) show the highest supersaturation that is experienced during the mixing process (blue), in comparison to the final value (red). This assumes no crystallisation. Dotted lines are aesthetic only, and do not represent a predictive model. (b): initial anti-solvent composition, (c): Solution to anti-solvent ratio & (d) initial supersaturation

is generated as ethanol lowers local solubility. As the model does not include glycine nucleation, the predicted supersaturations may differ at longer time scales.

Quantitative trends were unchanged from the ideal and non-ideal models with higher initial supersaturation (initial glycine mass fraction) producing higher supersaturations. The key difference between models is once more the magnitude of the overshoots. In the non-ideal model these are small, and increase with higher supersaturations as more glycine is present. Spatiotemporal profiles are shown in appendix A.4.2

When comparing trends of key process parameters for ideal and non-ideal models we find they are similar. However a key difference is observed when considering the magnitudes of peak supersaturations. The non-ideal model predicts more modest peaks. The composition of the peak varies between models and therefore significantly different nucleation conditions are modelled. The ideal model therefore fails to predict real-life physical process, even if the effects of key process parameters make sense intuitively.

### 4.5.4 Influence of relative diffusivities

The above analysis assumed that all the mutual diffusion coefficients were equal to $10^{-9}\,\mathrm{m^2\,s^{-1}}$. In this section, we examine the influence of the relative values of the three mutual diffusion coefficients on the behaviour of the system. Each mutual diffusion coefficient was chosen to have one of two values: a low value of $0.4 \times 10^{-9}\,\mathrm{m^2\,s^{-1}}$ and a high value of $1.25 \times 10^{-9}\,\mathrm{m^2\,s^{-1}}$. These values encompass the range of diffusion coefficients experimentally observed across relevant composition ranges (see Fig. 4.3). Simulations were performed for each of the eight combinations of values of the mutual diffusion coefficients, which are depicted graphically in Fig. 4.7(a). The sensitivity of predicted supersaturation profiles with reference to the relative values of mutual diffusion coefficients can be determined by considering the temporal variation of the supersaturation profiles for each combination of values used.

We begin our investigation with ideal solutions. Figure 4.7 shows supersaturation profiles at various times for ideal solutions with different sets of mutual diffusion coefficients. For all systems, the supersaturation profiles form a peak at the solvent/anti-solvent interface, and this peak broadens and moves deeper into the anti-solvent, eventually meeting the right wall of the channel and then gradually becoming uniform.

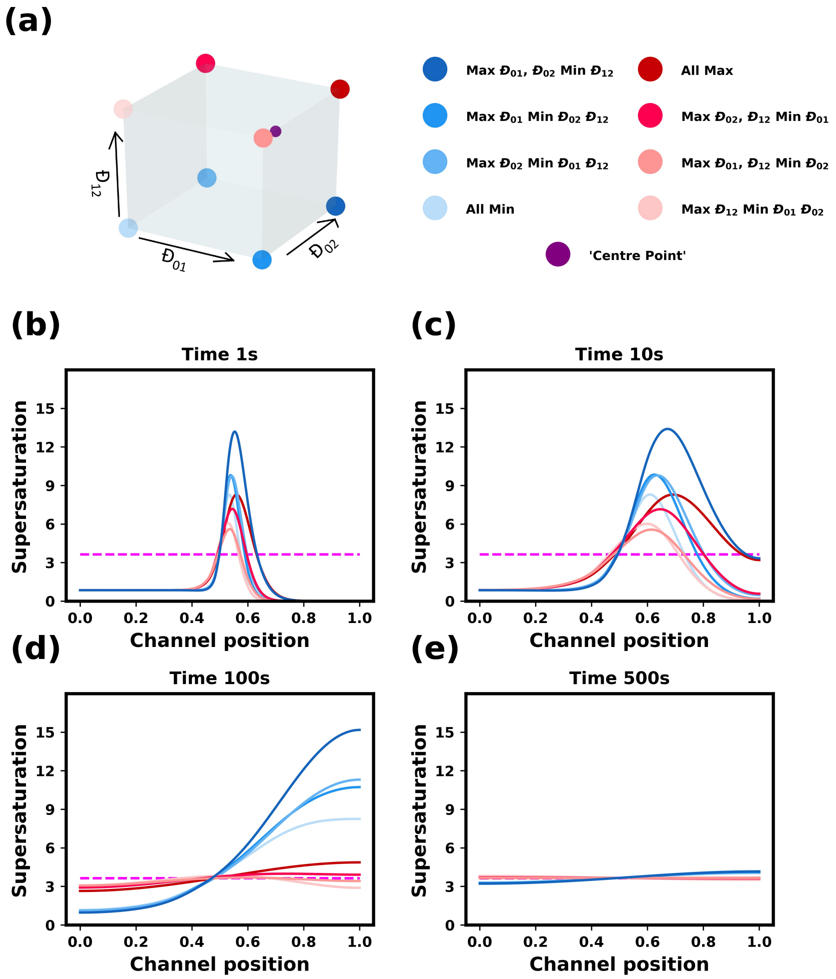

Figure 4.7: Influence of the mutual diffusion coefficients on the dynamics of ideal solutions. (a) The corners of the cube represent the 8 sets of diffusion coefficients used in this work. The purple point indicates the representative "Reference point" values used in Fig. 4.5. (b)–(e): Evolution of supersaturation profiles at 1, 10, 100, and 300 s. The initial supersaturation in the solvent is 0.85. The initial anti-solvent composition was 80 wt% ethanol and 20 wt% water.The horizontal dashed magenta line shows the value of the fully mixed supersaturation. The channel position is in reference to simulated channel described in section 4.4. The initial solution/anti-solvent interface is at 0.5 mm.

However, the precise evolution of the supersaturation profiles is sensitive to the relative values of binary coefficients used in the model. Moments after the onset of mixing, the systems appear to divide into two groups: those with higher supersaturation overshoots where the water/ethanol mutual diffusion coefficient $Đ_{12}$ is small, and those with lower supersaturation overshoots where the water/ethanol diffusivity is large.

The systems with the higher supersaturations, which have a blue shade in Fig. 4.7, correspond to conditions in which the minimum value of the glycine/ethanol diffusion coefficients is used (i.e. $0.4 \times 10^{-9} \mathrm{m}^2\,\mathrm{s}^{-1}$). This is expected, as glycine will diffuse into the anti-solvent mixture at a faster rate than water. This causes the anti-solvent to have a relatively higher fraction of ethanol, which implies that the solubility of glycine in the anti-solvent will remain low, resulting in a large overshoot in the local supersaturation. For these systems, the height of the peak continues to grow as it moves into the anti-solvent mixture. They also relax more slowly to the uniform profile, but this can be directly attributed to the lower value of $Đ_{12}$.

The systems with the lower supersaturations, which have a red shade in Fig. 4.7, have a higher value of the water/ethanol mutual diffusion coefficient. Because the water and ethanol mix more quickly, glycine solubility in the anti-solvent mixture increases more rapidly, which prevent the local supersaturation from becoming very large. For these systems, the height of the supersaturation peak decreases as it moves into anti-solvent mixture. We also note that in situations where glycine diffuses more slowly, the glycine concentration in the anti-solvent mixture increases gradually, allowing water to more time to mix with ethanol, which leads to lower supersaturations.

In summary, the qualitative behaviour of the spatiotemporal evolution of the supersaturations profiles in ideal solutions appears to be controlled mainly by the magnitude of the water/ethanol mutual diffusion coefficient, with slower water/ethanol mixing leading to a larger overshoot of the local supersaturation.

Following the same approach as for ideal solutions, a parametric study of the diffusion coefficients in non-ideal mixtures was carried out, and the evolution of the supersaturation profiles are shown in Fig. 4.8. As before, a local peak in the supersaturation appears at the solvent/anti-solvent interface. A key difference from the ideal case, as observed in the previous section, is that the local supersaturation does not, in general, overshoot the final, fully mixed value. Only for one set of diffusion coefficients does it slightly exceed the fully mixed value, however, then it quickly falls below the final supersaturation.

Similarly to the ideal case, two groups can be seen to form, driven by the difference in the water/ethanol mutual diffusion coefficient Because the dynamics is slower in the non-ideal systems, it takes somewhat longer times before these groups become qualitatively distinct. For the group of systems with the lowest value of $Đ_{12}$ (coloured with a blue shade in Fig. 4.8), the supersaturation in the solvent side increases much more slowly, as compared to that for the group of systems with the highest value of $Đ_{12}$ (coloured with a red shade in Fig. 4.8). In addition, the peak of the local supersaturation in the blue group gradually increases in height and slowly moves into the anti-solvent mixture, eventually reaching the right side of the channel at a value slightly over the fully mixed supersaturation. For the red group, the peak remains relatively stationary, even slightly moving into the solvent, as the supersaturation curve flattens.

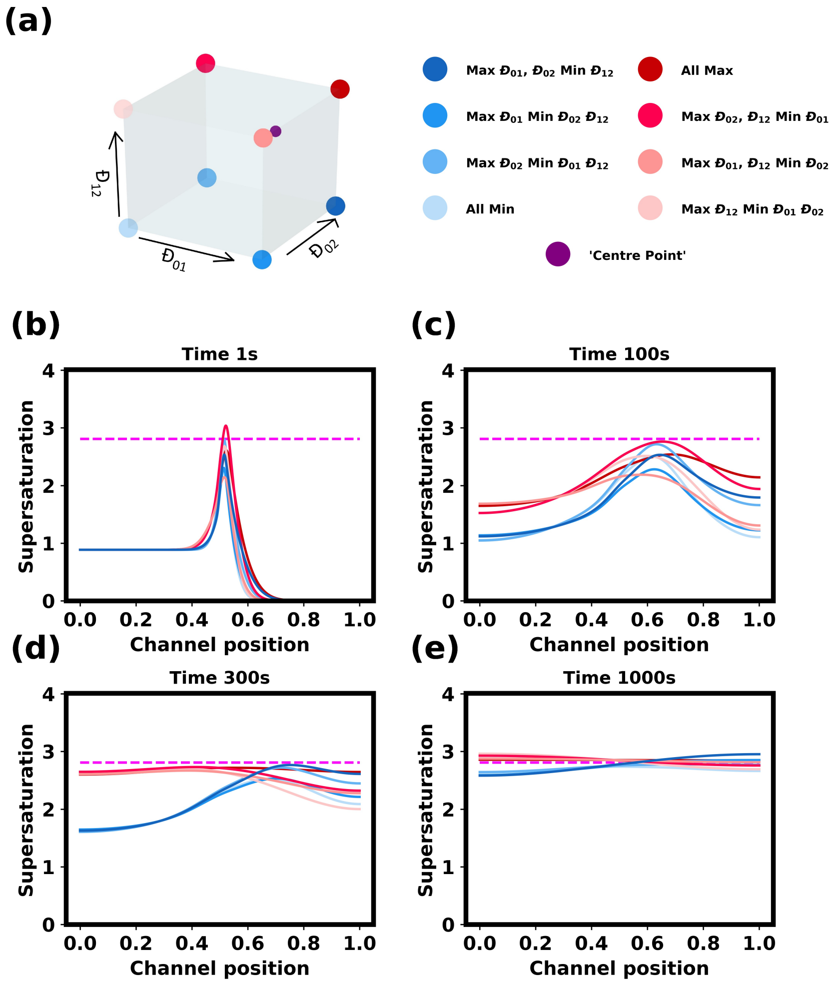

Figure 4.8: Influence of the mutual diffusion coefficients on the dynamics of non-ideal solutions. (a) Cube plot and with corners showing the 8 sets of diffusion coefficients used. The purple dot indicates the "reference point" values used in Figs. 4.5. (b) – (e): Evolution of supersaturation profiles at times 1, 100, 300, and 1000 s. The initial supersaturation in the solvent is 0.89. The initial anti-solvent composition was 80 wt% ethanol and 20 wt% water.The horizontal dashed magenta line shows the value of the fully mixed supersaturation. The channel position is in reference to simulated channel described in section 4.4. The initial solution/anti-solvent interface is at 0.5 mm.

To gain more insight into the cause of this behaviour, the mass fraction profiles of each species across the channel at 300 s are shown in Fig. 4.9. Figure 4.9(a) shows that the glycine in the red group (fast solvent/anti-solvent diffusivity) has diffused relatively quickly into the anti-solvent, in comparison to the blue group (slow solvent/anti-solvent diffusivity). This indicates the intermixing of water/ethanol helps to facilitate the diffusion of glycine. The movement of glycine into the anti-solvent incurs a large chemical potential penalty (i.e. the local chemical potential would increase as glycine diffuses into ethanol), and, consequently, glycine retreats further to the solvent solution to avoid contact with ethanol. As the water content in the anti-solvent increases, this penalty is significantly reduced, and glycine starts to diffuse into the anti-solvent mixture. Another consideration is the effect of diffusing water “dragging” the glycine along with it as it intermixes with ethanol. Both of these phenomena lead to faster diffusion of glycine into the anti-solvent in the red group in relation to the blue group.

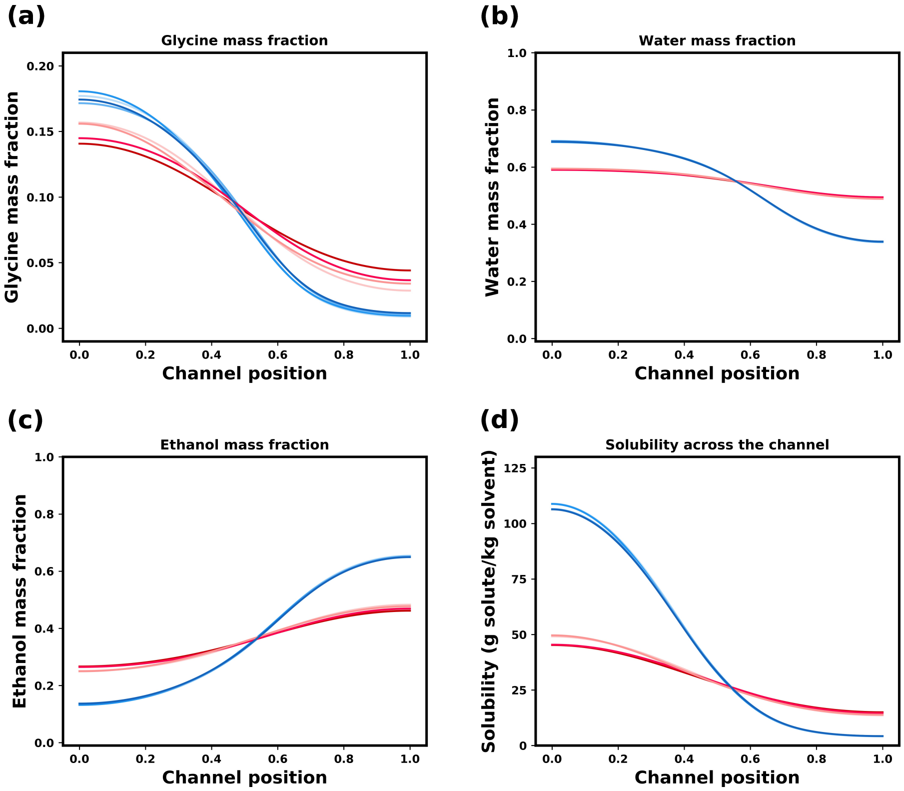

Figure 4.9: Mass fraction profiles in a non-ideal system at 300 s for (a) glycine, (b) water, and (c) ethanol. (d) Solubility of glycine in the solvent mixture. The initial supersaturation in the solvent is 0.85. The initial anti-solvent composition was 80% ethanol and 20 wt% water. The colour scheme is the same as in Fig. 4.8(a), in which blue is slow anti-solvent/solution diffusivity, and red is fast.

From the relative amounts of glycine in the anti-solvent, one would expect the red group to have a supersaturation peak at the channel wall on the anti-solvent side of the system. However, if we consider the local composition, we can see why this happens for the blue group. The intermixing of the solvents results in low local solubility in the anti-solvent side of channel, and hence with even low amounts of glycine, supersaturation is generated.

Additionally, in the blue group, the slow diffusion of ethanol into the solution only causes a modest rise in supersaturation. The location of the supersaturation peak is therefore dependent on both glycine composition and local solvent composition/solubility.

This suggests that regardless of precise values of mutual diffusion coefficients, it is very unlikely that significant supersaturation overshoots would occur due to diffusive mixing in anti-solvent crystallisation processes. Therefore, predictions based on ideal solution models and Fickian diffusion and corresponding intuitions are physically incorrect.

### 4.5.5 Peak supersaturation trajectories in ternary phase diagram

Crystal nucleation is most likely to occur in the system at the peak of the local supersaturation. In Fig. 4.10, the compositional trajectory of the supersaturation peak with respect to time is plotted on a mass based ternary phase diagram. Each point represents a time step of 1 s. The trajectories for the eight sets of diffusivity values are divided into three groups:

A: **All diffusion coefficients are the same:** This includes the two extreme combinations in which all three coefficients were set to the maximum and minimum values. The case where the diffusion coefficients are equal to $10^{-9}\mathrm{m}^2\,\mathrm{s}^{-1}$ (the "reference point") was added to this group. This relates to Fig. 4.10(a).

B: **One diffusion coefficient is significantly lower:** This is the case in which the diffusivity of one of the components was much lower than the other two in the mixture. These are the combinations in which one of the diffusion coefficients is chosen at the minimum of the range, while the other two are selected to be the maximum. This relates to Fig. 4.10(b)

C: **One diffusion coefficient is significantly higher:** Similar to B, but with one maximum and two minimum values being selected. This relates to Fig. 4.10(c)

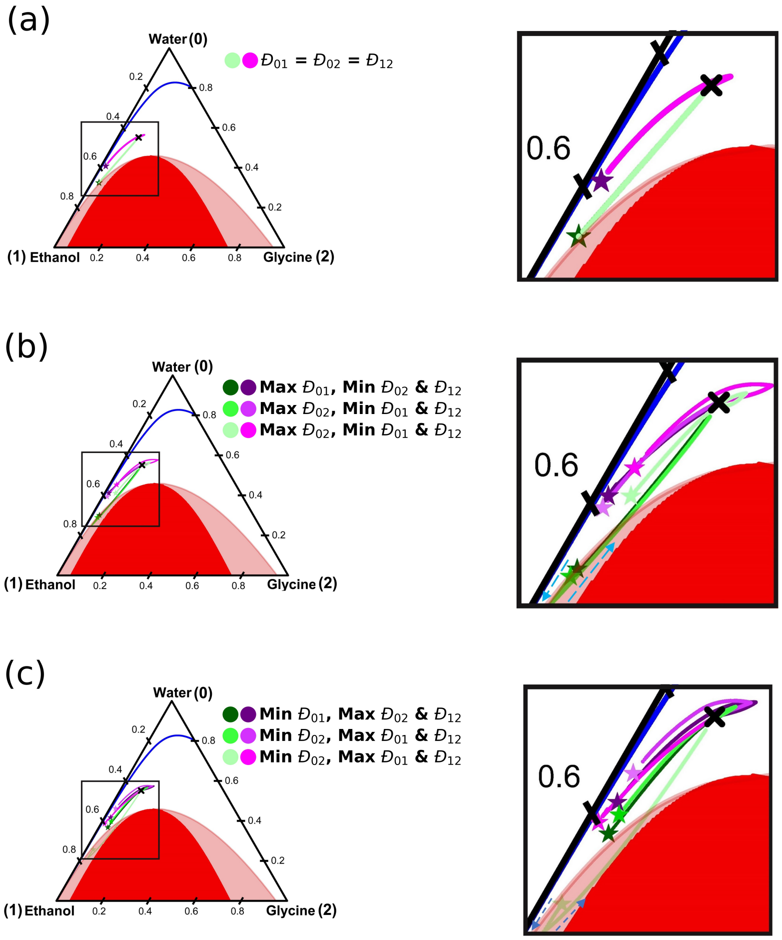

Figure 4.10: Ternary phase diagram showing the trajectories of the peak supersaturation compositions within the channel with respect to time. The stars indicate initial location of the supersaturation peak, while the black cross is the final fully mixed composition of the system. The blue dashed lines in (b) and (c) highlight that the trajectories initially move towards the ethanol corner, before changing direction. The sets of diffusion coefficients used relate to those in Figs. 4.7 and 4.8. The initial supersaturation in the solvent is 0.89. The initial anti-solvent composition was 80 wt% ethanol and 20 wt% water. Green and purple trajectories refer to ideal and non-ideal models respectively.

In group A (shown in Fig. 4.10a), no significant differences can be seen in the predicted trajectories among the three cases for both ideal (shown in green) and non-ideal (shown in purple) model. This is expected, as all three diffusion coefficients have the same value, so the relative fluxes and the compositional trajectories are identical, while only time scale affected (the differences in diffusive mixing times between ideal and non-ideal solutions are highlighted in Fig. 4.5). The ideal solution model predicts much higher concentrations of glycine and a higher concentration of ethanol at the peak supersaturation mixture. This again highlights that supersaturation in the ideal solution is driven by the glycine moving into the anti-solvent in which solubility is very low. The trajectory for the non-ideal system initially bypasses the final solvent mixture composition due to the movement of glycine into the aqueous solution, as it avoids the anti-solvent. The peak supersaturation is generated by an increased glycine concentration in the solution. As the water and ethanol intermix, glycine diffuses into the anti-solvent mixture, and the final composition is reached.

Figures 4.10(b) and (c) show a range of trajectories for both the ideal and non-ideal model. First, the non-ideal model will be considered. Here, two behaviours are observed: one similar to the group A and the opposite case, in which no initial bypass of the final mixture composition is present. It is found that all combinations with the maximum diffusion coefficient value for water/ethanol lead to this bypass in the trajectory. This corresponds to the red group in Fig. 4.9. The opposite is found to be true for combinations with the minimum coefficient for water/ethanol (blue group). This is explained by considering the cause of the peak supersaturation. For the red group, the fast mixing of the solvent and anti-solvent lowers the local solubility of the solution, where the glycine concentration remains high. In addition, until the anti-solvent and solvent are sufficiently mixed, only small amounts of glycine move into the anti-solvent. For the blue group, water and ethanol mix slowly with respect glycine. Supersaturation is generated by glycine being present in regions with low local solubility. As water and ethanol mix, the final composition is approached. It is clear from the trajectories and the supersaturation profiles Fig. 4.9 that the solvent/anti-solvent diffusion coefficient plays a significant role in determining mixing profiles.

In the ideal trajectories, two behaviours were observed to occur. This was also based on the mutual diffusion coefficient of water/ethanol. For combinations in which water/ethanol diffusion was minimised, the trajectory initially moves towards the ethanol corner of phase diagram. This reflects that the supersaturation is caused by glycine moving into the low solubility anti-solvent. As glycine reaches the channel wall, its mass fraction increases. Concomitantly, the mass fraction of water at the peak supersaturation increases as water/ethanol mix. From here, the trajectory moves to the final composition. In the opposite case, the trajectory bypasses the final composition in a similar manner to the non-ideal case. The water/ethanol mix relatively quickly, and the peak supersaturation in the first instance is caused by anti-solvent lowering the local solubility of the glycine solution. This is seen in the trajectory, where the starting composition is more concentrated in water. As glycine catches up with ethanol, the trajectory approaches the final composition.

In summary, the modelling approach developed here describes compositional and supersaturation profiles due to diffusive mixing in non-ideal ternary mixtures during the induction time preceding any crystal formation. Although crystallisation itself is not considered here, this model providing valuable insights into diffusive mixing in anti-solvent crystallisation within realistic non-ideal solutions,

### 4.5.6 Liquid-liquid phase separation

While the peak supersaturation trajectories in the ideal systems (shown in green in Fig. 4.10) stay relatively close to the line connecting the initial compositions of the solution and anti-solvent mixtures, in non-ideal systems (shown in purple in Fig. 4.10) they can explore a much wider range of ternary mixture compositions. Interestingly for non-ideal systems, the composition profile can potentially enter the liquid-liquid phase coexistence region (which is denoted by the red shaded body in the ternary phase diagram in Fig. 4.2), even though the final mixture composition may be well outside the the liquid-liquid phase coexistence region. In particular, if the composition trajectory enters the spinodal region, it would directly lead to localised instantaneous liquid-liquid phase ]separation (LLPS) in the mixture.

Typically each of the coexisting liquid phases would have very different solute concentrations,[35] and because crystallisation is strongly dependent on the local mixture compositions, LLPS can significantly influence crystal nucleation and growth and affect the outcomes of anti-solvent crystallisation. The presence of LLPS, even if only local or intermittent, can have a profound effect on the particular crystal polymorph that forms and the resulting particulate attributes in an anti-solvent crystallisation process. For example, in the continuous anti-solvent crystallisation of lovastatin, McGinty et al.[36] found that the size and aspect ratio of the needle-like crystals formed could be controlled by altering the process conditions. Spinodal decomposition was suggested as a possible explanation for the change in aspect ratio, where under certain conditions nucleation and growth occurs inside "oiled out" droplets at local compositions different from the overall mixture composition,[37, 38] resulting in different crystal morphologies.

Consequently, it is crucial to understand when LLPS could potentially occur. When the overall liquid mixture composition is in the spinodal (or binodal) region during anti-solvent crystallisation, LLPS can occur and is usually observed as macroscopic "oiling out"; however, LLPS can also be present, but less apparent, when spinodal decomposition or rapid nucleation of the second liquid phase turns the system turbid, which is then followed by subsequent solid phase nucleation, before macroscopic oiling out can be observed. In order to investigate the scenario where the overall mixture composition is outside of the liquid-liquid phase coexistence region, but there is localised LLPS during diffusive mixing, a set of conditions was chosen where the peak supersaturation reaches the spinodal curve. The evolution of the composition profile across the channel with time is shown in Fig. 4.11.

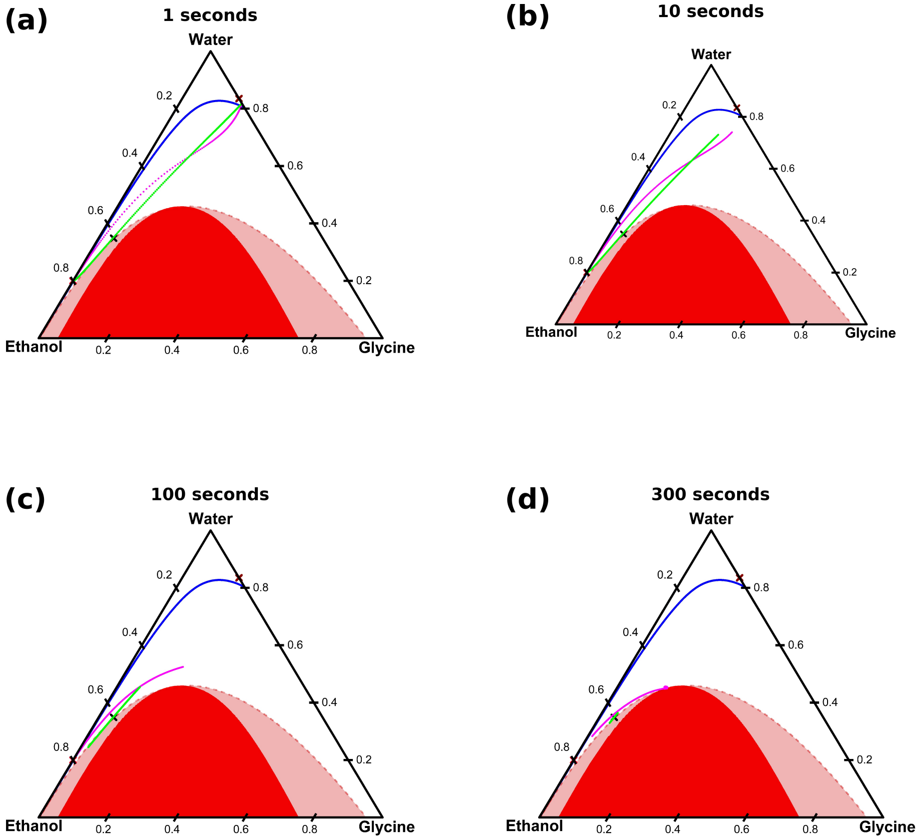

Figure 4.11: Example of predicted liquid-liquid phase separation during diffusive mixing. Note the run is stopped when the spinodal curve is encountered, as the model is not capable of simulating the actual demixing process. The anti-solvent consisted of 80 wt% ethanol and 20 wt% water, the initial supersaturation was 0.89, and the channel was filled with an initial volume ratio of 7:3 anti-solvent to solution. Each of the mutual diffusion coefficients is assumed to have a constant value of $10^{-9}\,\mathrm{m^2\,s^{-1}}$. The composition profile across the channel for the non-ideal case is shown in purple; the composition profile for the ideal case is depicted in green, and is shown for comparative purposes only, as phase separation does not occur in ideal solutions. The red crosses denote the starting compositions of the anti-solvent and solutions.

In this scenario, localised spinodal decomposition is predicted in the course of diffusing mixing. It is worth noting that this is not due to supersaturation with respect to the solid phase, as this remains similar to the final fully mixed value, although local solvent mixture compositions can be rather different from the final fully mixed conditions.

Instead, this is due to the solution becoming locally thermodynamically unstable with respect to the liquid-liquid separation, so that localised LLPS would be instant due to spinodal decomposition.

The non-ideal diffusive mixing model developed here can provide quantitative information on conditions that are likely to cause the local LLPS in non-ideal ternary solutions. This will provide novel insights into LLPS phenomena and their role in anti-solvent crystallisation processes.

## 4.6 Conclusions

Anti-solvent crystallisation systems are highly non-ideal, and assuming ideality in modelling of diffusive mixing fails to provide a qualitatively accurate representation of local composition and supersaturation profiles. Diffusive mixing in ideal solutions relies in the Fickian framework where the driving force for diffusion is based on concentration gradients rather than chemical potential gradients, leading to unphysical predictions of local, large overshoots in the local supersaturation profile with respect to that in the final, fully mixed system. A detailed study on the diffusive mixing of an anti-solvent system consisting of glycine/water/ethanol was performed for both ideal and non-ideal solutions. Qualitative differences were observed between models with the large supersaturation overshoots predicted in the ideal model, but not by the non-ideal model. This is caused by solute initially diffusing away from the anti-solvent, against the concentration gradient, as dictated by the chemical potential gradient, based on non-ideal solution thermodynamics. It was also found that for certain conditions, localised liquid-liquid spinodal demixing can be expected during diffusive mixing, even when the final mixture composition would suggest otherwise. While diffusive mixing is unlikely to lead to significant sensitivity of nucleation to mixing conditions, intermittent spinodal demixing driven by diffusive mixing may provide a novel explanation for differences of nucleation behaviours among various anti-solvents.

## 4.7 References

[1] Y Dong et al. Pharmaceutical nanotechnology a continuous and highly effective static mixing process for antisolvent precipitation of nanoparticles of poorly water-soluble drugs. *Int. J. Pharm.*, 386:256–261, 2010.

[2] L A.I. Ramakers et al. Investigation of Metastable Zones and Induction Times in Glycine Crystallization across Three Different Antisolvents. *Cryst. Growth Des.*, 20(8):4935–4944, 2020.

[3] S J Park and S D Yeo. Liquid antisolvent recrystallization of phenylbutazone and the effect of process parameters. *Sep. Sci. Technol.*, 46(8):1273–1279, 2011.

[4] H M. Omar and S Rohani. Crystal Population Balance Formulation and Solution Methods: A Review. *Cryst. Growth Des.*, 17(7):4028–4041, 2017.

[5] J. W. (John William) Mullin. *Crystallization.* Oxford, UK, 2001.

[6] H H Shi et al. Progress of crystallization in microfluidic devices. *Lab Chip*, 17(13):2167–2185, 2017.

[7] D. C. Leslie. Review of developments in turbulence theory. *Rep. Progr. Phys*, 36(11):1365–1424, 1973.

[8] Michael R. Thorson et al. Microfluidic approach to polymorph screening through antisolvent crystallization. *CrystEngComm*, 14(7):2404, 2012.

[9] Venkateswarlu Bhamidi et al. Antisolvent Crystallization and Polymorph Screening of Glycine in Microfluidic Channels Using Hydrodynamic Focusing. *Cryst Growth Des.*, 15(7):3299–3306, 2015.

[10] R Krishna. Uphill diffusion in multicomponent mixtures. *Chem. Soc. Rev,*, 44(10):2812–2836, 2015.

[11] Emmerich Wilhelm. Mitigating complexity: Cohesion parameters and related topics. i: The hildebrand solubility parameter. *J. Solution Chem.*, 47(10):1626–1709, 2018.

[12] T Lindvig, M L Michelsen, and G M Kontogeorgis. A Flory-Huggins model based on the Hansen solubility parameters. *Fluid Phase Equilib.*, 203:247–260, 2002.

[13] H Kuramochi et al. Measurements of vapor pressures of aqueous amino acid solutions and determination of activity coefficients of amino acids. *J. Chem. Eng. Data*, 42(3):470–474, 1997.

[14] H Dobson and J Eglinton. The partial pressures of aqueous ethyl alcohol. *J. Chem. Soc. Faraday Trans*, 127(0):2866–2873, jan 1925.

[15] D. J. Hall, C. J. Mash, and R. C. Pemberton. Vapor liquid equilibriums for the systems water-methanol, water-ethanol, methanol-ethanol, and water-methanol-ethanol at 298.15 K determined by a rapid transpiration method. *NTRL*, (NPL-Chem-95):36 pp., 1979.

[16] Zheng Cao et al. Solubility of glycine in binary system of ethanol+water solvent mixtures: Experimental data and thermodynamic modeling. *Fluid Phase Equilib.*, 360:156–160, 2013.

[17] E J. Cohn, T L. McMeekin, J T. Edsall, and J H. Weare. Studies in the physical chemistry of amino acids, peptides and related substances. II. The solubility of $\alpha$-amino acids in water and in alcohol-water mixtures. *J. Am. Chem. Soc*, 56(11):2270–2282, 1934.

[18] J W Kim and K K Koo. Crystallization of glycine by drowning-out combined with fines dissolution and cooling process with in situ control using focused beam reflectance measurement and attenuated total reflection-Fourier transform infrared spectroscopy.

*Cryst. Growth Des.*, 12(10):4927–4934, 2012.

[19] L. A. Ferreira, E. A. Macedo, and S. P. Pinho. Solubility of amino acids and diglycine in aqueous-alkanol solutions. *Chem. Eng. Sci.*, 59(15):3117–3124, 2004.

[20] D G. Miller, V Vitagliano, and R Sartorio. Some comments on multicomponent diffusion: Negative main term diffusion coefficients, second law constraints, solvent choices, and reference frame transformations. *J. Org. Chem.*, 90(8):1509–1519, 1986.

[21] R Krishna and J A Wesselingh. Review Article number 50:The Maxwell-Stefan approach to mass transfer. *Chem. Eng. Sci.*, 52(6):861–911, 1997.

[22] O Medvedev. *Diffusion coefficients in multi-component mixtures.* PhD thesis, Technical University of Denmark, 2005.

[23] A. S. Myerson and Y. C. Chang. Diffusional separation in ternary systems. *AIChE J.*, 32(10):1747–1749, Oct 1986.

[24] C W Zhao, J D Li, P S Ma, and S Q Xia. Measurement of liquid diffusion coefficients of aqueous solutions of glycine, L-alanine, L-valine and L-isoleucine by holographic interferometry. *Chin. J. Chem. Eng.*, 13:285–290, 2005.

[25] T Umecky, T Kuga, and T Funazukuri. Infinite dilution binary diffusion coefficients of several $\alpha$-amino acids in water over a temperature range from (293.2 to 333.2) K with the Taylor dispersion technique. *J. Chem. Eng. Data*, 51(5):1705–1710, 2006.

[26] Y Ma, C Zhu, P Ma, and K. T. Yu. Studies on the diffusion coefficients of amino acids in aqueous solutions. *J. Chem. Eng. Data*, 50(4):1192–1196, 2005.

[27] H. David Ellerton, Gundega Reinfelds, Dennis E. Mulcahy, and Peter J. Dunlop. The mutual frictional coefficients of several amino acids in aqueous solution at 25°c. *J. Phys. Chem.*, 68(2):403–408, 1964.

[28] Y. C. Chang and A. S. Myerson. Cluster diffusion in metastable solutions. *AIChE J.*, 33(4):697–699, 1987.

[29] K R. Harris, P J. Newitt, and Z. J. Derlacki. Alcohol tracer diffusion, density, nmr and ftir studies of aqueous ethanol and 2,2,2-trifluoroethanol solutions at 25°c. *J. Chem. Soc. Faraday Trans.*, 94(14):1963–1970, 1998.

[30] D Bosse and H-J Bart. Measurement of diffusion coefficients in thermodynamically nonideal systems. *J. Chem. Eng. Data*, 50(5):1525–1528, Aug 2005.

[31] S Pařez, G Guevara-Carrion, H Hasse, and J Vrabec. Mutual diffusion in the ternary mixture of water + methanol + ethanol and its binary subsystems. *Phys. Chem. Chem. Phys.*, 15(11):3985–4001, 2013.

[32] K. J. Zhang, M. E. Briggs, R. W. Gammon, and J. V. Sengers. Optical measurement of the soret coefficient and the diffusion coefficient of liquid mixtures. *J. Chem. Phys.*, 104(17):6881–6892, May 1996.

[33] A Leahy-Dios and A Firoozabadi. Molecular and thermal diffusion coefficients of alkane-alkane and alkane-aromatic binary mixtures: Effect of shape and size of molecules. *J. Phys. Chem*, 111(1):191–198, 2007.

[34] J E Guyer, D Wheeler, and J A Warren. FiPy: Partial differential equations with python. *Comput. Sci. Eng.*, 11(3):6–15, 2009.

[35] L. Derdour. A method to crystallize substances that oil out. *Chem. Eng. Res. Des.*, 88(9):1174–1181, sep 2010.

[36] J McGinty et al. Effect of process conditions on particle size and shape in continuous antisolvent crystallisation of lovastatin. *Crystals*, 10(10):1–17, 2020.

[37] Z Meng, Y Huang, S Cheng, and J Wang. Investigation of oiling-out phenomenon of small

organic molecules in crystallization processes: A review. *ChemistrySelect*, 5(26):7855–7866, jul 2020.

[38] E Deneau and G Se. An in-line study of oiling out and crystallization. *Org Process Res Dev*, 9(6):943–950, 2005.

## Chapter 5

# Diffusive mixing in Anti-solvent Crystallisation: Effect of Anti-solvent and Macroscopic Mixing

## 5.1 Introduction

Anti-solvent crystallisation is widely used in pharmaceutical and chemical industry for separation and purification processes where a solute is crystallised from solution through the addition of a miscible anti-solvent. Ideally, solution becomes homogeneous instantly upon anti-solvent addition so that the local composition is same everywhere in the crystallisation vessel. In reality, though, there are composition inhomogeneities at multiple length scales and corresponding characteristic time scales of mixing. Crystallisation kinetics, and especially crystal nucleation, are driven by the local solution composition and the corresponding supersaturation and are thus strongly dependent on the composition heterogeneity, especially at the anti-solvent addition point and local mixing conditions.

Relevant mixing processes strongly depend on the vessel, its mode of operation and manner of anti solvent addition. Mixing processes under turbulent conditions can be subdivided into three cascading mechanisms; macro-mixing, meso-mixing and micro-mixing.[1] Commonly these spatial scales are divided using the definition by Baldyga and Bourne.[2] Macro-mixing is defined to be above the Kolmogorov length scale ($L_k$), whilst micro-mixing takes place at the Bachelor scale ($L_b$) or lower. Meso-mixing is considered as the intermediate between these two scales. These scales can be further described by the dominant mixing mechanisms at the respective scale: inertial–convective, viscous–convective and viscous–diffusive for macro, meso and micro-mixing scales respectively.[3]

Macro-mixing occurs at the vessel scale and describes the dispersion of fluids by mean velocity fields. Mean velocity fields act to spatially rearrange fluid elements, with the species concentrations remaining unchanged within each element. Thus macro-mixing controls the fluid element concentrations in which micro-mixing takes place, and moves these elements to different regions within the vessel, in which turbulent properties vary.[1] Here, reduction of fluid elements to the Kolmogorov scale are caused by turbulent dispersion. These are then further reduced to the Bachelor scale by viscous deformation, which accelerates the diffusion process. Micro-mixing therefore plays a vital role in determining the effectiveness of crystallisation processes, even in under turbulent mixing conditions, as only the final diffusive step leads to molecular level mixing of the anti-solvent

To describe micro-mixing, many models have been developed, with varying degrees of complexity. The simplest model proposed by Mao and Toor[4] represents the system as a series of stagnant slabs, with inter-diffusion taking place between them. The thickness of the slabs was determined experimentally using fast neutralisation reactions under a specific set of hydrodynamic conditions. In this approach, acceleration of diffusion due to fluid shear and viscous deformation is not taken into account, and this model is widely considered to too simplistic[3, 5]

Interactions between fluid element deformation and molecular diffusion was accounted for in subsequent models. The lamellar model proposed by Ottino et al[6] describes turbulent motion results in the creation of lamellar structures from the fluids being mixed. Mixing effects at the meso and macro-scale act to stretch the lamella and reducing their thickness, thus facilitating molecular diffusion. Baldyga and Bourne reported the engulfment-deformation-diffusion model (EDD).[7] In the EDD model a lamellar structure is formed through the engulfment of vortexes. Layers of fluid within the lamella are stretched and deformed by fluid motion. Finally diffusion takes place between each fluid layer. This process is repeated as new vortices are formed until a homogeneous solution is reached. This model was simplified in further work by Baldyga and Bourne[8] to the engulfment model (E) for cases in which the Schmidt number is significantly lower than 4000 and more than two engulfments are required for the system to be fully mixed. This simplification assumes that engulfments are the rate determining step in the mixing processes and that deformation and diffusion steps are slow in comparison.

Li et al[9] suggested that fluid layers are subjected to convective forces that cause stretching of the layer, and again reducing the thickness. This model is referred to as the slab shrinkage (SS) model. The SS model argues that lamellar structures are not formed, but rather fluid layers are dispersed through the system in forms of slabs or slices. Viscous stresses act to deform and stretch the slabs, accelerating the diffusive mixing process. Li et al observed this experimentally using high speed micro-photography. A tracer was injected into the vessel, and was seen to disperse through the system as slabs.

In our previously developed model[10] of diffusive mixing we simulated multi-component diffusion between fluid layers for an anti-solvent system, namely aqueous glycine and ethanol. Diffusion was modelled for both the cases of ideal solutions and non-ideal solutions. It was found that when using physically correct driving forces for non-ideal solutions (activity gradients as opposed to concentration gradients), the large overshoot in supersaturation intuitively expected with anti-solvent crystallisation was absent. Furthermore localised liquid-liquid phase separation was predicted to occur under certain conditions potentially complicating crystallisation processes. In this model fluid layers were not influenced by macro or meso-mixing processes and only diffusion was modelled. In the absence of convection, acceleration of diffusion through layer stretching or deformation was therefore neglected. Qualitatively however, the model can be related to the inter-diffusion between the fluid layers formed in the micro-mixing models. Although the micro-mixing times may be inaccurate as layer deformation is not considered, system behaviour during the diffusive mass transfer process is still approximately represented by the model. The model therefore provides qualitative insight into mixing at small length scales, such as the Bachelor scale, even under turbulent conditions Additionally, the main focus of this work was the effect of solution non-ideality on diffusive mixing, which is largely independent of deformation effects. i.e. diffusion of glycine towards the anti-solvent was severely hindered due to activity gradients within the system.

Experimental work in literature is limited with regards to anti-solvent mixing effects on crystallisation processes. Ramakers et al[11] investigated meta-stable zone widths for aqueous glycine solution with three anti-solvents, methanol, ethanol and dimethylformamide. Induction times were then measured for these anti-solvent systems. It was observed that induction time were strongly dependent on mixing mechanism. For batch rapid injection, ethanol had longer induction times than the methanol system, whilst the opposite was found for continuous mixing. This is suggests that the choice anti-solvent plays a role in the mixing process, and therefore the resulting crystallisation process. In this work we will simulate the diffusive mixing of aqueous glycine solution with two different anti-solvents - methanol and ethanol. In order to investigate the influence of anti-solvent on diffusive mass transfer and crystallisation outcomes. Previously, diffusion was simulated for two layers of fluid - one solution and the other anti-solvent. In mixing processes, under turbulent conditions, multiple fluid layers will be present, with species exchange occurring simultaneously with adjacent layers. This is represented through the use of periodic boundary conditions, which will be compared to the results using fixed boundary conditions (i.e. to represent diffusion between only two fluid layers) ,allowing for differences in behaviours to be highlighted.

The rest of the chapter will be split into the following sections: 2. A summary of the free energy model used to predict solution activity in the anti-solvent systems. 3. Details on the multi-component diffusion model. 4. Comparison of diffusive mixing for the methanol and ethanol anti-solvent systems. 5. Implementation of periodic boundary conditions and the effect on mixing trajectories. 6. The results of this work will be summarised.

## 5.2 Methods

### 5.2.1 Thermodynamic model for anti-solvent systems

This section briefly summarises the free energy model used in this work. For a more detailed description, the readers are referred to the chapter 3 section 3.3.

The extended Scatchard-Hildebrand activity coefficient model was used to model the non-ideality of ternary component anti-solvent systems. The expression for the Gibbs free energy is given by equation 5.1.[12] The second term in equation 5.1 accounts for the effect of size asymmetry on the entropy of mixing in the standard regular solution model.

$$\beta G = \sum_i x_i \left(\beta \mu_i^\circ + \ln \varphi_i\right) + \frac{1}{2} \frac{v}{v_{\text{ref}}} \sum_{ij} \varphi_i \varphi_j \chi_{ij} \tag{5.1}$$

where $\mu_i^\circ$ is the chemical potential of pure component $i$ in the liquid state at the system temperature, $\beta = 1/(RT)$, $R$ is the gas constant, $T$ is the absolute temperature, $v_{\text{ref}}$ is the reference volume (taken as the solvent volume), $v = \sum_{i=1}^{N} x_i v_i$ is the molar volume of the solution, $x_i$ and $v_i$ are the mole fractions and effective component molar volume, respectively, $\varphi_i = x_i v_i / v$ is the volume fraction of species $i$, and $\chi_{ij}$ is a binary interaction parameter between species $i$ and $j$. The binary interaction parameter are symmetric and describe the non-ideality of the binary mixture. A higher $\chi_{ij}$ value represents a greater incompatibility between the species, and the propensity to demix.

At saturation concentration for a given solvent composition, the chemical potential of glycine in solution and pure solid glycine is equal. This is expressed through equation 5.2.[10]

$$x_0 \gamma_0 = e^{\beta(\mu_0^s - \mu_0^\circ)} \tag{5.2}$$

Note that the right-hand side is independent on solvent composition, and is referred to as the solubility constant in this work ($\alpha_{ijk}$). The activity of glycine is expressed through the left-hand side. This allows us to define supersaturation as a ratio as: $S = \frac{x_0 \gamma_0}{e^{\beta(\mu_0^s - \mu_0^\circ)}}$. When S is greater than 1, the solution is saturated and glycine will have the tendency to crystallise from solution. S = 1 is saturated and less than 1 is under saturated.

## 5.3 Diffusion in anti-solvent systems

This section will provide a brief overview of the diffusive model used in this chapter. A more detailed description can be found in chapter 3.4. Accumulation of a species $'i'$ is related its local flux by the conservation equation. As only diffusion is considered, this is expressed through equation 5.3:

$$\frac{\partial c_i}{\partial t} + \nabla \cdot \mathbf{J}_i = 0. \tag{5.3}$$

The diffusive fluxes $(j)$ are calculated using the Maxwell-Stefan formulation which are recast into the ternary component Fickian diffusive equation.[13] Our work deals with a sealed liquid system, in which the volume change upon mixing is little. We therefore work in the volume reference frame for fluid velocity.[14] The fluxes $(j)$ for each species is then calculated through equation 5.4:

$$\begin{pmatrix} \mathbf{J}_1 \\ \mathbf{J}_2 \end{pmatrix} = -\frac{1}{\Delta} \begin{pmatrix} \dfrac{(1-\phi_1)\,V_1}{Đ_{02}} + \dfrac{\phi_1 V_0}{Đ_{12}} & -\phi_1 \left( \dfrac{V_2}{Đ_{01}} - \dfrac{V_0}{Đ_{12}} \right) \\ -\phi_2 \left( \dfrac{V_1}{Đ_{02}} - \dfrac{V_0}{Đ_{12}} \right) & \dfrac{(1-\phi_2)\,V_2}{Đ_{01}} + \dfrac{\phi_2 V_0}{Đ_{12}} \end{pmatrix} \begin{pmatrix} \Gamma_{11} & \Gamma_{12} \\ \Gamma_{21} & \Gamma_{22} \end{pmatrix} \begin{pmatrix} \nabla\phi_1 \\ \nabla\phi_2 \end{pmatrix} \tag{5.4}$$

where $\Gamma_{ij}$ is known as the matrix of thermodynamic factors and is defined through:

$$\Gamma_{ij} = c_i \frac{\partial \beta \mu_i}{\partial \phi_j}. \tag{5.5}$$

and;

$\Delta$ is given by:

$$\Delta = \frac{x_0}{Đ_{01}Đ_{02}} + \frac{x_1}{Đ_{01}Đ_{12}} + \frac{x_2}{Đ_{02}Đ_{12}} \tag{5.6}$$

In equation 5.4 $Đ_{ij}$ is the Maxwell-Stefan diffusion coefficients, $x_i$ is the mol fraction of species $'i'$, $\phi_i$ is the volume fraction of species $'i'$, $V_i$ is the pure component volume and $c_i$ is species concentration. $\Gamma$ refers to the thermodynamic factor which describes solution non-ideality and requires an free energy model, such as that discussed in the previous section. The volumes used in the diffusion model are taken as the pure component molar volume, and represent the space occupied by a molecule. Note that these values are in reference to the solvent molecule (water). These are distinct from the volumes used in the free energy model, which are taken as fitted parameters. A summary of parameters used in the diffusion model is given in table 5.1

### 5.3.1 Diffusion coefficients

The form of the diffusive flux equations require the value of the Maxwell-Stefan diffusion coefficient for each binary pair. These were calculated from their Fickian counterparts taken from literature. Due to the complexity in determining how the binary coefficient varied with composition in a ternary component mixture, these values were taken as constants. To do this, a weighted average was determined across the composition range for each binary

Table 5.1: Parameters of the diffusion model.

| parameter | value |
|---|---|
| Glycine relative molar volume: $V_0/V_1$ | 3.58 |
| Ethanol relative molar volume: $V_2/V_1$ | 3.23 |
| Methanol relative molar volume: $V_2/V_1$ | 2.23 |
| $Đ_{01}$ / $10^{-9}\,\mathrm{m^2\,s^{-1}}$ | 1 |
| $Đ_{02}$ / $10^{-9}\,\mathrm{m^2\,s^{-1}}$ | 1 |
| $Đ_{03}$ / $10^{-9}\,\mathrm{m^2\,s^{-1}}$ | 1 |
| $Đ_{12}$ / $10^{-9}\,\mathrm{m^2\,s^{-1}}$ | 1 |
| $Đ_{13}$ / $10^{-9}\,\mathrm{m^2\,s^{-1}}$ | 1.5 |

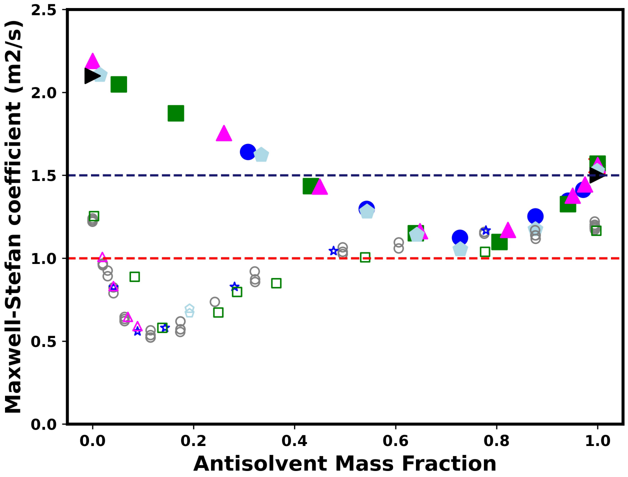

Figure 5.1: Comparison of binary Maxwell-Stefan diffusion coefficients for the water/methanol and water/ethanol solvent/anti-solvent pairs.[15–23] Blue line represents 'average' value of methanol/water diffusion coefficient over composition range. Equivalent value for water/ethanol given in red. Here, the 'average' refers to the average diffusion coefficient value experienced over the composition range.

pair. This is shown in figure 5.1 for water/methanol[15–20] and water/ethanol.[19–23] Diffusion coefficients for glycine in anti-solvent mixtures have not been reported in literature, and as such have been assumed to take the value of $10^{-9}$ m$^2$ s$^{-1}$. Values are shown on table 5.1

### 5.3.2 Simulation details

To represent inter-diffusion between fluid layers at the micro-scale we consider two systems. Firstly, we examine the case for two fluid layers adjacent to each other, One aqueous glycine solution the other anti-solvent. This is simulated as a closed, rigid channel in which the left side is initially filled with the glycine solution and the right hand with anti-solvent/solvent mixture. The solution and anti-solvent were allowed to freely diffuse into each other. Convective mixing was negated. Neumann boundary conditions are imposed on the channel walls, i.e. no flux at channel walls. A width of 1mm was chosen for simplicity.

Table 5.2: Simulation parameters

| **Simulation Parameter** | **Range** |
|---|---|
| Initial anti-solvent composition | Pure anti-solvent–50 vol% anti-solvent |
| Anti-solvent: solution ratio in channel | 9 : 1–3 : 7 |
| Initial glycine volume fraction in solution | 0.08–0.23 |

The second system considered is multiple layers of fluid in contact with each other. This is to represent the case for which fluid layers are dispersed through a system. Periodic boundary conditions are used to simulate this scenario. Again, only diffusion was modelled and convection was assumed to not take place.

For both cases the system was assumed to be one dimensional. The temperature was taken to be constant at 298K, with heat of mixing effects not considered. Although the components form a non-ideal mixture, excess volume was ignored to simplify the model. Lastly, nucleation is not modelled, and therefore supersaturation is not depleted during the mixing process. With this in consideration, the calculated supersaturation profiles will still give a qualitative assessment of nucleation conditions and allow a comparison between different anti-solvents systems.

The finite volume solver FiPy (v3.4)[24] v3.4 was used to solve the diffusion equations. This was done for a regular one dimensional domain containing 1024 solution points, with a time step of 0.01s. These values were varied to ensure that the solution was independent of the specific choices.

The anti-solvents of interest used in this work were methanol and ethanol. To get a full comparison between the two behaviours, the simulations were computed for a range of initial conditions. The parameters changed were; initial anti-solvent composition, initial ratio of solution to anti-solvent within the channel, glycine volume fraction in solution and width of each fluid layer. Table 5.2 summarises the range of parameters used.

## 5.4 Results and discussion

### 5.4.1 Thermodynamics of glycine/water/anti-solvent systems

To model non-ideality within the system the interaction parameters between each binary pair had to be determined. Previously, glycine/water ($\chi_{01}$), glycine/ethanol ($\chi_{02}$) and water/ethanol ($\chi_{12}$) were calculated from thermodynamic data. As such, only the interaction parameters between glycine/methanol ($\chi_{03}$) and water/methanol ($\chi_{13}$) were determined in this article. The volumes used in the activity model are taken as adjustable parameters, and are considered to be distinct to the volumes used in the diffusion model. These are fitted alongside the interaction parameters, and are in reference to the solvent (water) molar volume. Table 5.3 summarises the parameters used in the activity coefficient model. We indicate which parameters were fitted in this work, and those taken from chapter 4. For the remainder of this article, the following species indices apply: glycine (0), water (1), ethanol (2) and methanol (3).

$\chi_{13}$ was calculated by fitting the binary activity model to VLE data acquired from literature[25–29] No binary data was reported in literature for glycine/methanol, therefore

Table 5.3: Values of the parameters used in the thermodynamic model. The nomenclature refers to notation used to represent each parameter. Calculated column indicates if the parameter was calculated in this chapter, or chapter 5.

| Parameter | Nomenclature | Value | Calculated |
|---|---|---|---|
| glycine/water binary interaction parameter | $\chi_{01}$ | 0.59 | Chapter 4 |
| glycine/ethanol binary interaction parameter | $\chi_{02}$ | 2.075 | Chapter 4 |
| glycine/methanol binary interaction parameter | $\chi_{03}$ | 2.065 | Chapter 5 |
| water/ethanol binary interaction parameter | $\chi_{12}$ | 1.07 | Chapter 4 |
| water/methanol binary interaction parameter | $\chi_{13}$ | 0.475 | Chapter 5 |
| glycine relative volume | $v_0/v_1$ | 3.58 | Chapter 4 |
| ethanol relative volume | $v_2/v_1$ | 1.50 | Chapter 5 |
| methanol relative volume | $v_3/v_1$ | 1.07 | Chapter 4 |
| Methanol solubility constant | $\alpha_{013}$ | $-2.55$ | Chapter 5 |
| Ethanol solubility constant | $\alpha_{012}$ | $-2.075$ | Chapter 4 |

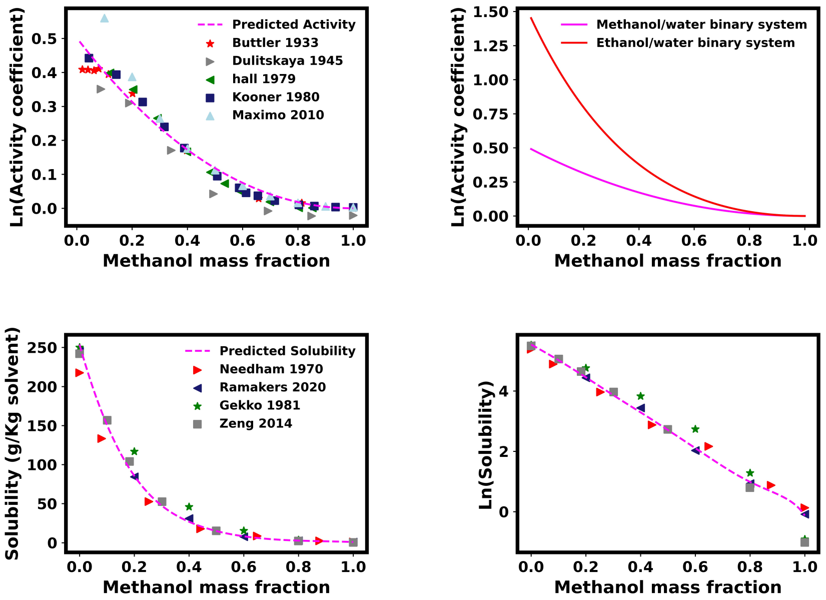

Figure 5.2: (a) Comparison of the predicted vapour pressure with measurements from the literature for water/methanol binary system[25–29] (b) Comparison of activity of methanol/ethanol in water. (c) Solubility of glycine in water/methanol mixtures as predicted by the thermodynamic model at 298 K.[11, 30–32] (d) Solubility shown on a logarithmic scale

glycine solubility in methanol/water mixtures was used to obtain $\chi_{03}$.[11, 30–32] Predicted activity coefficient and solubility are shown in figures 5.2 (a), (c) and (d). Both cases show a favourable comparison with literature data.

Activity coefficients are compared for the solvent/anti-solvent pairs. Figure 5.2 (b) shows that water/methanol behaves more ideally than water/ethanol mixtures. The binary interaction parameters ($\chi_{12}$&$\chi_{13}$), in which water/methanol is approximately half of water/ethanol. These parameters describe the physical incompatibility of the binary pair and the tendency to demix. Lager values describe a greater propensity to demix. This is reflected by the calculated phase diagrams shown in figure 5.3. The methanol system is

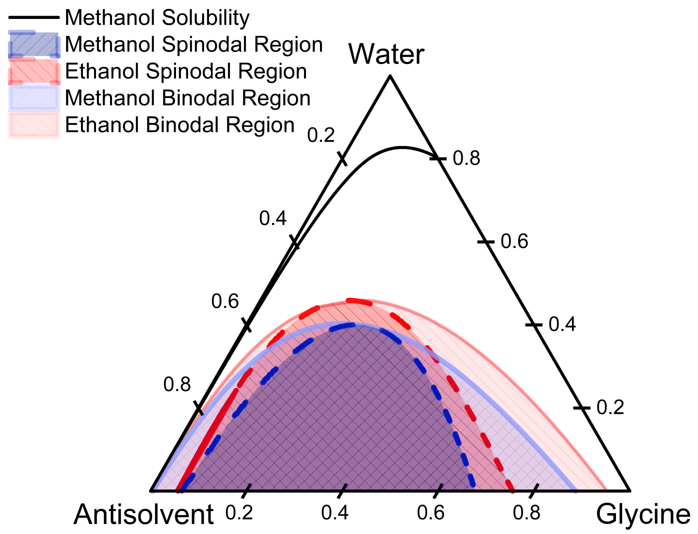

Figure 5.3: Calculated phase diagrams for the glycine/water/methanol and glycine/water/ethanol systems. Binodal regions depicted by light shades of blue and red for the methanol and ethanol systems respectively, whilst spinodal regions are indicated by dark shades. Solubility of glycine in methanol/water mixtures is shown in black. Due to overlapping solubility curves, glycine solubility in ethanol/water systems is not shown, however is available in chapter 4.2.

shown in blue, whilst ethanol is depicted in red. Dark shades and light shades indicate the spinodal and binodal regions respectively. In the spinodal regions, the solution is unstable and spontaneous demixing into two phases will occur. This entire region is meta-stable with respect to glycine crystallisation. It can be seen that these regions are smaller for the methanol system, reducing the probability that compositions that result in liquid-liquid demixing will be present during the diffusive mixing process. The spinodal regions were calculated using the property that the eigenvalues of the thermodynamic factor must be positive (see chapter 3), whilst the binodal regions are determined by equating the chemical potential in both coexisting phases.

### 5.4.2 Solvent effect on diffusive mixing

In anti-solvent crystallisation processes, a key consideration is the choice of anti-solvent to be used, due to the influence on resulting crystal properties. This due to solvent mixture effects on solid forms, and on nucleation and growth kinetics.[11] To investigate this, we compare diffusive mixing profiles for two anti-solvents, namely methanol and ethanol diffusing into aqueous glycine solution. In crystallisation processes the propensity for the solute to crystallise is described through supersaturation, which is related to activity through equation 5.2. Figure 5.4 offers a comparison of supersaturation profiles for both anti-solvent systems. Note that these profiles are related to glycine activity profiles through the solubility constant defined in section 5.2, and thus describe the driving force for diffusion.

Immediately after the onset of mixing (figure 5.4a) a peak in supersaturation is generated at the interface. Contrary to intuition, local activity gradients results in glycine diffusing against its concentration gradient and away from the interface to avoid the anti-solvent.[10] The peak in supersaturation begins to relax as intermixing of solvents occur, with the greater diffusivity of methanol leading to a wider peak in comparison to the ethanol system. Multi-component effects of the ternary component diffusion model results in glycine being 'dragged' into the anti-solvent, increasing glycine activity in the anti-solvent region.

With the methanol system in consideration, after (figure 5.4c) the methanol lowers the solubility in the solution region, and the supersaturation and composition gradient now have the same direction. Furthermore the increased water in anti-solvent region reduces the chemical potential penalty invoked by the solute diffusing into the anti-solvent, i.e. it is less thermodynamically unfavourable for glycine to move into the anti-solvent. Consequently glycine begins diffuses down its concentration gradient.

In the ethanol system (magenta), water is slower to move into anti-solvent region, and the peak in supersaturation remains at greater times. At 300s (figure 4d), the solvents continue to mix, and glycine follows the water into the anti-solvent. At longer times, the activity gradient acts to equalise the compositions across the system resulting in a similar profile to the methanol system, and the system fully mixes. A more detailed comparison of these systems are shown in appendix B.1.

The difference in supersaturation profiles emphasises the role that the solvent choice plays in the mixing process, especially with regards to the influence on the solute behaviour. Nucleation is most probable to occur at peak supersaturation, with differences noted in the supersaturation profiles. Methanol is seen to peak at the channel wall and

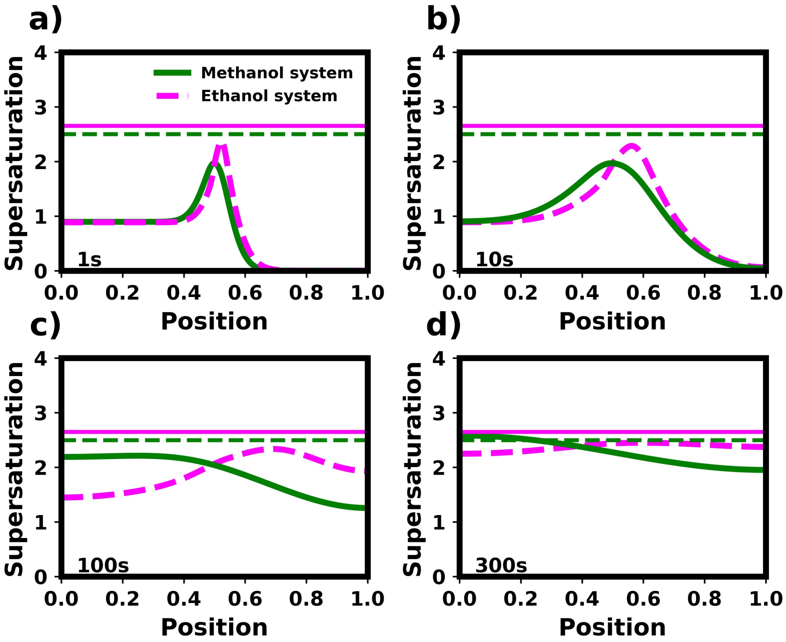

Figure 5.4: Supersaturation profiles highlighting the differences between the anti-solvent systems. Both systems are for 80/20 % v/v anti-solvent/water solvent mixtures mixing with aqueous glycine solution. Initially equal amounts of anti-solvent and solution were present. Temperature was 298K and heat of mixing was neglected. Green and magenta depict the methanol and ethanol system respectively. The plots in (a), (b) (c), (d) correspond to 1, 10, 100, and 300s.

ethanol peaks near the interface as seen previously in chapter 4. If we consider the parametric study in chapter 4 on diffusion coefficients we can see the difference in peak locations can be explained by the different diffusivities. Methanol/water mixes faster than ethanol/water and faster inter-mixing of solvents occur. Solubility is therefore lowered on the solution side and supersaturation increases. With peak values in different locations these two anti-solvents may lead to nucleation under different solution environments, specifically different solvent mixture compositions and the corresponding solute/solvent interactions. This can result in different solid forms and nucleation rates.

### 5.4.3 Liquid-liquid phase separation

For some anti-solvent systems there is the possibility for LLPS, also known as 'oiling out' to occur during the anti-solvents crystallisation processes. This is generally considered undesirable due to the added layer complexity caused by nucleation potentially taking place in oiled out droplets. These droplets can have significantly different fluid composition and resulting crystal properties could differ from those nucleated from the bulk solution . On the other hand, LLPS can give crystals with more desirable properties, with the nucleation environment within the oiled out phase providing better conditions for nucleation. In either case, a better understanding of LLPS will help to improve the design and optimisation of anti-solvent processes. This section will provide insight into the role of diffusive mixing in the occurrence of LLPS.

In chapter 4,[10] we highlighted the possibility of a local LLPS during the diffusive mixing process for non-ideal anti-solvent systems. Here, we consider the differences in compositional trajectories on ternary phase between the methanol and ethanol anti-solvents systems to investigate the effect of anti-solvent choice on LLPS. Figure 5.5 shows an example composition profile across the channel plotted on corresponding ternary phase diagrams (mass based). The black cross indicates the final composition of the channel, which lies outwith of the spinodal regions of both systems. The initial anti-solvent mixture compositions was 90% anti-solvent and 10% solution by volume. The channel was initially filled with 80% v/v anti-solvent and 20% aqueous glycine solution. Under these set of conditions, both systems become meta-stable with respect to glycine crystallisation, i.e. the compositional curves are located in region under the solubility curve. Note that the solubility curve is depicted for the water/methanol system. Due to similar solubility on the mass basis these solubility curves overlap for water/ethanol and water/methanol.[11]

Initially the liquid binodal region is avoided by both anti-solvent systems however, as mixing proceeds (figure 5.5 (c)) the methanol system enters the binodal region (light blue), and the local mixture becomes meta-stable, and two distinct solution phases may coexist. The ethanol system curves around its binodal region (light red), but does not enter at this time. After approximately 150s, the ethanol system hits the spinodal curve and local LLPS is predicted to occur. The simulation is stopped at this time, as phase separation is not modelled in this work. The methanol system continues to mix, with local compositions still in the binodal region and eventually reaches a uniform composition, with no local compositions in the spinodal region being experienced (not shown in figure 5.4).

Composition trajectories were examined using the same approach for a range of initial anti-solvent compositions and initial volume ratios between solution and anti-solvent within the channel. This allows for a prediction of conditions that have the potential to result in LLPS. Figure 5.6 shows a comparison of LLPS parameter space for the two anti-solvents systems, methanol (left) and ethanol (right).

Figure 5.6 shows that when pure anti-solvents are used, LLPS can be expected for solution volume fractions of about 0.2 for methanol, and 0.3 for ethanol. it can be assumed that only regions of high anti-solvent content in the initial anti-solvent mixture will result in LLPS for both systems. Note that conditions outwith the parameter space did not result in LLPS or enter binodal region. The relatively lower amounts of ethanol required for LLPS can be explained by considering the phase diagram. The spinodal region for the ethanol system is larger due to the mixture being more non-ideal and consequently has a wider area of compositions in which the systems becomes unstable. During mixing, the composition profiles across the channel do not significantly change between the two systems, and largely occupy the same region in the phase diagram. With the spinodal region encompassing a greater area less anti-solvent is needed for local compositions to enter this region.

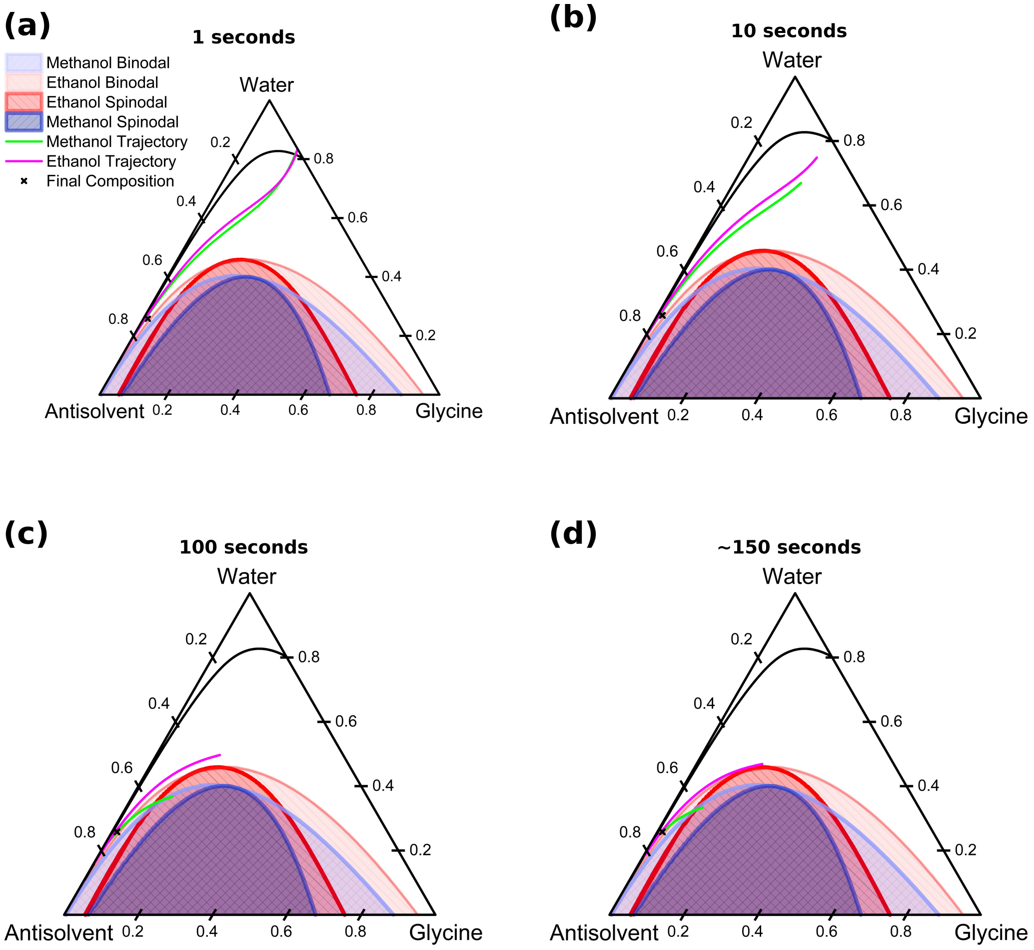

Figure 5.5: Mixing trajectories plotted on mass based ternary phase diagram. Green and magenta lines represent methanol and ethanol systems respectively. Black cross indicates final mixture composition. For both systems, initial anti-solvent composition is 90% anti-solvent, 10% water, and volume ratio is 4:1 anti-solvent:solution within the channel. Initial solution supersaturation is 0.89.

The binodal region was found to be greater in the methanol system. In the binodal region, LLPS can occur although it does not occur spontaneously. For the case of composition trajectories entering the binodal regions on route to the spinodal region, occurrence of phase separation would be dictated by the relative values of mixing and phase separation kinetics. Although phase separation is not modelled, figure 5.6 highlight that local compositions can enter the binodal region during the diffusive mixing process and thus LLPS is possible.

Occurrence of LLPS in relation to anti-solvent crystallisation processes is not uncommon but it usually reported for systems where macroscopic phase separation is observed. That is, the final mixture composition is within the spinodal, or at least the binodal region. However, there may be cases of local LLPS which trigger intermittent phase separation which may even be away from the mixing interface. When the overall mixture

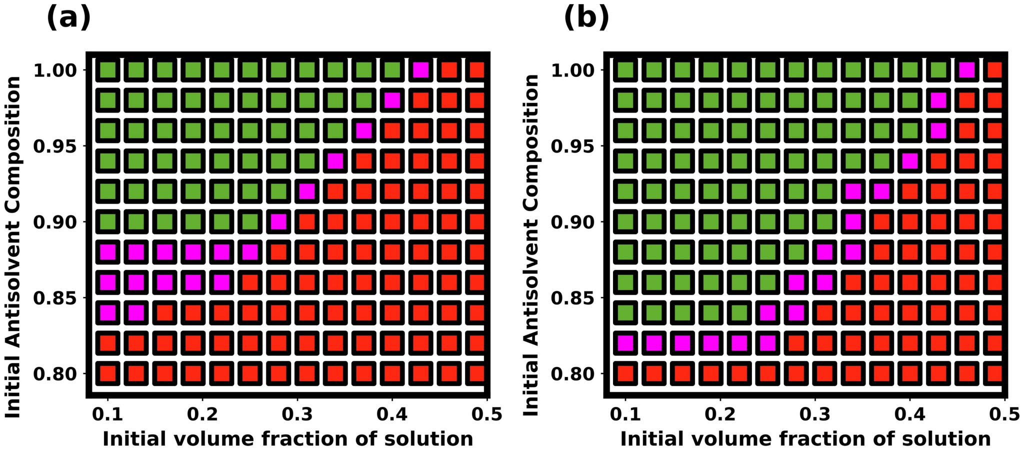

Figure 5.6: Parameter space indicating the combination of initial anti-solvent compositions and solution/anti-solvent ratios that results in localised liquid-liquid phase separation (LLPS), depicted by green squares. Red squares show conditions in which LLPS is not predicted to occur. Magenta indicates local compositions enter the binodal region but not the spinodal. Initial solution supersaturation is 0.89 for all parameter combinations. a) shows methanol system, whilst b) shows ethanol system.

composition is within binodal or spinodal regions, this then may result in macroscopic phase separation. However, if the overall mixture composition is not predicting macroscopic LLPS, intermittent LLPS can still trigger local phase nucleation.

### 5.4.4 Effect of periodic boundary condition

Previously we considered diffusive mixing to occur in a fixed channel with no flux Neumann boundary conditions imposed at the channel walls. This scenario would be most directly related to diffusion processes that take place between two layers of fluid, for example the diffusive mixing of two laminar fluid streams in contact within a microfluidic channel. In turbulent mixing, fluid elements of varying composition are spatially rearranged through macro-mixing processes before turbulent dispersion reduces these to the Kolmogorov scale. Finally further viscous deformation leads to the fluid elements being reduced to the Bachelor scale in which diffusive mechanisms dominates mixing. Fluid elements are surrounded by others of different composition, and representing diffusive mixing at these scales as a fix width channel does not appropriately represent the actual mixing process. To better represent this, we use periodic boundary conditions and diffusion in modelled as a series of anti-solvent and aqueous glycine solution layers. In this approach to model each solution and anti-solvent layer will have the same respective initial composition. Diffusive mixing is simulated at the bachelor length scale to produce a comparison with the fixed channel boundary condition simulations.

Figure 5.7 shows the comparison between supersaturation profiles for periodic and fixed channel boundary conditions for a given set of parameters. In the grey inset, the periodic profile is depicted, with the region in the black box representing one solution and anti-solvent layer. The initial anti-solvent/solution interface is the same for across both boundary conditions and consequently at early times, the supersaturation profiles at the interface overlap. The edges of the periodic boundary condition profile, reflect the periodicity of the system. As time proceeds the profiles begin to diverge and the periodic

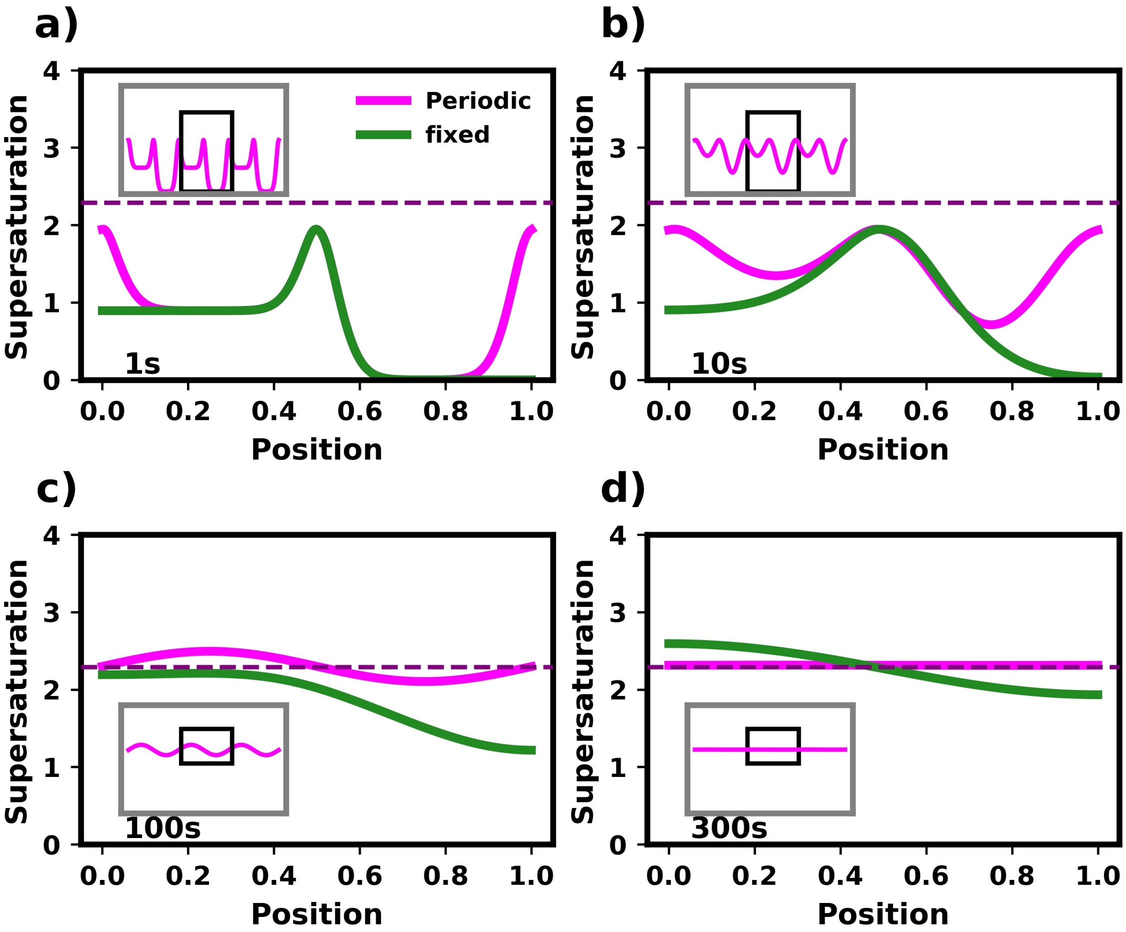

Figure 5.7: Comparison of supersaturation profiles for fixed and periodic boundary conditions. Magenta and green lines indicate fixed and periodic boundary conditions respectively. Magenta dashed line depicts the supersaturation profile at fully mixed composition. The light grey box shows the periodic supersaturation profile, whilst the region enclosed in black is compared with the fixed boundary condition. In this system, 80/20 % v/v methanol/water anti-solvent mixtures was used, with equal amounts of solution and anti-solvent present. Initial supersaturation of the glycine solution was 0.90

boundary condition system mixes at faster. For the fixed boundary condition system, diffusion in each element takes place in only one direction i.e. glycine solution only diffuses

Table 5.4: Mixing time comparison for fixed and periodic boundary conditions. A water/methanol/glycine system is used with conditions corresponding to figure 5.7.

| **% homogenisation** | **Fixed boundary time (s)** | **Periodic Boundary time (s)** |
|---|---|---|
| 99.9 | 1330 | 349 |
| 99 | 946 | 239 |
| 95 | 665 | 168 |
| 90 | 504 | 126 |

into anti-solvent adjacent to it and vice versa. If we consider the solution side of the fixed channel due to the no flux boundary condition. In other words, local compositions away from the solution-anti-solvent interface are unchanged at short time scales after the onset of mixing.

In the periodic system diffusion is expedited by each layer having an interface at either side and less time is needed for local activity gradients to be generated. To compare mixing times between the two boundary conditions we define mixing using the time taken for a specific homogenisation criteria to be met. We will consider characteristic mixing times; when all four components are within 90, 95, 99 and 99.9% of their final fully mixed values. Table 5.4 summaries these times. It can be seen that when periodic boundary conditions are used the mixing time are 1/4 of those for fixed boundary conditions. For a given system diffusive time-scales can be related to length-scale through $t = \frac{L^2}{D}$ where D is the diffusivity. Time therefore scales with the square of length. The factor of 1/4 for periodic vs fixed time scales can be explained through considering the diffusion path length. In periodic boundary conditions the diffusion path would be from the centre of a fluid layer, to the centre of the adjacent layer, whilst in fixed boundary conditions, the diffusion path is from the solution channel wall to the anti-solvent channel wall. This results in periodic diffusion paths being half that of fixed, corresponding to the time scaling to a factor of 1/4 as seen from table 5.4. Regarding compositions experienced during mixing, compositional trajectories in the ternary phase diagram were almost identical for both boundary conditions. Corresponding composition trajectories are shown on mass based ternary phase diagrams in appendix B.2

In periodic conditions considered, the solution/anti-solvent layers are arranged in an alternating manner, with each solution/anti-solvent layer having the same initial thickness and compositions. Whilst this is based on a simplified model of micro-mixing, it produces a qualitative representation of diffusive mixing in turbulent flows. Importantly, it was found that composition trajectories were the same for periodic and fixed boundary conditions, and independent of layer thickness. It can therefore be concluded that local solution composition at diffusive interface between solution and anti-solvent can be expected

### 5.4.5 Discussion on the lenghtscales and timescales turbulent mixing

This section offers a qualitative discussion on how the diffusive mixing model relates to micro mixing models found in literature and at which stage of turbulent mixing our model would be applicable to in terms of lengthscales and timescales. It is worth first defining the appropriate length scales that are used in characterising micro-mixing, namely the Kolmogorov[33, 34] and Batchelor scales,[35, 36] shown in equations 5.7 and 5.8. The Kolmogorov length ($L_k$) scale is the smallest eddy length scale in turbulent flow below which viscous forces dominate mixing. The Batchelor length scale ($L_k$) describes the smallest length scales below which diffusive mixing becomes dominant.

$$L_k = \left(\frac{\nu^3}{\epsilon}\right)^{\frac{1}{4}} \tag{5.7}$$

$$L_b = \left(\frac{\nu D^2}{\epsilon}\right)^{\frac{1}{4}} \tag{5.8}$$

Where $\nu$ is the kinematic viscosity and $\epsilon$ is the turbulent energy dissipation rate. Corresponding time scales can be derived through dimensional analysis and are shown in equations 5.9 and 5.10:

$$t_k = \left(\frac{\nu}{\epsilon}\right)^{\frac{1}{2}} \tag{5.9}$$

$$t_b = \left(\frac{\nu D}{\epsilon^2}\right)^{\frac{1}{4}} \tag{5.10}$$

For turbulent mixing in agitated vessels typical shear rates are in range of 1-10000$s^{-1}$.[37–39] This corresponds to a turbulent dissipation range of $10^{-6}$ - $20^3$. Plots of turbulent dissipation against relevant time and length scales are shown in figure 5.8.

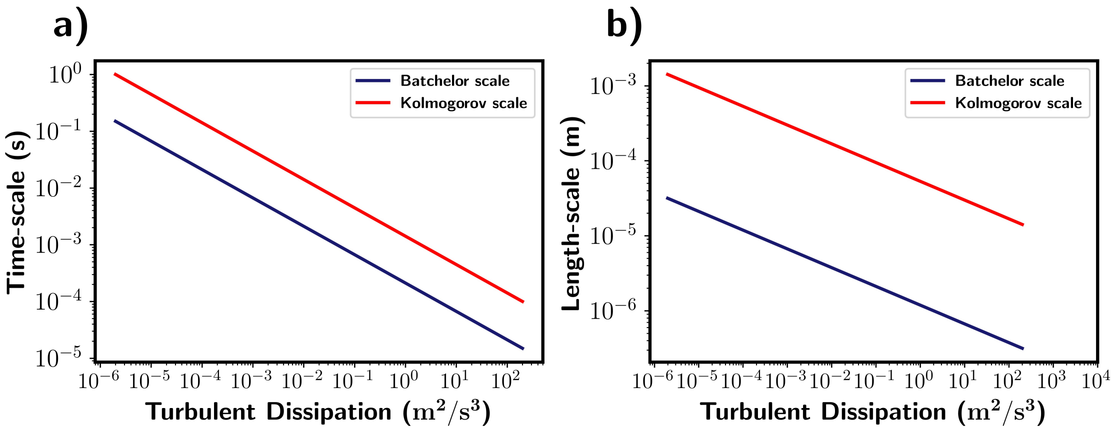

Figure 5.8: A) Kolmogorov (red) and Batchelor (blue) time-scales against shear rates. B) Kolmogorov and Batchelor length scales against dissipation rates. Calculated using equations 5.7-5.10. Viscosity and diffusivity taken as $3.5 \times 10^{-6} m^2/s$ and $1 \times 10^-9m^2/s$ respectively.

From figure 5.8 we see that $L_b$ « $L_k$ where above $L_k$ the main mixing mechanism is inertial due to turbulent dispersion. Between $L_b$ and $L_k$ its viscous to due fluid shear and below $L_b$ the effects of fluid element deformation and stretching by fluid shear/turbulent dispersion become limited and the main mixing mechanism becomes diffusive. On this basis we can conclude that the diffusive model developed in this work is applicable to the final step of the mixing process; molecular diffusion across the fluid elements that have been reduced to the Batchelor length-scale through turbulent dissipation.

To compare the mixing times predicted by our model to the Batchelor time scale, the same mixing time characterisation approach as discussed in section 5.4.4 is used. Diffusion simulations were ran for fluid layer thicknesses of 1, 10, 100 and 1000 microns in which mixing times were found to scale to $L^2$ as expected. The supporting material shows detailed results. Figure 5.9 shows a comparison between our calculated mixing times from simulations and those calculated from equation 5.10. Note that our diffusion simulations are based on equal amounts of aqueous glycine solution and pure methanol anti-solvent by volume. Fixed and periodic boundary conditions are shown.

For a given $\epsilon$, relevant length and time-scales can be determined from figure 5.8. Figure 5.9 shows two subsequent processes; firstly the reduction of Kolomogorov length-scale to the corresponding Batchelor length-scale by turbulent dispersion. Secondly mixing is completed through diffusion with the time estimated by the Batchelor time-scale shown in dark green. For a given length-scale we find that the times predicted by our model when using periodic boundary conditions are close to those predicted by the Batchelor time-scale, with the 95% mixing overlapping the Batchelor scale line. Fixed boundary conditions are approximately four times greater. As crystallisation is significantly influenced by local solution composition, diffusive mixing plays a key role in understanding the effect of mixing on nucleation outcomes. In anti-solvent crystallisation, proper description of multi-component diffusion can therefore provide a more accurate description of diffusive mixing processes and better capture the behaviour of highly non-ideal systems such as those associated with anti-solvent crystallisation. Future improvement on existing micro-mixing models can be realised through the incorporation of multi-component diffusive model to describe the diffusive flux between fluid layers, thus properly accounting for the non-ideality of the system.

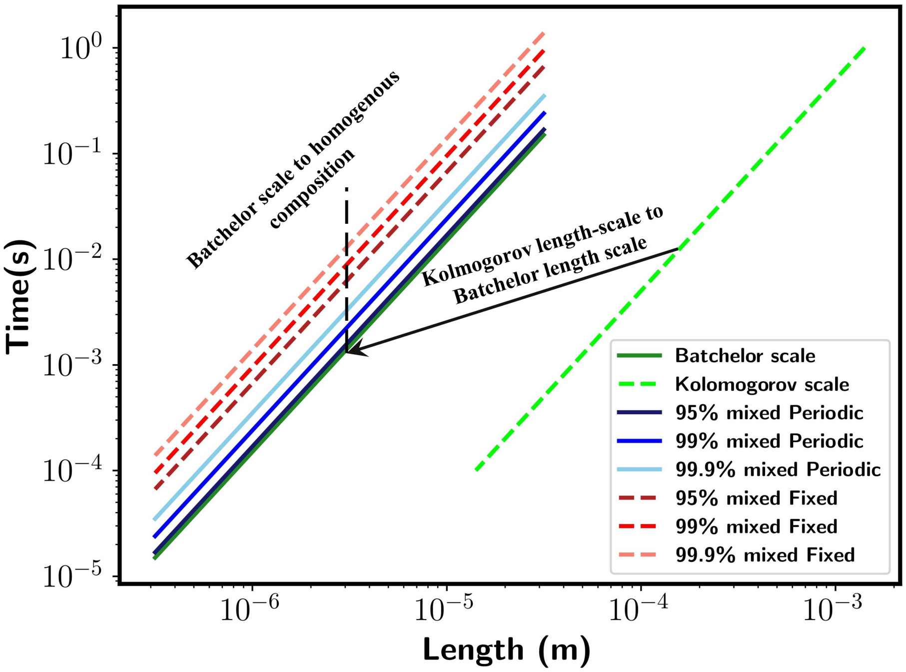

Figure 5.9: Comparison of mixing times predicted by diffusive model and those calculated from Batchelor and Kolmogorov time-scales. For a given shear rate a specific Kolmogorov length-scale exists. Turbulent dissipation and fluid shear reduces this to the Batchelor length-scale and mixing is finished through diffusion. The Batchelor time-scale gives an estimation of this time and is compared to the time predicted by our model. Diffusion simulations are based on equal amounts of aqueous glycine solution and pure methanol anti-solvent by volume.

## 5.5 Conclusions

Using the multi-component diffusion model for non-ideal ternary systems developed in chapter 4, the role of diffusion in anti-solvent crystallisation processes was further explored. Firstly the effects of anti-solvent selection were assessed by a comparative study of two anti-solvent systems; glycine/water/ethanol and glycine/water/methanol. Glycine behaviour was found to be qualitatively similarly in both systems, with the solute diffusing away from the solution/anti-solvent interface as a result of the activity gradients in the system. Supersaturation was however found to peak at different solvent compositions, potentially effecting local nucleation behaviour and the resulting crystal properties. Additionally the occurrence of localised liquid-liquid phase separation (LLPS) during diffusive mixing was investigated for both systems. For both, high anti-solvent volumes relative to aqueous glycine solution led to LLPS. Secondly periodic boundary conditions were implemented and the effects on composition trajectories and mixing times were contrasted to the fixed boundary conditions used in chapter 4. This was to better represent diffusive mixing at the Batchelor scale in which multiple fluid layers are in contact as opposed to just two layers inter-diffusing as described by fixed boundary conditions. It was found that composition trajectories were similar in both cases, however mixing times were significantly shorter in the periodic system due to diffusion across two interfaces. Finally, we discussed lengthscales and timescales turbulent mixing. It was found that Batchelor timescales agrees very well with diffusion mixing timescale from diffusion mixing calculations using periodic boundary conditions.

## 5.6 References

[1] J. Bałdyga and R. Pohorecki. Turbulent micromixing in chemical reactors — a review. *Chem. Eng. J. Biochem. Eng. J.*, 58(2):183–195, 1995.

[2] J. Baldyga and J.R. Bourne. *Turbulent Mixing and Chemical Reactions.* Wiley, 1999.

[3] Y Qu et al. A perspective Review on Mixing Effect for Modeling and Simulation of Reactive and Antisolvent Crystallization Processes. *React. Chem. Eng.*, 2020.

[4] K. W. Mao and H. L. Toor. A Diffusion Model for Reactions with Turbulent Mixing. *AIChE J*, 16(1):49–52, 1970.

[5] Z Mao and C Yang. Micro-Mixing in Chemical Reactors: A Perspective. *Chin. J. Chem. Eng.*, 25(4):381–390, 2017.

[6] J M Ottino, W E Ranz, and C W Macosko. A Lamellar Model for Analysis of Liquid-Liquid Mixing. *Chem. Eng. Sci.*, 34:877–890, 1979.

[7] J. Baldyga and J.R. Bourne. A fluid mechanical approach to turbulent mixing and chemical reaction part ii micromixing in the light of turbulence theory. *Chem Eng Commun*, 28(4-6):243–258, 1984.

[8] J. Baldyga and J.R. Bourne. Simplification of micromixing calculations. i. derivation and application of new model. *J. Chem. Eng.*, 42(2):83–92, 1989.

[9] L X and C G. Simplified Framework for Description of Mixing with Chemical Reactions I: Physical Picture of Micro- and Macromixing. *Chin. J. Chem. Eng.*, 4(4):311–321, 1996.

[10] R Miller, J Sefcik, and L Lue. Modeling Diffusive Mixing in Antisolvent Crystallization.

*Cryst. Growth Des*, 22(4):2192–2207, apr 2022.

[11] L A.I. I Ramakers et al. Investigation of Metastable Zones and Induction Times in Glycine Crystallization across Three Different Antisolvents. *Cryst. Growth Des*, 20(8):4935–4944, aug 2020.

[12] E Wilhelm. Mitigating Complexity: Cohesion Parameters and Related Topics. I: The Hildebrand Solubility Parameter. *J Solution Chem*, 47(10):1626–1709, 2018.

[13] R Krishna. Uphill Diffusion in Multicomponent Mixtures. *Chem. Soc. Rev.*, 44(10):2812–2836, 2015.

[14] D G. Miller, V Vitagliano, and R Sartorio. Some Comments on Multicomponent Diffusion: Negative Main Term Diffusion Coefficients, Second Law Constraints, Solvent Choices, and Reference Frame Transformations. *J. Phys. Chem. A*, 90(8):1509–1519, 1986.

[15] L Hao and D G. Leaist. Binary mutual diffusion coefficients of aqueous alcohols. methanol to 1-heptanol. *J. Chem. Eng. Data*, 41(2):210–213, 1996.

[16] G Chen, Y Hou, and H Knapp. Diffusion coefficients, kinematic viscosities, and refractive indices for heptane + ethylbenzene, sulfolane + 1-methylnaphthalene, water + n,n-dimethylformamide, water + methanol, water + n-formylmorpholine, and water + n-methylpyrrolidone. *J. Chem. Eng. Data*, 40(4):1005–1010, 1995.

[17] Z. J. Derlacki et al. Diffusion coefficients of methanol and water and the mutual diffusion coefficient in methanol-water solutions at 278 and 298k. *J. Phys. Chem*, 89(24):5318–5322, 1985.

[18] L Chang, T-I Lin, and M-H Li. Mutual diffusion coefficients of some aqueous alkanolamines solutions. *J. Chem. Eng. Data*, 50(1):77–84, 2005.

[19] S Parez et al. Mutual Diffusion in the Ternary Mixture of Water + Methanol + Ethanol and its Binary Subsystems. *Phys. Chem. Chem. Phys.*, 15(11):3985–4001, mar 2013.

[20] H-J Bosse, Dand Bart. Prediction of Diffusion Coefficients in Liquid Systems. *Ind. Eng. Chem. Res.*, 2006.

[21] K R. Harris, T Goscinska, and H N Lam. Mutual diffusion coefficients for the systems water–ethanol and water–propan-1-ol at 25 $^0$c. *J. Chem. Soc., Faraday Trans.*, 89:1969–1974, 1993.

[22] A Leahy-Dios and A Firoozabadi. Molecular and Thermal Diffusion Coefficients of Alkane-Alkane and Alkane-Aromatic Binary Mixtures: Effect of Shape and Size of Molecules. *J. Phys. Chem. B*, 111(1):191–198, 2007.

[23] K. J. Zhang et al. Optical Measurement of the Soret Coefficient and the Diffusion Coefficient of Liquid Mixtures. *J. Chem. Phys*, 1996.

[24] J E Guyer, D Wheeler, and J A Warren. FiPy: partial differential equations with python. *Comput. Sci. Eng.*, 11(3):6–15, 2009.

[25] J. A. V. Butler, D. W. Thomson, and W. H. Maclennan. 173. the free energy of the normal aliphatic alcohols in aqueous solution. *J. Chem. Soc.*, pages 674–686, 1933.

[26] K A Dulitskaya. Vapor Pressure of Binary Systems. I. *Russ.J.Gen.Chem*, 15:9–21, 1945.

[27] D. J. Hall, C. J. Mash, and R. C. Pemberton. Vapor Liquid Equilibriums for the Systems Water-Methanol, Water-Ethanol, Methanol-Ethanol, and Water-Methanol-Ethanol at 298.15 K Determined by a Rapid Transpiration Method. Technical Report NPL-Chem-95, National Physical Lab, 1979.

[28] Z S. Kooner, R C. Phutela, and D V. Fenby. Determination of the Equilibrium Constants of Water-Methanol Deuterium Exchange Reactions from Vapour Pressure Measurements.

*Aust. J. Chem*, 33(1):9–13, 1980.

[29] J. M Guilherme, J.A. M Antonio, and A.C. B Eduardo. Boiling point of aqueous d-glucose and d-fructose solutions: Experimental determination and modeling with group-contribution method. *Fluid Ph. Equilibria*, 299(1):32–41, 2010.

[30] T E Needham. *The Solubility of Amino Acids in Various Solvent Systems.* PhD thesis, University of Rhode Island, Kingston, RI, 1 1970.

[31] K Gekko. Mechanism of Polyol-Induced Protein Stabilization: Solubility of Amino Acids and Diglycine in Aqueous Polyol Solutions. *J. Biochem.*, 90(6):1633–1641, 10 1981.

[32] Y Zeng, Z Li, and G P. Demopoulos. Phase equilibria for the glycine–methanol –nh4cl–h2o system. *Ind. Eng. Chem. Res.*, 53(43):16864–16872, 2014.

[33] A. N. Kolmogorov. The local structure of turbulence in incompressible viscous fluid for very large reynolds numbers. *Proc. USSR Acad. Sci.*, 30:301–305, 1941.

[34] J Jiménez. The contributions of a. n. kolmogorov to the theory of turbulence. *Arbor*, 178:589–606, 08 2004.

[35] G. K. Batchelor. Small-scale variation of convected quantities like temperature in turbulent fluid part 1. general discussion and the case of small conductivity. *J. Fluid Mech.*, 5(1):113–133, 1959.

[36] E. L. Paul, M Midler, and Y Sun. *Mixing in the Fine Chemicals and Pharmaceutical Industries. Handbook of Industrial Mixing.* Wiley & Sons, 2004.

[37] S Miroslav et al. Effect of shear rate on aggregate size and morphology investigated under turbulent conditions in stirred tank. *J. Colloid Interface Sci.*, 319(2):577–589, 2008.

[38] D L. Marchisio et al. Role of turbulent shear rate distribution in aggregation and breakage

processes. *AIChE J*, 52(1):158–173, 2006.

[39] N Alderman. Non-newtonian fluids: Guide to classification and characteristics. Technical report, 12 1997.

# Chapter 6

# Mixing Times of Miscible Liquid Systems in Agitated Vessels

## Comment on contributions to chapter

This chapter details the research output from a industrial placement with Takeda. It was originally planned for the placement to completed onsite in Boston, US, however due to Covid-19 travel restrictions this was not possible. A collaborative effort between myself and a placement student situated onsite at Takeda was necessary to mitigate the disruption caused by Covid. Table 6.1 outlines the contributions of the individuals associated with this project.

Table 6.1: Summary of individual contributions to the work reported in this chapter. UoS and T refers to the University of Strathclyde and Takeda respectively.

| Contribution | Person/s |
|---|---|
| Experimental work | Isabella Cardona Barber |
| Experimental data analysis | Russell Miller & Isabella Cardona Barber |
| Mstar CFD | Russell Miller |
| Dynochem | Isabella Cardona Barber |
| Writing of manuscript | Russell Miller |
| Supervisors | Neda Nazemifard (T.), Jan Sefcik (UoS) & Leo Lue (UoS) |

## 6.1 Introduction

In pharmaceutical manufacturing, heat and mass transfer significantly influence the performance of the manufacturing process steps, such as the synthesis or crystallisation. These transport phenomena are influenced by agitation in vessels, with mixing conditions varying widely across development stages and process steps; thus mixing is an important aspect of process design. Crystallisation processes are particularly sensitive to mixing, as temperature or concentration gradients can produce in-homogeneity in the prevailing level of supersaturation. This can result in regions of high supersaturation close to the walls of the vessel in cooling crystallisation, or at the addition location for anti-solvent or reactive crystallisation processes. This affects crystallisation outcomes and can lead to scaling on vessel walls or inlet ports.

Mixing time is considered as one of the most important factors in assessing the performance of agitated systems. Mixing time can be defined as the time required for achieving a certain degree of homogeneity of tracer inserted in a stirred vessel.[1] Computational fluid dynamics (CFD) can be used to estimate mixing times and provide further insight into how different mixing configurations influence supersaturation gradients within a crystallisation vessel. CFD can therefore be used to develop strategies for the rational scale up of processes involving mixing of miscible liquids, such as anti-solvent crystallisation. However, these models require validation to assess the reliability and accuracy of predicted outcomes. This can be achieved by comparing the models to the relevant experimental data. Previously Oblak et al. performed a digital twinning process for stirred tank reactors through tandem experimental and CFD simulations to evaluate mixing in baffled and unbaffled vessels. A single liquid system of distilled water was used.[2] In their work, it was found that the system geometry influenced the mixing time: irregular flow distribution can lead to local stagnation zones thereby increasing the time needed to achieve the homogenisation of the liquid phase composition. It was also found that measuring local, point-wise concentrations can lead to an underestimation of the global mixing time required for the homogenisation of the entire vessel. In another paper, mixing times were predicted for miscible solvents using a CFD approach, which was qualitatively compared to experimental work.[3] The characterisation of mixing from pilot to manufacturing scale using an experimental and CFD hybrid approach was developed by Martinetz et al.[4] This approach enabled mixing times to be correlated to vessel filling volume and vessel-averaged energy dissipation rate for single phase systems.

There are many experimental techniques that can be used to characterise mixing times in agitated vessels, with varying degrees of accuracy and reproducibility . When categorising mixing characterisation techniques, they can be divided into two groups, based on the volume of fluid represented by the measurement.[5] The first of these are local techniques, in which only localised measurement using fixed probes are provided. Mixing times are then estimated based on a set homogenisation criteria for example a property such as conductivity to reach 95% of the fully mixed value. Whilst they are simple to implement, provide direct measurements, and can be used for transparent and opaque fluids, they are intrusive and disturb the measured flow fields. Additionally, the resulting mixing time is dependent on the probe position, and care must be taken in selecting a location that is representative of mixing times.[6, 7] To obtain more spatial information on the process, multiple probes can be used together. Another characterisation technique is the application of planar laser-induced fluorescence (pLIF) combined with image analysis. Here, the measurements are made on the laser plane and only a limited spatial resolution is provided. Advantages of this technique include the non intrusiveness with regards to the fluid, and the provision of detailed visualisation of fluid structures and mixing patterns of the systems. Applications of pLIF are limited by the difficulty in calibrating, and high laser power/costs associated with large volumes or opaque fluids.[8, 9]

Global mixing characterisation methods offer spatial information on the whole vessel, and can provide quantitative information on the on global flow structures and highlight regions of poor mixing. One such method is colorimetry, in which colour changes are used to determine mixing times. For example fast acid-base reactions involving colour changes.[5, 10] Further advantages of this method are its non-intrusiveness, simple implementation, and limited calibration requirements.[6, 11] Accuracy of this method can be improved when combined with image analysis technique to quantify the colour change process and define individual RBG model criteria to define the end of mixing.[5, 12] Liquid crystal thermography can be used to induce colour changes in vessels[6, 12, 13] . Thermochromic liquid crystals are suspended in the liquid and thermal pulse is given. The resulting mixing of this pulse leads to the crystals exhibiting a different colour depending on the local temperature. Temperature profile of the vessel is then determined using the crystal colours and is used as the scalar to characterised mixing. Image processing is typically used to analyse results to more accurately quantify the evolution of colour change.

Electrical resistance tomography (ERT) is a non-invasive method based on conductivity, and typically used for solutions that have a distinct conductivity change upon mixing.[5, 14] Through capturing a series of 2D tomograms, ERT is capable of proving a visualisation of 3D flow fields, allowing for good spatio and temporal resolution of the system to be obtained. The cost and complexity in setting up ERT is considerable, and as such is mainly used for applications in which detailed flow fields are required for example mixing characterisation in concentrated slurries,[15] or to determine gas/liquid flow patterns,[16] as opposed to characterising mixing times of vessels.

Whilst optical methods such as colorimetry are relatively simple, they can only be applied to optically transparent vessels and fluids, significantly limiting their in industrially relevant geometries.[17] Although tomography can provide detailed information on flow patterns, it has several practical drawbacks when using manufacturing equipment, such as the limited space for sensor installation, waste material treatment and strict regulations for equipment in a GMP environment.[17] Local mixing characterisation techniques such as probe-based methods are an attractive option due to the relative easiness of application to industrial vessels - i.e. the insertion of the probe being straight-forward in most cases. The main disadvantage of using probe is that only local flow properties are measured, leading to limited spatial and temporal information being provided on the measured quantity. To account for this during measuring mixing time determination, careful consideration must be taken on deciding placement of the probe. A position should be used that gives a good representation of global mixing time within the vessel. The probe sensor response time should be fast in comparison to mixing kinetics, and a data measurement frequency of at least once per second recommended.[4] Mixing times in agitated vessels can be determined using tracers tests, with probes being used to provide information on the measured variable, such as Ph or conductivity. In this work we use the conductivity method, which involves the addition of a salt tracer and measuring the conductivity increase within the vessel. Mixing time can be determined once the conductivity fluctuations are less than 5% of the homogenised value, referred to as the 95% mixing assumption.[18]

Anti-solvent crystallisation involves mixing of miscible liquids with different viscosities and densities, which can influence mixing phenomenology and kinetics in agitated vessels. Bouwmans et al. presented work on the influence of viscosity and density differences on mixing times in stirred vessels.[19] To vary the viscosity and density independently, mixtures of water, ethanol and glycerol were used in which Poly-Vinyl-Pyrrolidone (PVP) was dissolved to achieve the desired viscosity allowing for systems ranging from 1 mPas to 200 mPas and 900 kg/m$^3$ to 1100 kg/m$^3$ respectively. Under certain conditions, they found that mixing time can be unpredictable due to the turbulent nature of flow leading to mixing time standard deviations of over 50%. Their conclusions were based on the case of a less dense liquid being added to the surface of bulk liquid can be summarised as follows: Relatively short mixing times with a large relative standard deviation were found at high stirrer speeds whilst longer mixing times with small relative standard deviation were found at low stirrer speeds. In the transitional region, both mechanisms are at work giving low mixing time predictability and large relative standard deviations.

This work aims to extend previous work on mixing characterisation in agitated vessels to miscible liquid systems with the focus on the mixing a common solvent-anti-solvent pair water and ethanol within a 1 litre agitated vessel. A combined experimental and CFD approach is taken. Two scenarios are considered; firstly the addition of a tracer to premixed water/ethanol solvent mixtures and secondly the addition of ethanol to water. Multiple mixing time characterisation methods are applied to both the experimental and computational data, allowing for comparison and contrasting of various approaches and highlighting the inherent associated with mixing times.

The remainder of this paper will be organised as follows; In the methods section we describe the experimental methods and CFD. The results and discussion section is divided into three subsections; mixing time characterisation, mixing times in premixed water/ethanol solvent mixtures, and the addition of ethanol to water. The main outcomes of the work are then summarised in the conclusion section.

## 6.2 Methods

### 6.2.1 Experimental

In this article, we investigate mixing times of miscible solvent systems in a 1L stirred vessel. The miscible liquids were selected to represent a common anti-solvent pair, water and ethanol system. Crystallisation is not considered in this work, and no solute is present within the system. Two distinct cases were considered, one in which the solvents are 'premixed', and the other where we investigate the addition of ethanol to water. For the former, water and ethanol are mixed prior to the salt tracer being added, with sufficient time given to ensure a fully homogenised solution. Salt tracer is then injected as a concentrated aqueous solution at the surface of the solvent mixture. In the latter, salt tracer is added to either the solvent or anti-solvent before mixing the solvents. Conductivity as a function of time is measured during the mixing process, allowing for mixing times to to be determined. The subsequent section will describe the experimental procedure and setup used in this work.

#### 6.2.1.1 Mixing vessel set-up

The Mettler Toledo Optimax 1001 Thermostat System was utilised for all experiments without the use of baffles. The total volume was kept constant at 1 L. A metal downward pitched-blade (Metter Toledo 103504) with four blades at 45°was used. The impeller had a 45 mm outer diameter and was positioned 19 mm above the bottom of the vessel. Two probes (conductivity and temperature) were placed 38 mm from the bottom of the vessel and positioned at 30°angles. The conductivity probe (Mettler Toledo InPro 7100(i) Series) was connected to an external logger to record measurements every 0.1s. The temperature probe measured the temperature of the vessel contents. The vessel jacket temperature was also recorded. Figure 6.1 shows a schematic of the vessel set up.

Table 6.2: Summary of vessel and components used in experimental section if this work. Component number relates to figure 6.1.

| Component | Details |
|---|---|
| 1. Temperature Probe | 3.2mm O.D. , 175mm length |
| 2. Conductivity Probes | 12mm O.D.,225mm length |
| 3. Impeller shaft | 8mm O.D. |
| 4. Pitch-blade impeller | Outer angle 45mm, downward, four blades, 45 ° |
| 5. Optimax 1litre vessel | 101mm I.D., 172mm height, 3mm wall thickness |
| 6. Tracer injection | Tracer/solvent injection location |

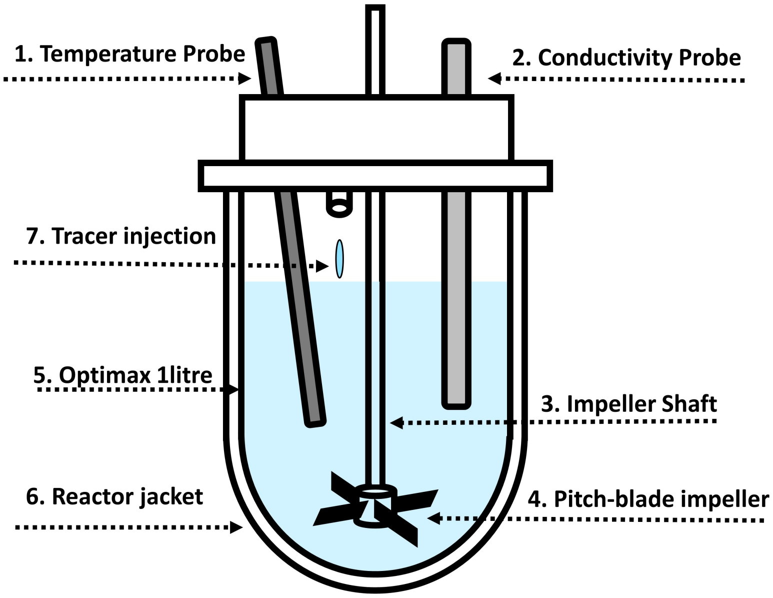

Figure 6.1: Schematic of the Mettler Toledo Optimax 1001 thermostat system. A metal downward pitched with 4 blades with OD of 45mm is placed 19mm above the bottom of the vessel. Two probes (conductivity and temperature) were placed 38 mm from the bottom of the vessel and positioned at 30°angles. Numbers correspond to components in table 6.2 where geometries used in the experimental work are summarised.

#### 6.2.1.2 Tracer tests

Sodium chloride (NaCl) was dissolved in distilled water to prepare 1M salt tracer solution. Solvent mixtures used in all experiments comprised of water and ethanol, with relative ratio of water to ethanol varied.

**Premixed solutions**: The vessel was filled with 1L of premixed water/ethanol

Table 6.3: Table of solution compositions investigated for premixed experiments. Density and viscosity were calculated by fitting a cubic spline to literature data. Note each composition was performed for a range of RPM values ranging from 150 to 750 in increments of 50.

| Fluids | Composition | Density | Viscosity | Re Number Range |
|---|---|---|---|---|
| - | % v/v | ($kg/m^3$) | ($mPa.s$) | - |
| Water | 100 | 998 | 1 | 5040-25200 |
| Water/Ethanol | 80/20 | 974 | 1.8 | 2730-13650 |
| Water/Ethanol | 60/40 | 947 | 2.6 | 1830-9170 |
| Water/Ethanol | 40/60 | 908 | 3.01 | 1895-9480 |

solution, and steady-state was achieved in terms of temperature (20°C) and velocity field/vortex formation. 10ml of tracer solution was then injected at the liquid surface, with care taken to ensure the addition location is consistent across each run. Figure 6.1 indicates the approximate tracer injection location. Injection of the tracer was repeated four times to determine the variability of mixing times within the vessel. This procedure was followed for a range of water/ethanol compositions as shown in Table 6.3 which details the solution compositions investigated along with relevant physical properties given. Each set of conditions was repeated for RPMs values ranging from 150 to 750 in increments of 50. The range of impeller Reynolds numbers for each solvent composition are shown as well, indicating which regime mixing takes place. Impeller Reynolds number is defined in equation 6.1, where $\rho$ is density (kg/m$^3$), N is impeller rotation speed (s$^{-1}$) , D is impeller diameter (m) and $\mu$ is dynamic viscosity of the liquid phase.

$$Re = \frac{\rho N D^2}{\mu} \tag{6.1}$$

**Mixing solvents**: The vessel was initially filled with 800ml of water, before the impeller was started and temperature was set to 20°C. After steady state was reached, 200ml of ethanol was added at the liquid surface. Extra precaution was taken during the ethanol addition to minimise the variance between trials. Once more, each condition was run for RPM values ranging from 150 to 750RPM in increments of 50. Three repetitions per RPM value were performed. The salt tracer solution was added to the ethanol prior to mixing of the solvents. For each RPM, a single experiment was performed with the salt tracer initially being in the water, prior to mixing. This was to determine the effect of initial tracer location on mixing time determination. For both tracer locations, the amount of NaCl tracer solution added to the anti-solvent was 0.05 vol %. Once more, local conductivity was measured by the probe, and used to determine mixing times.

### 6.2.2 Computational

#### 6.2.2.1 CFD geometry

The experimental set-up was modelled using Mstar, with vessel dimensions corresponding to those shown in table 6.2. Figure 6.2 shows the corresponding CFD geometry. Probe and tracer locations were based on those used in the experimental set-up. Tracers were added in the CFD simulations as scalar quantities, where it is assumed that the tracers do not interact with the fluid, and follow local fluid streamlines. To model the conductivity probe sensor in the CFD simulation, a virtual 'probe' was attached at the end of the conductivity probe. This allows for fluid properties such as tracer concentration to be measured at that local position.

To investigate the effect of tracer injection location, additional simulations were run which included five tracers being injected at various locations. These are shown as squares in figure 6.2, with the colour relating to the tracer location. For all other simulations, tracer location two (red) is used, to match that used experimentally. In the solvent mixing experiments, ethanol was poured into the vessel. To approximate this in the CFD model, we take the diameter of the ethanol stream to be 1cm and an addition time of 4s. The volumetric flow rate of ethanol was therefore 50ml/s.

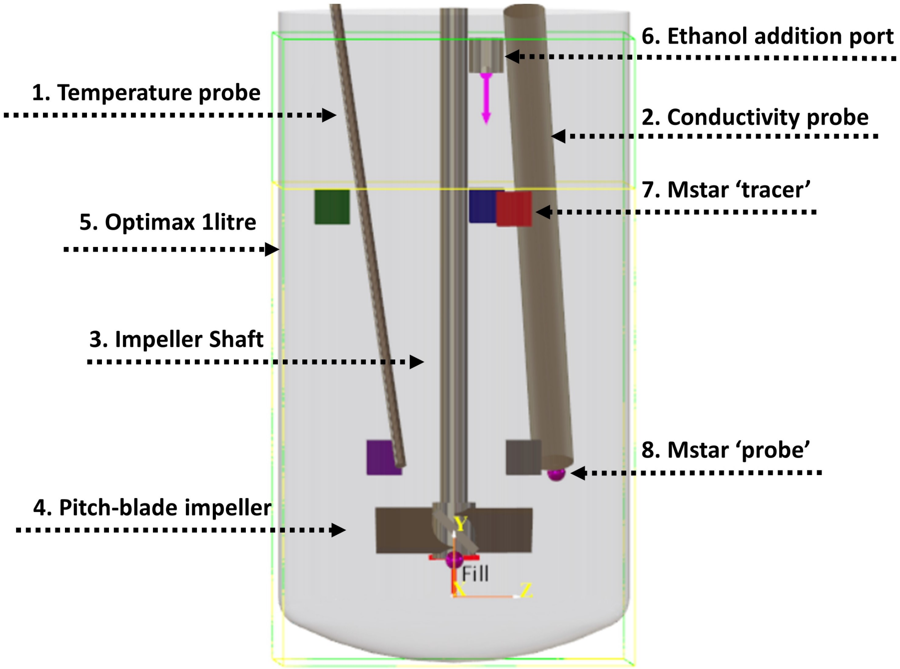

Figure 6.2: Representation of the mixing vessel and probes used as modelled using Mstar. Probe and tracer injection locations correspond to those used experimentally. Dimensions correspond to those detailed in table 6.2. The coloured squares represent tracer injection locations used in the simulations to investigate the effect of this on mixing time. These are labelled as follows; 1.green, 2.blue, 3. red, 4. purple and 5. grey. Note that tracer 2 is used for all premixed simulations. Ethanol addition port refers to the addition of 200ml of ethanol to the water in the solvent mixing simulations. Yellow line shows initial liquid height for a volume of 1litre, that is used for the premixed simulations. The light green box indicates the simulated geometry volume.

#### 6.2.2.2 CFD simulations

CFD simulations were performed using the commercial software package M-star CFD (3.3.96).[20] M-Star CFD uses a Lattice-Boltzmann approach to solve the time-dependent Naiver-Stokes equation.[21, 22] Here, the Boltzmann transport equation is solved to model the time-dependent molecular probability density function ($'f'$) in phase space [1, 2]. This is expressed through equation 6.2.

$$\frac{\partial f}{\partial t} + \zeta \nabla_x f + K \nabla_\zeta f = Q(f, f) \tag{6.2}$$

where, $\zeta$ are the molecular velocity vectors, $K$ denotes any external forces acting on the particles, and $Q(f, f)$ is the collision operator. $Q(f, f)$ describes the rate of change over time in the molecular probability density function for species f with respect to collisions with species f. This becomes complicated for an n-body system, however, it can be argued that the result of multi-body collisions is for local distributions to tend to an equilibrium distribution ($f^0$). Equation 6.2 is then expressed through:

$$\frac{\partial f}{\partial t} + \zeta \nabla_x f = -\frac{1}{\tau}\left(f - f^0\right) \tag{6.3}$$

Where $\tau$ represents the relaxation time which describes how quickly the local distribution relaxes to its equilibrium state. Viscosity is therefore related to the relaxation time, with a larger time relaxation time corresponding to a higher viscosity Macroscopic properties such as density or momentum can be calculated from the moments of the distribution function. In M-star the molecular velocities are discretized into the velocity vector set D3Q19,[20] as this gave the best balance between stability and speed of solver.

For all simulations, the free surface model was selected. In this model, a free-slip boundary condition is imposed at the fluid surface, whilst the vessel walls are assumed to have no-slip boundary conditions. Fluid-impeller interactions are modelled using the immersed boundary method, which enforces a no-slip velocity along the surface of the impeller. The turbulence model used was the Large Eddy Simulation (LES) model with the default Smagorinsky coefficient of 0.1. To ensure lattice density fluctuations were kept within 1%, time steps were chosen to obtain a Courant number of 0.01. A lattice spacing of 0.65mm was used.

Viscosity of the fluid mixture was calculated through a user defined function. This was in the form of a polynomial which was fitted to literature data.[23] M-star assumes volume averaged density, which for our system gives a reasonable approximation. Figure 6.3 shows the properties of the fluid mixtures used here as a function of composition. Surface tension was taken from literature for the solvent mixtures used.[23]

Diffusion was modelled as ideal using the binary Fickian diffusion coefficient for water/ethanol. Although chapters 4 and 5 previously highlighted the importance of modelling diffusion using a non-ideal approach to better predict localised composition profiles at short length scales, a Fickian approach was deemed sufficient for this chapter. Firstly, here we are concerned with characterising macroscopic mixing times and their variability, rather than micro-mixing times. The timescales for macroscopic mixing are many magnitudes greater than corresponding micro-mixing times and as a consequence would not have a significant impact on calculated mixing times. Secondly, the scope of this chapter was to compare mixing characterisation techniques and times. Local composition profiles were not considered in detail. Lastly only the mixing of water/ethanol is considered here and no solute is present in the system. Non-ideal effects would be greatly diminished in a binary system of water/ethanol. With these reasons in mind, it was decided that a Fickian approach to diffusion in this case, provided a reasonable approximation.

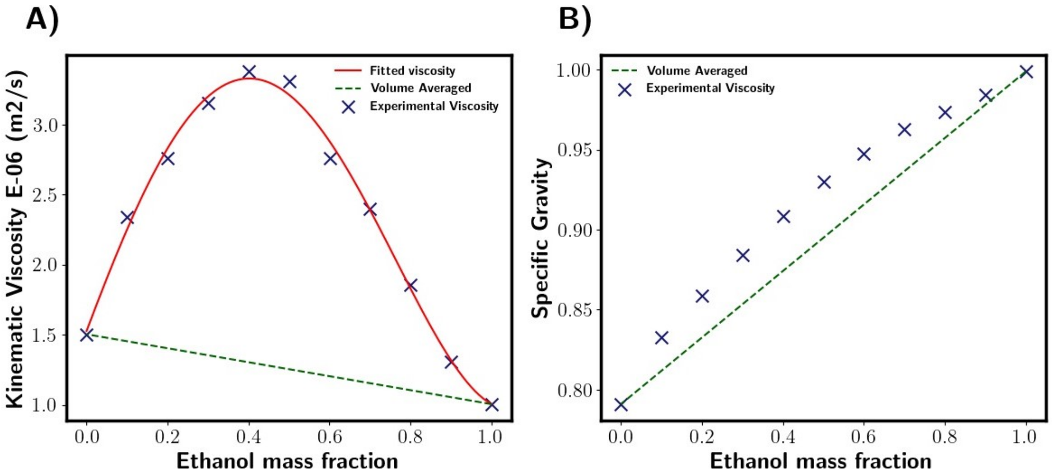

Figure 6.3: Fluid Properties as function of liquid composition.[23] A) Viscosity B) Density. Mstar uses fitted viscosity function whilst DynoChem uses volume averaged (green dashed line). Both software packages assume density is volume averaged.

#### 6.2.2.3 Dynochem

A mixing and heat transfer toolbox, a spreadsheet based software from Dynochem was also used to estimate mixing time. Calculated mixing time is based on the time required to blend a tracer into the bulk such that the additive is 95 % homogenised. The Mixing time correlations for the turbulent (eqn 6.4) and transitional (eqn 6.5) regime are given as such:[24–28]

$$\theta = 5.4\left(H/T\right)\right)^{1.4}\left(V/\left(T^2H\right)\right)^{-1/3}\epsilon^{-1/3}\left(T/D\right)^{1/3}T^{2/3} \tag{6.4}$$

$$\theta = 38025\left(V/\left(T^2H\right)\right)^{-2/3}\epsilon^{-2/3}\mu/\rho_L\left(T/D\right)^{2/3}T^{-2/3} \tag{6.5}$$

Where $\theta$ is mixing time (s), $\epsilon$ is is power per unit volume (kW/m$^3$), $T$ is tank diameter (m), $D$ is impeller diameter (m), $\mu$ is liquid viscosity (Pa s), $H$ is liquid height (m), $V$ is liquid volume ($m^3$), and $\rho$ is liquid density (kg/m$^3$). N represents the impeller rotational speed (1/s). Power input $P$, (W) is calculated using the equation 6.6, with a power number ($P_o$), dependent on impeller choice. From this, power per unit volume ($\epsilon$) is calculated,i.e. $\epsilon = P/V$. In the turbulent regime it is seen that mixing time ($\theta$) is inversely proportional to N, the impeller speed. In the transitional regime, ($\theta$) is inversely proportional N$^2$.

$$P = P_o \rho N^3 D^5 \tag{6.6}$$

DynoChem assumes that the tracer has similar physical properties (i.e. density and viscosity) to the bulk. The correlations are valid for both turbulent ( Re $>$ 2 x 10$^3$) and transitional phases (200 $<$ Re $<$2 x 10$^3$), but not for the laminar phase. Note that Re is impeller Reynolds number given by equation 6.1. The correlations used have been tested over a wide range of scales at different operating conditions with different impellers and the typical error in the turbulent correlation is +/- 14%.[26] For solvent mixtures, Dynochem assumes fluid properties are a volume average of the solvents used, in this case water and ethanol. Figure 6.3 shows the viscosity and density used. One interesting consequence of using volume averaged viscosity is that all mixing conditions have Reynolds numbers above 2000, suggesting turbulent conditions. If we use the actual viscosity data, some solvent compositions at lower RPM are in the transitional regime. This has an effect on calculated mixing times, as Dynochem uses different correlations for the turbulent and transitional regime (equations 6.4 and 6.5). Geometries used in the calculations are given in table 6.4;

Table 6.4: Table of Parameters used in Dynochem Calculations. The range corresponds to that experienced by the various water/ethanol compositions.

| Parameter | Nomenclature | Value |
|---|---|---|
| Tank diameter | T | 101mm |
| Impeller diameter | D | 45mm |
| Viscosity | $\mu$ | 1.14-1 mPaS |
| Impeller speed | N | 150-750RPM |
| Liquid density | $\rho$ | 914-1000 $kg/m^3$ |
| Liquid height | H | 0.135m |
| Liquid Volume | V | 1 litre |
| Power number | Po | 1 |

### 6.2.3 Mixing time characterisation

#### 6.2.3.1 Experimental

**Premixed solutions**: We consider three mixing time estimation methods based on the conductivity profiles obtained from the probes; 95% homogenisation method, and fitting exponential and first order plus dead-time models to the probe data. In all methods, conductivity profiles obtained from the tracer tests were used to characterise mixing times under varying conditions. Figure 6.6 demonstrates the mixing time definitions. In the 95% homogenisation method the end of mixing, was when the conductivity value was within +/-5% of the final steady-state value. The final steady-state value is taken as the plateau of the conductivity profile. The start of mixing was taken as the time in which the conductivity increase is first detected by the probe. To do this, a Savitzky-Golay filter was fitted to the conductivity data, and the first derivative with respect to time was calculated. This was then used to quantify the rate of change of conductivity within the system, allowing for the start of mixing to be estimated. The start of mixing was taken as when the derivative became greater than 0.1 $\frac{mS}{cm}/s$ as this indicated a rapid increase in conductivity. For the other two methods of mixing time estimation, two equations were fitted to the conductivity profiles, first of which was the exponential model:

$$C(t) = A.(1 - exp(-K.t)) \tag{6.7}$$

where A is a fitted constant and represents the steady-state conductivity value and $K$ is the time constant. A higher value of $K$ corresponds to faster mixing time. The exponential function was fitted from the start of mixing. With the start of mixing being defined as described in the 95% homogenisation method.

The conductivity probes only detects the local conductivity at the probe location, resulting in a delay between the tracer being injected at the surface and the increase in conductivity being realised. In order to account for this and avoid estimating the start of mixing, a first order plus dead-time model (FOPDT) is fitted to the conductivity profiles.

$$C(t > t_d) = A.(1 - exp(-(t - t_d)K)) \tag{6.8}$$

In equation 6.8, A is a fitted constant, again representing the steady-state conductivity. $t_d$ is the delay time, whilst K is the time constant. From both of these equations, the time for 95% homogenisation is calculated, allowing for comparison with the 95% homogenisation method.

**Mixing Solvents**: We use the same approach as for premixed solvents with one additional consideration. When solvents are mixed together heat is released due to enthalpy of mixing which lead to a temperature increase of the solvent mixture. Although the vessel is temperature controlled, temperature measurements indicated an increase during mixing. Conductivity is a function of temperature and thus this was accounted for through a temperature calibration model. Details are shown in appendix C1.

#### 6.2.3.2 Computational

**Premixed solvents**: Mixing times obtained by Mstar were characterised using two different mixing indexes, both being based on the tracer concentration. Firstly the relative standard deviation (RSD) of the tracer concentration (mol/litre) is calculated to measure the overall degree of mixing within the vessel. In this work, we consider the system to be fully homogenised when the RSD value drops below 5%.[2, 18] Figure 6.4A shows RSD as a function of time with the green dashed line highlighting when mixing is determined to be complete.

Although the RSD gives an good indication of the degree of mixing in vessel, it does not offer a direct comparison to experimental results from this work. Experimentally, tracer concentration was measured using a conductivity probe, resulting in only localised conductivity profiles being readily available. In order to directly compare computational and experimental results, a 'probe' was added to the CFD geometry in a position to match the experimental set-up. This recorded the local tracer concentration every 0.1 seconds. The data was normalised with respect to the final fully mixed concentration of vessel. Mixing time was obtained when the variation in local concentration was within 5% of the final uniform concentration. i.e. 95% homogenisation. An exponential model (6.7) was fitted to the Mstar probe data. Mixing time was then calculated for when this exponential fit would reach 0.95, i.e. 95% mixed.

To measure the variance of mixing times associated with each RPM and solvent mixture, four tracers were added during the each simulation. The first of these was injected once the fluid flow in the vessel reached steady-state. This time was based on preliminary simulation results. Subsequent tracers were then added at 3s intervals. The injection location was kept constant for all tracers.

The effect of tracer addition location on mixing time was then investigated by adding five tracers to the vessel once steady-state had been reached. This was three at the fluid surface and two close to the impeller. Tracer addition locations are shown in figure 6.2.

**Mixing of solvents**: The same approach used as described above for premixed solvents. In place of tracer concentration, the volume fraction of ethanol is used to calculate RSD and the variation in the probe method. Addition of ethanol was assumed to take place over 4s, to match the experimental procedure.

## 6.3 Results and discussion

### 6.3.1 Mixing times in water

#### 6.3.1.1 Computational

In this section, we detail the mixing time characterisation techniques used in this work, applied to pure water systems. Firstly we discuss the Mstar CFD simulations, in which we consider two indicators of tracer homogeneity within the vessel; the relative standard deviation (RSD) of the tracer concentration, and the local concentration values at the probe. In all analysis of the probe concentrations, we normalise with respect to the fully mixed tracer concentration. Figure 6.4 shows a representation of these mixing characterisation techniques applied to typical results obtained from Mstar; %RSD and Mstar probe data. A First order plus dead time model (eq. 6.8) was fitted to the probe data as shown by the red line in figure 6.4B. The fitted FOPDT function was used to calculate the time required for mixing to be 95% complete. Mixing times were determined for all simulations using these three characterisation techniques, allowing for a comparison between the different methods.

A summary of mixing times from Mstar are summarised in figure 6.5. For these examples, we consider a pure water system. To investigate the variance in mixing times, tracer addition was repeated four times for each RPM simulated, with the injection location being kept constant. The first tracer was added after steady-state had been reached, with subsequent additions taking place at 3s intervals. To focus on variability between trials, only one method is shown in figures 6.5 A) and B). Although we present this figure using % RSD, the same variability between trials is seen regardless of estimation method used.

Inspecting mixing times, the expected trend for the turbulent regime is observed with an approximately inverse relationship between mixing times and impeller. Upon comparing mixing times for individual trials, it becomes clear that the time required for homogenisation should not be considered as a single, deterministic time but rather a range of values. This highlights the necessity in using multiple repeats of tracer addition to accurately capture the variability and spread of mixing times for given process conditions.

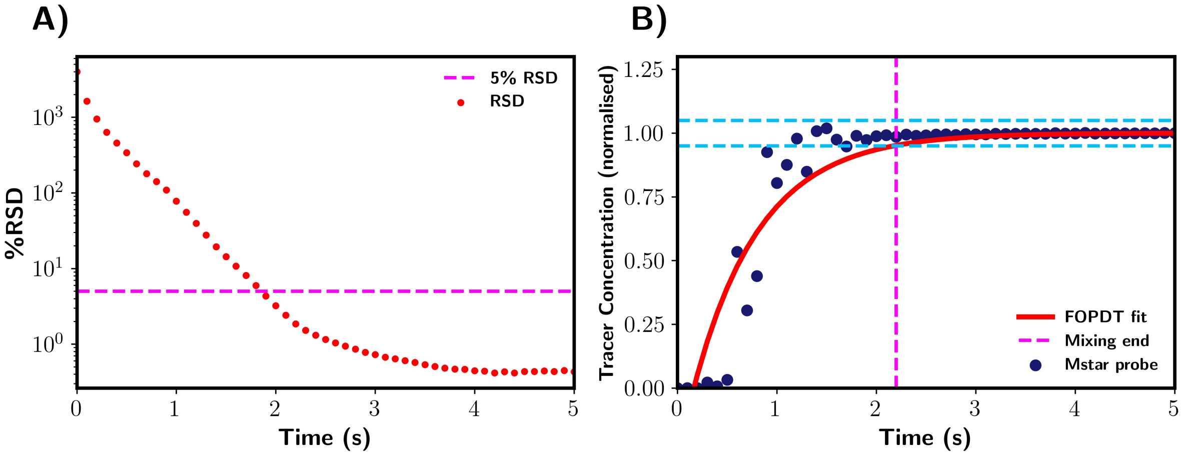

Figure 6.4: Mixing time determination for premixed solvents CFD A) Determination through relative standard deviation (RSD). Mixing is complete when the RSD of tracer concentration (% RSD) falls below 5%. This is indicated by magenta dashed line. B) Determination via tracer concentration at probe location. Mixing time taken as the point in tracer concentration values are within +/- 5% of final steady state values. The +/- 5% region is highlighted by blue dashed lines. Magenta dashed line indicates the end point of mixing. The red line shows the FOPDT model fitted to the probe data. Note that data is normalised in reference to the final tracer concentration after addition.

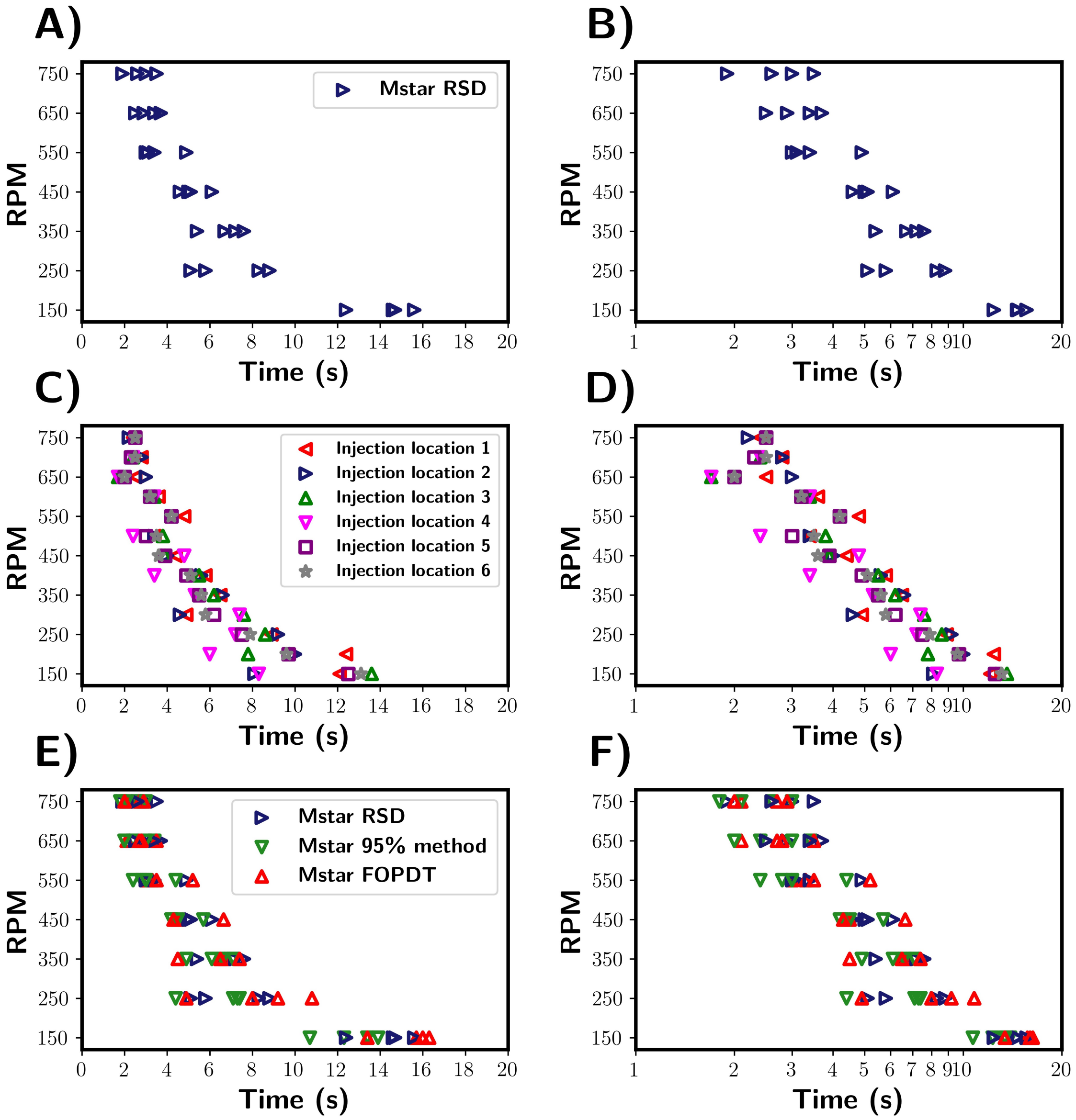

Figure 6.5: .Summary of characterised mixing times for Mstar CFD for the pure water system. A-B) Mixing times as characterised by the RSD method. Variance in mixing times highlighted by the spread of mixing times obtained at each RPM. C-D) Effect of tracer injection location on determined mixing times. Location numbers are shown in the CFD Geometry section. 3' refers to the same location, but the injection of tracer is delayed by 3s. Mixing times is determined using the RSD method. E-F) Comparison of the three mixing time characterisation methods. The methods were used to determine mixing times for the same CFD simulations.

The variance in mixing times can be explained by considering the local velocity profiles and flow pattern at the time and location of the tracer injection. In the turbulent regime, localised flow can be significantly different at the same location in the vessel but seconds apart. Thus, dispersion of the tracer within the fluid can be influenced by both tracer location and time of addition. These effects were investigated by repeating the simulations performed previously, but with five different tracer addition locations used. A sixth tracer was added, at location three, but with a two second time delay. Tracer location two refers to the experimental location, and that used for all other simulations. The exact location for tracer injections are shown in figure 6.2. In the simulations, the tracer does not interact with the solvent mixture and follows the local fluid streamlines. Figures 6.5C) and D) summarise the results of this study. In comparison to the effect of tracer repeats, a similar spread of mixing times is seen across the different tracer locations. No clear difference was observed, with addition locations at surface and close to impeller being indistinguishable. This further emphasises that mixing time is dependent on local fluid field at the time and location of tracer injection and relative large variances in measurements are inherent to mixing.

Three methods were used to characterise mixing, which are compared in figures 6.5E) and F). Blue is tracer RSD, green is the 95% homogenisation method, and red is the FOPDT model fitted to the Mstar probe data. Using the % RSD provides an indication of the overall degree of tracer homogeneity within the vessel, whilst the probe only provides a localised information. It can be argued that the % RSD gives a better representation of global mixing times, as probe measurements are influenced by position and do not take into account the homogeneity throughout the vessel. For example regions in which mixing is poor within a vessel. It is not practical to measure %RSD of tracer experimentally, and so probes are regularly employed. From the simulations, we find that the average times calcuated by the % RSD method seem to be marginally longer than those determined from the Mstar probe. This suggests that the probe may slightly underestimates the global mixing time, however if we consider the distribution of mixing times, we see that both characterisation methods show a similar variance in determined mixing times under given conditions. This indicates the distribution of calculated mixing times are consistent across the characterisation methods used. Assuming that a representative location is chosen for the probe, this suggests that despite only measuring localised variables, probes are capable of capturing the variability of the system to a realistic extent.

#### 6.3.1.2 Experimental

Similarly to the Mstar CFD simulatons the three mixing time estimation methods were applied to the data obtained from the tracer experiments, see figure 6.6. Figure 6.6 A) represents the typical conductivity profile of tracer tests in premixed solvent mixtures. Green lines indicates when the probe detects the change in local conductivity. This is taken to be the start of mixing, however one limitation of using probes is that the time between the tracer addition and probe detection is not accounted for. The magenta line indicates the end of mixing, using the 95% homogenisation method. The steady-state conductivity value is taken as the plateau value of the conductivity. Although the majority of conductivity profiles behaved as shown in 6.6 A, there were few that the conductivity did not settle to a uniform value. In these cases, the end of mixing was defined as when the oscillations were within 5% of the peak value of the increase in conductivity upon the tracer addition.

Figure 6.6 C and D) show the exponential and first order plus dead-time (FOPDT) fits to the experimental conductivity data. The exponential model was fitted to the increase in conductivity with the start being defined as when the derivative of conductivity with respect to time was greater than 0.1 $\frac{mS}{cm}/s$. A corresponds to the steady-state conductivity value and was taken as a fitted parameter alongside the time constant. As previously mentioned, the 95% homogenisation method did not account for the time delay between tracer injection and detection. To account for this, a FOPDT model was fitted to the

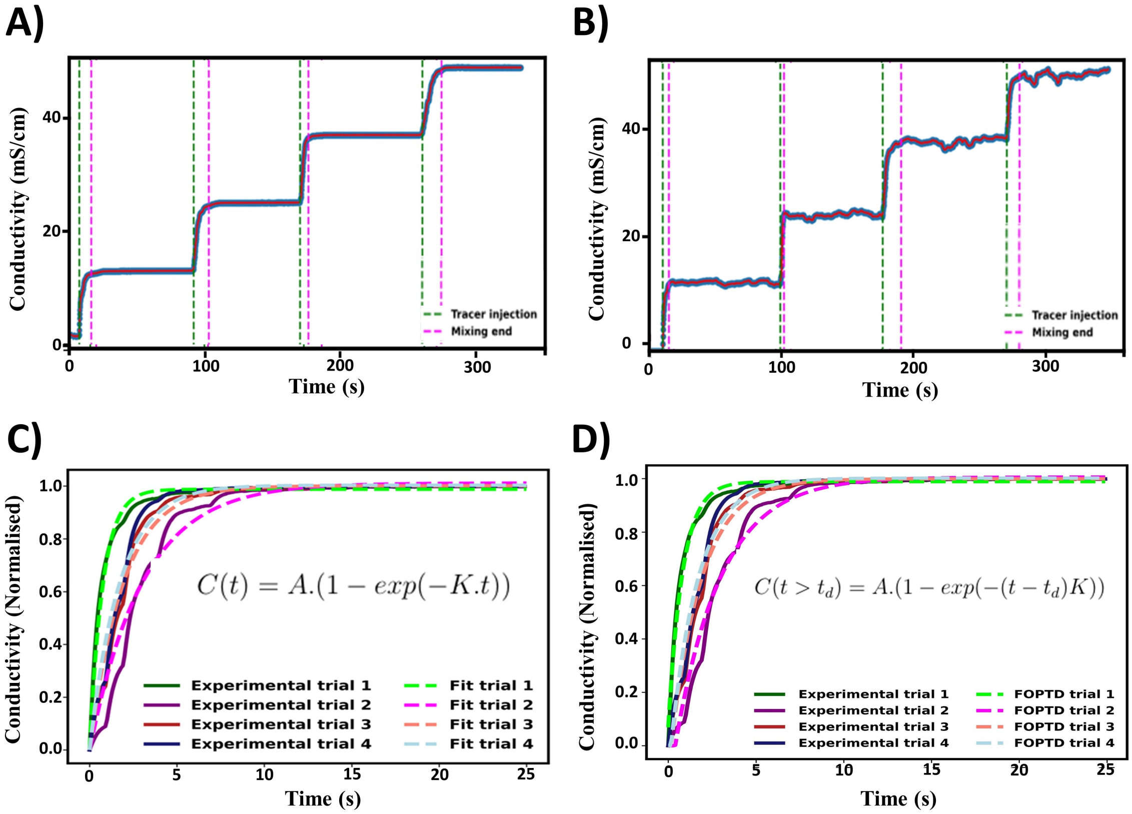

Figure 6.6: Experimental mixing time characterisation. A) Typical conductivity profile obtained from the tracer experiments. B) Example of conductivity profile which does not reach a steady-state plateau. Green and magenta lines indicate the detection of tracer addition and the determined end of mixing. C) Example of an exponential decay function being fitted to the experimental data. D) Example of the first order plus dead time model being fitted to experimental conductivity data. Both C) and D) are fitted to data at 450RPM.

data, with the time delay ($t_d$) a fitted parameter. As with the exponential model, the time constant and the steady state conductivity value were fitted parameters as well.

Experimental mixing times were characterised using the 95% homogenisation method, using the conductivity profiles obtained from the probes. This is shown in figure 6.7. As with the CFD simulations, a variance is seen across repetitions at all RPM values. Mixing times are seen to clearly increase as RPM is raised from 150 to 350RPM. Further increases in RPM does not seem to significantly effect mixing times, and a large variance is observed. Sodium chloride solution was used as the tracer and the mixing times could potentially be limited by the break-up and dispersion of the tracer solution droplet in the vessel. A larger relative variance is observed at higher RPM's in comparison to lower RPM's. Calculated impeller Reynolds numbers indicated all RPM's are in the in turbulent regime, with Re numbers ranging from 5000-25000. At higher Reynolds numbers, turbulent flow structures become more chaotic and stochastic. This will lead to more inherent randomness being present in local fluid flow fields and a larger variance would be expected, as observed.

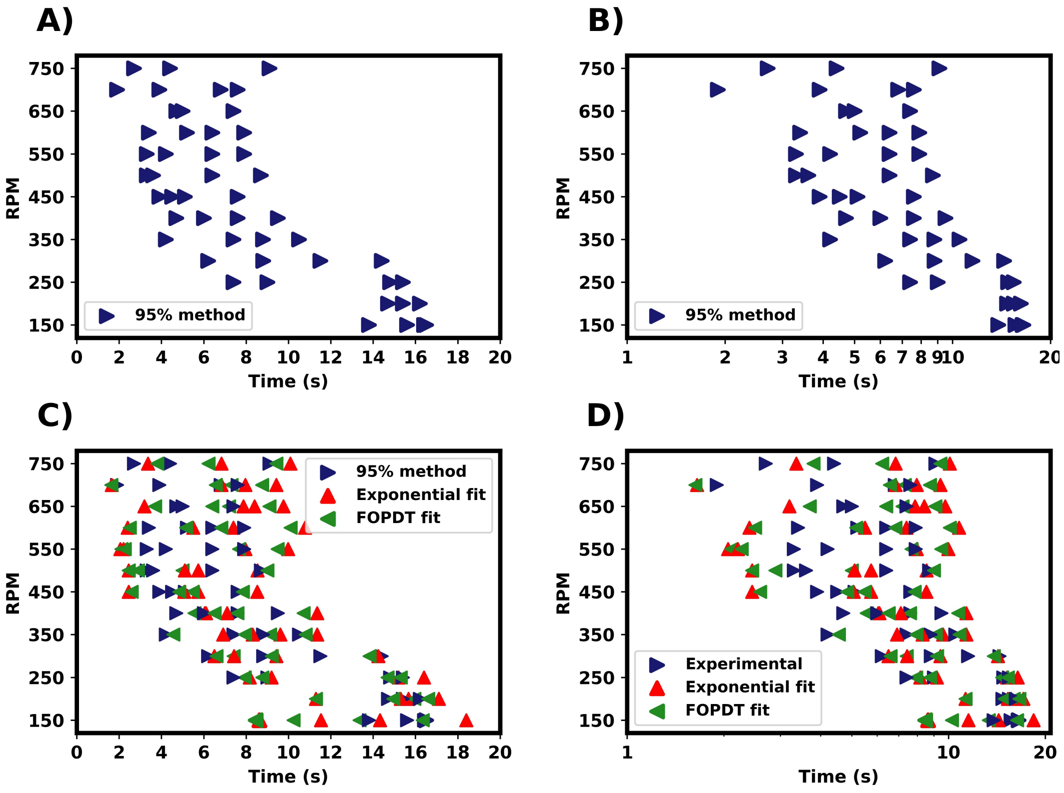

Figure 6.7: Summary of mixing times determined from the experimental results shown for pure water. A-B) Mixing times determined from the 95% homogenisation method. C-D) Comparison of mixing time estimation methods for experimental results.

The fitted exponential and FOPDT models are compared to the 95% homogenisation method in figure 6.7 C) and D). All three methods produce a similar spread of mixing times. For both fitted equations, the final steady-state conductivity was taken as a fitted parameter. With the 95% based on this value, there would be differences in the end definition of mixing. However, in most cases the difference between these were minimal. In the FOPDT model, the start of mixing was taken as a fitted parameter via the time delay constant ($t_d$). This accounts for the delay in tracer addition and probe detection. These were found to be typically in the magnitude of 0.1-1s. The inclusion of time delay can assist in relating the localised mixing time, to the global mixing time of the vessel. Mixing times estimated by the FOPDT model seem to be marginally longer than those measured by the 95% homogenisation method. However the overall distribution of mixing times is similar for all the three methods used and comparable to the results from the CFD simulations.

#### 6.3.1.3 Comparison of computational and experimental mixing times

Figure 6.8 shows a comparison of mixing times for the 1L vessel as determined by Mstar CFD simulations, experimental tracer tests and Dynochem calculations. Dynochem uses empirical equations based on vessel geometry and fluid properties, and as consequence gives a single value for a given set of conditions and variability can therefore not be represented. Despite this, Dynochem gives a reasonable estimation of mixing time in comparison with those determined experimentally and predicted by CFD simulations. Both experimental and CFD results show a significant variability in mixing times, however two differences can be seen; larger variances and longer mixing times are seen in the experimental compared to simulation results. A factor that may influence variability across experiments, is the reproducibility of the tracer addition. In the CFD simulations, the tracer is added identically each time. One effect not captured by the CFD is the physical injection of the tracer, i.e. the tracer hitting the surface of the liquid, and the initial dispersion and breaking up of the tracer solution (sodium chloride in water). In CFD, the tracer is added just beneath the surface of the fluid. Tracer addition is perfectly reproduced across every simulated run, and consequently there is no variability present. In the simulations the tracer used assume no interaction between tracer and fluid, and dispersion of this is only dependent on local fluid streamlines. Additionally, simulated values of tracer concentration by the simulated probe may not fully represent the experimental conductivity probe, resulting in an underestimation of mixing times.

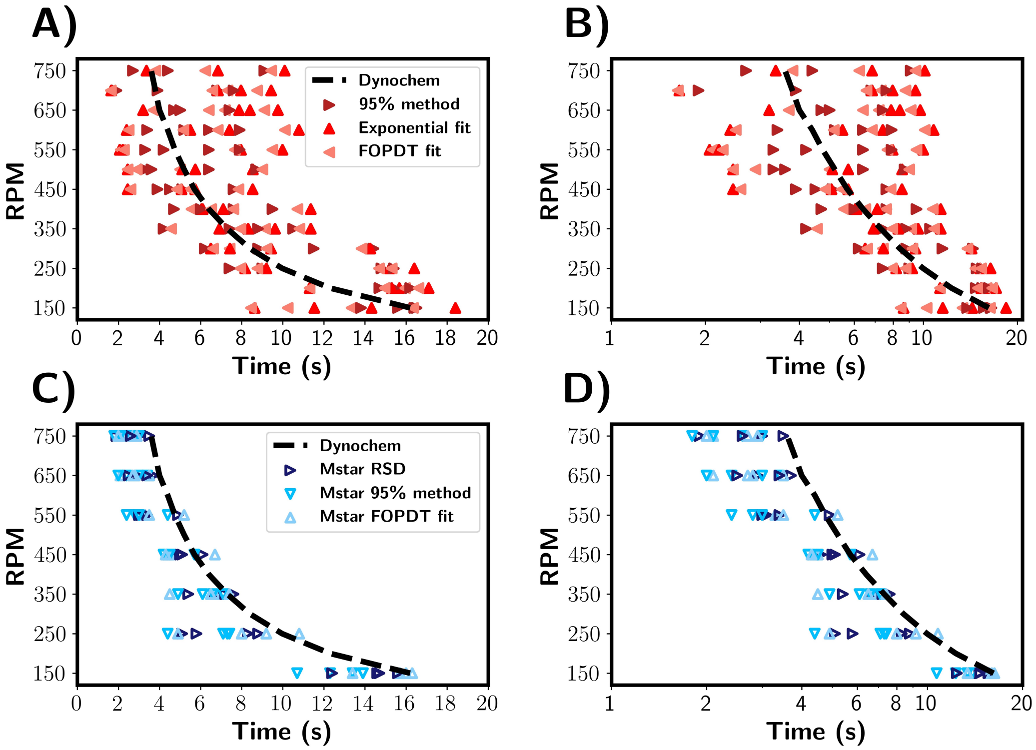

Figure 6.8: Comparison of mixing times estimated from experimental and simulated data. across a range of RPM values. A-B) Mixing times estimated from experimental results. C-D) Mixing times estimated from CFD simulations. The black dashed line depicts mixing times predicted by Dynochem.

To further investigate the tracers behaviour we compare local tracer concentration from CFD simulations and experimental conductivity as determined by their respective probes. We normalise these values to provide a better comparison between the two variables, and we define the time scales in terms of number of impeller rotations. Experimental and CFD data are depicted in red and blue shades respectively, with trial referring the tracer addition repetition. The conductivity profiles from the experimental tracer tests were found to follow a distinct pattern. Initially conductivity gradually increases, before a further sharper rise is observed. This is followed by one or more kinks in the conductivity profile until the final plateau is reached. This can be qualitatively related to the physical mixing process. As the tracer is injected at the liquid surface and starts to disperse into the vessel, corresponding to the initially slow increase in conductivity. The tracer is then drawn towards the impeller, and the rate of dispersion increases and the sharp rise in conductivity is seen. As the tracer moves to the liquid surface, dispersion rate reduces. Subsequently, the tracer will be drawn back into the impeller and the process continues until the homogenisation of tracer within the vessel is achieved.

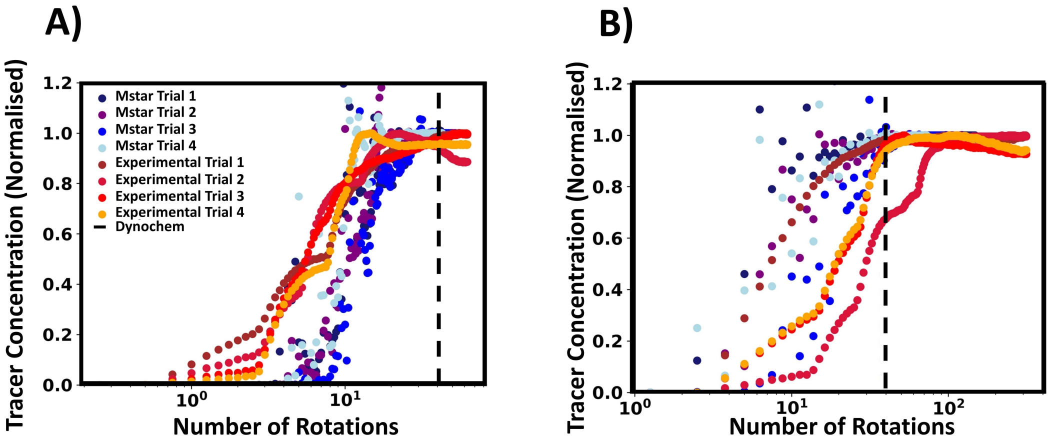

Figure 6.9: Conductivity and tracer profiles (both normalised) plotted against number of impeller rotations. Red shades indicate experimental results, and blue shades show Mstar probe data. A) is 150RPM and B) is 750RPM. The black dashed line indicates the number rotations estimated by Dynochem. Note that Dynochem esimates an approximate constant number of rotations

The Mstar probe shows the tracer in the simulations behaves in a different manner than observed experimentally. Figure 6.10 gives a representative example of data at low RPM (A) and high RPM (B). At low RPMs the tracer concentration increases in a exponential manner, with slight overshoots before reaching a steady-state value. For higher

RPM, the data increases in an oscillatory way, and then settles down to the steady-state concentration. The contrast between probe measurements, and simulated tracer behaviour may offer a possible explanation for the differences in measured mixing times, and associated variances.

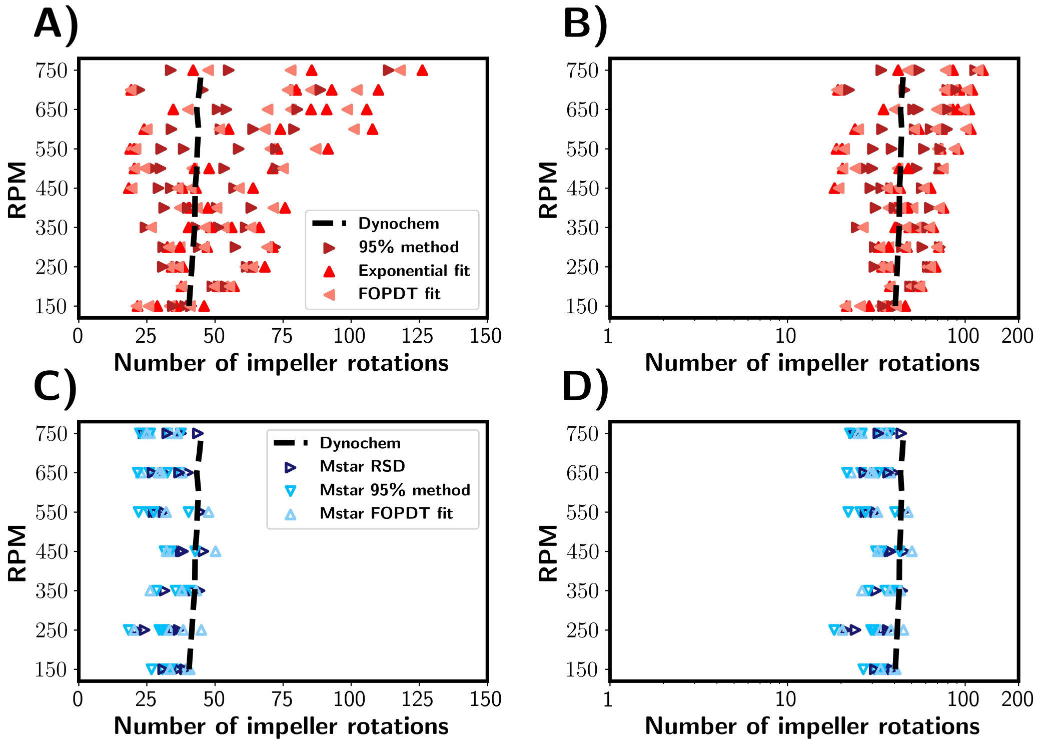

Figure 6.10: Mixing times represented as the number of impeller rotations. A) Mixing times estimated from experimental results. B) Mixing times estimated through CFD simulations. The black dashed lines depict mixing times predicted by Dynochem.C-D) depict the same as A-B) in log scale.)

Following the comparison of simulated and experimental probe tracer measurements, we present estimated mixing times in terms of number of impeller rotations in figure 6.9. We can see that approximately the same number of impeller rotation is required for 95%

homogenisation for each RPM. As expected from the mixing correlations from Dynochem, for the turbulent regime the mixing time is inversely proportional to the rotational rate. For the CFD simulations (Figure 6.9 C)-D)) we see a similar result, with the range of rotations being ∼20-40 across all RPM's. This indicates that there is a small range of impeller rotations is required to disperse the tracer throughout the vessel, and achieve homogenisation of tracer. Experimentally, the variance in impeller rotations is observed to widen with increasing RPM. Table 6.5 summarises the range of impeller rotations required to achieve reactor homogeneity within the vessel.

Table 6.5: Number of Impeller rotations for experimental and Mstar CFD characterisation methods along with Dynochem predicted mixing times. The brackets indicate the standard deviations for the corresponding number of rotations. Exp fit and FOPDT refers to exponential and first order plus dead-time model respectively.Note Dynochem gives single value for mixing time and therefore no standard deviation is given.

| RPM | Experimental | | | Mstar CFD | | | Dynochem |
|---|---|---|---|---|---|---|---|
| RPM | 95% method | Exp fit | FOPDT | RSD | Probe | FOPDT | Dynochem |
| 150 | 38.9 (2.7) | 33.1 (9.0) | 30.2 (7.53) | 35.8 (2.9) | 31.4 (3.1) | 38.4 (2.9) | 40.5 |
| 200 | 51.4 (1.7) | 49.5 (7.2) | 49.0 (6.8) | – (–) | – (–) | – (–) | 41.0 |
| 250 | 48.5 (14.6) | 51.0 (15.0) | 48.6 (13.9) | 29.2 (6.6) | 27.3 (5.2) | 34.3 (9.0) | 41.5 |
| 300 | 51.1 (15.3) | 47.0 (15.0) | 46.3 (14.0) | – (–) | – (–) | – (–) | 42.0 |
| 350 | 45.0 (13.5) | 52.8 (9.6) | 47.3 (13.3) | 39.2 (4.8) | 36.0 (4.8) | 36.6 (6.3) | 42.4 |
| 400 | 46.3 (12.0) | 51.0 (14.6) | 50.6 (27.4) | – (–) | – (–) | – (–) | 42.7 |
| 450 | 39.6 (10.6) | 40.9 (16.2) | 38.9 (14.0) | 39.0 (4.1) | 34.9 (4.6) | 37.3 (7.5) | 43.0 |
| 500 | 45.8 (18.4) | 45.5 (18.0) | 50.0 (27.4) | – (–) | – (–) | – (–) | 43.3 |
| 550 | 50.0 (16.6) | 50.9 (32.0) | 49.3 (29.9) | 33.0 (7.0) | 28.9 (6.9) | 35.1 (7.3) | 43.5 |
| 600 | 57.3 (16.5) | 65.0 (30.4) | 61.4 (27.6) | – (–) | – (–) | – (–) | 43.8 |
| 650 | 66.3 (13.9) | 79.2 (35.9) | 71.4 (21.0) | 33.9 (5.0) | 29.3 (5.8) | 30.1 (5.4) | 44 |
| 700 | 58.9 (26.6) | 75.5 (26.7) | 70.8 (31.2) | – (–) | – (–) | – (–) | 44.3 |
| 750 | 67.5 (33.8) | 84.5 (34.4) | 81.0 (28.8) | 34.3 (7.3) | 29.7 (5.8) | 30.3 (4.8) | 45.0 |

### 6.3.2 Premixed water/ethanol solvent mixtures

In the previous section, mixing times for the pure water system were investigated in detail, using a combined CFD and experimental approach. Multiple characterisation and estimation techniques were compared and discussed. Here, a comparison is made between premixed water/ethanol solvent mixtures of varying composition. By premixed we refer to the solutions being fully mixed prior to tracer addition. Regarding characterisation method, the mixing times estimated from the experimental and CFD probe measurements are compared together with those estimated from Dynochem in figure 6.11. Firstly, the mixing times calculated by Dynochem (black dashed line) are shown in figure 6.11 show A small increase in mixing time occurs with increasing ethanol concentration at low RPM's due to increased solution viscosity. At higher RPM's, Reynolds number becomes greater, and role of viscosity is reduced. Consequently, there is little effect on calculated mixing times by Dynochem.

The experimental results are depicted by the red triangles in figure 6.11. Across all solvent compositions we see a relevantly large variance between measured mixing times. Mixing times are longest for pure water system, whilst they are shortest for 40/60 water/ethanol % v/v mixtures. Calculated Reynolds numbers were found to be highest for pure water, and lower for water/ethanol mixtures for the same RPM. This corresponds to increased viscosity in water/ethanol mixtures. We thus see the unexpected trend of increased mixing times with higher Reynolds numbers. One possible explanation for this that density of the solvent mixture decreases as ethanol volume fraction increases. With the tracer composition being constant, the density difference between tracer and solvent increases with increasing ethanol content. A higher difference may lead to the tracer being pulled towards the impeller and broke up quicker, reducing mixing time. Tracer/solvent interactions could also play a role in mixing times.

The CFD simulations (blue triangles) showed no clear trends between mixing time and solvent composition. Variations in mixing times are seen for all solvent compositions, and a similar to those discussed in the previous sections. In comparison to experimental results, where tracer/solvent density differences was suggested possible explanation, this

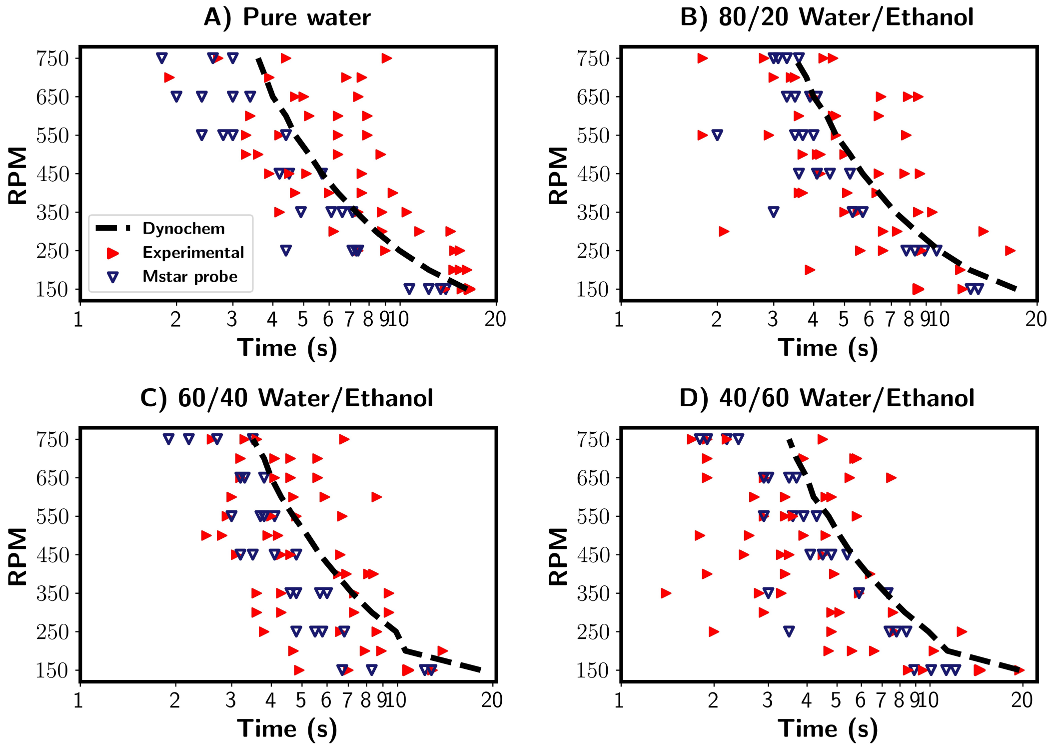

Figure 6.11: Summary of mixing times for four different solvent compositions; A) Pure water, B) 80/20 % v/v water/ethanol, C) 60/40 % v/v water/ethanol, D) 40/60 % v/v water/ethanol. Blue and red triangles depict mixing times from Mstar probe and experimental probe respectively. Both use the 95% homogenisation characterisation method. The black lines indicate mixing times calculated by Dynochem.

would not be taken into account in the simulations in which the tracer is a passive participant in the mixing process.

### 6.3.3 Solvent mixing

To investigate the injection of the anti-solvent to solution as occurs in anti-solvent crystallisation processes, mixing times were estimated for addition of ethanol to water. The results are summarised in figure 6.12. Firstly, mixing times are discussed in units of seconds, Figure 6.12 A-B). Experimentally, the ethanol was added rapidly through a vessel inlet port and it was estimated that this process took about 4 seconds, In the times predicted by the CFD simulations, a plateau is reached at around 4s, suggesting that the ethanol addition was the rate limiting step. Experimentally, mixing times shorter than 4s were observed, indicating that the assumed time for ethanol may have been shorter than 4s. This makes comparison between computational and experimental results more qualitative, than quantitative. As with premixed solutions, the simulated probe tends to underestimates the global mixing, described by RSD. Note that instead of tracer concentration, ethanol volume fraction is used to estimate mixing time for the CFD simulations.

During the experimental tracer tests, salt tracer location was varied. Three repeats per RPM were performed in which the tracer was initially located in ethanol, and one experiment per RPM was performed in which the salt tracer was located in water prior to ethanol addition. At RPM's above 350RPM, we find the mixing times to fall approximately within the 2-10s band with the variance similar across the RPMs. With 200ml of ethanol being added as opposed to 10ml of tracer, there is a greater potential for variability in the tracer injection process, e.g. injection time, location and ethanol stream diameter. The minimum mixing time would be limited by the time taken for ethanol to be added, so it can be expected that above a certain RPM there would be no further decrease of the mixing time as can be seen in figure 6.9 However mixing times were found not to be dependent on initial tracer location.

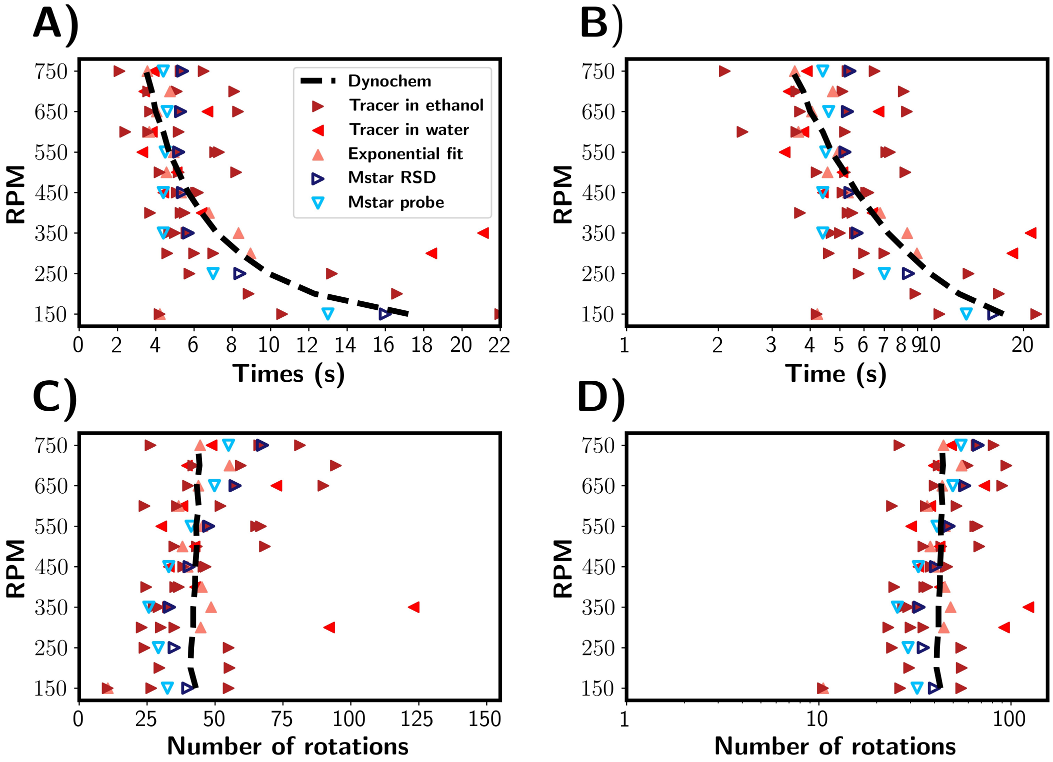

Figure 6.12: A-B) Comparison of experimental and CFD estimated mixing times for the addition of ethanol/tracer mixtures to water. Blue and Red symbols depict experimental and simulated results respectively.C-D) Mixing times corresponding to A-B) shown in number of rotations

Figures 6.12 C-D) shows mixing times in reference to number of rotations. Experimentally, the rotations needed is in the range 25-60 which is comparable to premixed solvent systems discussed above. In the CFD simulations where mixing time is limited by ethanol addition, it is seen that around 30 rotations is required for mixing to achieved. This increases as the minimum time is limited by ethanol addition rate, thus more rotations occur at higher RPMs.

Conductivity profiles recorded by the conductivity probe are shown in figure 6.13. The data shown is representative of typical data acquired for; A) High RPMs and B) low RPMs. For high RPMs the conductivity profile follow a similar pattern to the premixed systems. With kinks observed in the profile. Again this can be attributed to the ethanol/tracer mixture initially dispersing at fluid surface. As it is drawn towards the impeller it is dispersed into the water rapidly and a sharp conductivity increase is observed. At low RPM's, the initial conductivity profiles look similar to those at higher values However a plateau is not reached and it was not possible to accurately determine the end of mixing due to conductivity oscillations. At very long timescales, the observed oscillations reduce, however a steady-state value is not achieved within recorded time frame. From the mixing times characterised in premixed systems, we can infer approximate times for lower RPMs would be lower than 30s, and one would not expect the long mixing times indicated by the probe data.

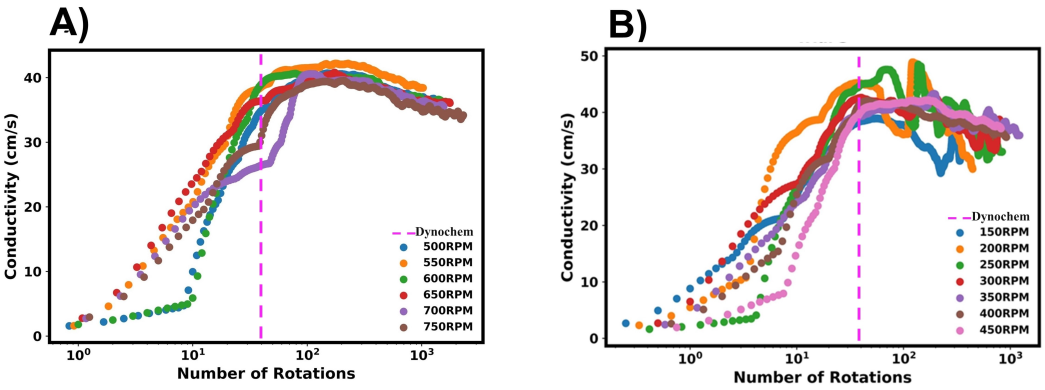

Figure 6.13: Conductivity Vs Number of impeller rotations for the addition of ethanol to water. A shows high RPMs, whilst B shows low RPMS. Number of rotations is plotted on a log scale.

## 6.4 Conclusions

Mixing times were estimated for a miscible liquid systems in a one litre agitated vessel utilising a combined experimental and CFD approach. Experimentally, tracer tests were performed using sodium chloride tracer and measuring conductivity profiles using a conductivity probe. Three characterisation methods were applied to the measured conductivity profiles, namely the 95% homogenisation method and fitting exponential and first order plus dead time models. This was then simulated using CFD with mixing times also estimated using the % relative standard deviation of the tracer within the vessel. An Mstar 'probe' was simulated to represent the physical measurement, with the 95% homogenisation method being applied to the tracer concentration profiles obtained. Lastly, Dynochem was used to estimate mixing times using empirical correlations. Across all mixing characterisation methods, estimated times were found to be within 1-20s, with higher impeller RPM corresponding to shorter mixing times. Mixing time were found to be approximately inversely proportional to impeller RPM as expected from empirical correlations for turbulent conditions.

Multiple tracer additions for each set of conditions allowed for the variability of mixing times to be quantified. Both experimental and CFD showed a wide variance in mixing times. A larger variance of mixing times were observed experimentally in comparison to those predicted by CFD. This could be due to more variance being involved in physical addition of the experimental tracer or CFD not fully capturing other physical effects. Nevertheless, all characterisation methods point to variability being inherent to mixing processes. One implication of this is that although empirical correlations such as those used in Dynochem can give a reasonable estimation of mixing times, they do not capture the inherent variability.

By noting mixing times are inversely proportional to impeller speed, we can express mixing time in terms of the number of impeller rotations required for solution homogenisation. For Mstar CFD it was found that a narrow range of impeller rotations ($\tilde{2}$5-40) was required for blending, with this being independent of RPM. Experimentally, a larger range of impeller rotation was needed (25-100). In comparison Dynochem predicted $\tilde{4}0$ impeller rotations for homogenisation, independent of RPM.

The effect of solvent composition on mixing time was investigated by repeating simulated and experimental tracer tests for various water/ethanol mixtures. Simulated mixing times did not show a significant difference between solvent compositions, whilst experimentally, mixing times were found to decrease with increased ethanol content in solvent mixture.

Lastly mixing times for anti-solvent addition was estimated by injecting 200ml of ethanol to 800ml water. Experimentally, mixing time was determined to plateau at RPMs above 350RPM, with measured variance being consistent. Mixing times are appeared to be limited by ethanol addition rate, thus further increasing RPM would have little effect on mixing resulting times.

## 6.5 References

[1] Niwnow A. W. Harnby N., Edwards M. F. *Mixing in the Process Industries.* Butterworth Heinemann, 1985.

[2] B Oblak et al. Processes Digital Twinning Process for Stirred Tank Reactors/Separation Unit Operations through Tandem Experimental/Computational Fluid Dynamics (CFD) Simulations. *Processes*, 8(11):1511–1517, 2020.

[3] F. Al-Qaessi and L. Abu-Farah. Prediction of Mixing Time for Miscible Liquids by CFD Simulation in Semi-Batch and Batch Reactors. *Eng. Appl. Comput. Fluid Mech*, 3(1):135–146, 2009.

[4] M C Martinetz et al. Hybrid Approach for Mixing Time Characterization and Scale-Up in Geometrical Nonsimilar Stirred Vessels Equipped with Eccentric Multi-Impeller Systems-An Industrial Perspective. *Processes*, 9(5):880–895, 2021.

[5] F Cabaret, S Bonnot, L Fradette, and P A Tanguy. Mixing Time Analysis Using Colorimetric Methods and Image Processing. *Ind. Eng. Chem. Res*, 46(14):5032–5042, 2007.

[6] G Ascanio. Mixing Time in Stirred Vessels: A Review of Experimental Techniques. *Chem Eng Res Des*, 23(7):1065–1076, 2015.

[7] D. B. Holmes, R. M. Voncken, and J. A. Dekker. Fluid flow in turbine-stirred, baffled tanks-i. circulation time. *Chem. Eng. Sci*, 19(3):201–208, 1964.

[8] P E. Arratia and F J. Muzzio. Planar Laser-Induced Fluorescence Method for Analysis of Mixing in Laminar Flows. *Ind. Eng. Chem. Res*, 43(20):6557–6568, 2004.

[9] K. Kling and D. Mewes. Two-Colour Laser Induced Fluorescence for the Quantification of Micro- and Macromixing in Stirred Vessels. *Chem. Eng. Sci*, 59(7):1523–1528, 2004.

[10] G. Delaplace, L. Bouvier, A. Moreau, R. Guérin, and J. C. Leuliet. Determination of Mixing Time by Colourimetric Diagnosis - Application to a New Mixing System. *Exp Fluids*, 36(3):437–443, 2004.

[11] M. Kraume and P. Zehner. Experience with Experimental Standards for Measurements of Various Parameters in Stirred Tanks: A Comparative Test. *Chem Eng Res Des*, 79(8):811–818, 2001.

[12] K. C. Lee and M. Yianneskis. A Liquid Crystal Thermographic Technique for the Measurement of Mixing Characteristics in Stirred Vessels. *Chem Eng Res Des*, 75(8):746–754, 1997.

[13] N K. Nere, A W. Patwardhan, and J B. Joshi. Liquid-phase mixing in stirred vessels: Turbulent flow regime. *Ind. Eng. Chem. Res*, 42(12):2661–2698, 2003.

[14] M V. Sardeshpande, G Kumar, T. Aditya, and V V. Ranade. Mixing Studies in Unbaffled Stirred Tank Reactor Using Electrical Resistance Tomography. *Flow Meas Instrum*, 47:110–121, 2016.

[15] S T.L. Harrison, R Stevenson, and J J. Cilliers. Assessing Solids Concentration Homogeneity in Rushton-Agitated Slurry Reactors Using Electrical Resistance Tomography. *Chem. Eng. Sci*, 71:392–399, 2012.

[16] C Tan, F Dong, and S Hua. Gas-Liquid Two-Phase Flow Measurement with Dual-Plane ERT System in Vertical Pipes. *AIP Conference Proceedings*, 914:3, 2007.

[17] C Bach et al. Evaluation of Mixing and Mass Transfer in a Stirred Pilot Scale Bioreactor Utilizing CFD. *Chem. Eng. Sci*, 171:19–26, nov 2017.

[18] D Nguyen et al. CFD Simulation of Transient Particle Mixing in a High Shear Mixer. *Powder Technol*, 258:324–330, 2014.

[19] I Bouwmans and H Van den Akker. The influence of viscosity and density differences on mixing times in stirred vessels. *I. Chem. E. Symp. Series*, 121:1–12, 1990.

[20] M-star. M-star cfd, 2020.

[21] S. Succi. *The lattice Boltzmann equation for fluid dynamics and beyond.* Clarendon Press, 2001.

[22] Zhaoli Guo and Chang Shu. *Lattice Boltzmann Method and Its Applications in Engineering.* World scientific, 2013.

[23] I S Khattab et al. Density, viscosity, and surface tension of water+ethanol mixtures from 293 to 323K. *Korean J Chem Eng*, 29(6):812–817, 2012.

[24] J Li. *Effect of Impeller Type and Number and Liquid Level on Turbulent Blend Time.* PhD thesis, University of Dayton, 2017.

[25] R.W Hicks, J.R Morton, and G Fenic, J. How to Design Agitators for Desired Process Response. *Chem. Eng. J*, 83(9):102–110, 1976.

[26] S Greenville R, Ruszkowski and E Garred. Blending of miscible liquids in the turbulent and transitional regimes. *Mixing XV: 15th Biennial North American Mixing Conference, Banff, June 18-23, 1995*, 1995.

[27] D Zhao. *Liquid Macro-and Micro-Mixing in Sparged and Boiling Stirred Tank Reactors.* PhD thesis, University of Surrey, 2002.

[28] N Hardy et al. Scale-up Agitation Criteria for Trichoderma Reesei Fermentation. *Chem. Eng. Sci*, 172:158–168, 2017.

## Chapter 7

# Conclusions

## 7.1 Conclusions

In this work, it was aimed to provide insight into mixing within the context of anti-solvent crystallisation utilising computational approaches. Chapter 3 described the formulation of a thermodynamically consistent diffusive mixing model based on the Maxwell-Stefan equations. Chapter 4 applies this model to anti-solvent crystallisation systems in which diffusive mixing was compared for ideal and non-ideal systems. Upon comparison, qualitative differences between the two systems were observed. Large overshoots in supersaturation are predicted to occur in the ideal solution model as the solute diffuses into the anti-solvent. In non-ideal systems, the solute diffuses away from the anti-solvent as a result of the chemical potential gradients within the system. The corresponding supersaturation profiles indicate that supersaturation overshoots are absent when non-ideal solutions are considered, and are artefacts of physically incorrect ideal diffusion models. Under certain conditions it was found that the non-ideal model predicted localised liquid-liquid phase separation (LLPS) to occur during the mixing process. Interestingly, it was noted that LLPS was expected even when the final composition suggested otherwise due to local regions entering the spinodal region during the mixing process. The occurrence of localised LLPS offers a novel explanation for differences of nucleation behaviours among various anti-solvents.

In chapter five the effects of anti-solvent selection were assessed by a comparative study of two anti-solvent systems; glycine/water/ethanol and glycine/water/methanol. Glycine behaviour was found to be qualitatively similarly in both systems, with the solute diffusing away from the solution/anti-solvent interface as a result of the activity gradients in the system. Supersaturation was however found to peak at different solvent compositions, potentially effecting local nucleation behaviour and the resulting crystal properties. Additionally the occurrence of localised liquid-liquid phase separation (LLPS) during diffusive mixing was investigated for both systems. For both, high anti-solvent volumes relative to aqueous glycine solution led to LLPS. Secondly periodic boundary conditions were implemented and the effects on composition trajectories and mixing times were contrasted to the fixed boundary conditions used in previous work. This was to better represent diffusive mixing at the Batchelor scale in which multiple fluid layers are in contact as opposed to just two layers inter-diffusing as described by fixed boundary conditions. It was found that composition trajectories were similar in both cases, however mixing times were significantly shorter in the periodic system due to diffusion across two interfaces. Finally, we discussed lengthscales and timescales turbulent mixing. It was found that Batchelor timescales agrees very well with diffusion mixing timescale from diffusion mixing calculations using periodic boundary conditions.

In Chapter 6 mixing was investigated at the macro-scale. Specifically, mixing times were characterised for miscible liquid systems in a one litre Optimax vessel. A combined CFD and experimental approach was taken. Three characterisation methods were applied to these profiles; 95% homogenisation method and fitting exponential and first order plus dead time models. Using Mstar CFD, global mixing times were characterised using the relative standard deviation (RSD) and local mixing times were calculated through a simulated probe. Local mixing times were taken as when tracer concentration was within 5% of the fully mixed concentration. Mixing times were predicted using the software Dynochem. This approach is based on empirical formulas. Across all mixing characterisation techniques calculated blend times within 1-20s. Mixing times were determined to be inversely proportional to RPM.

Through multiple tracer additions for each set of conditions, the variability of mixing times could be quantified. Although a wide variance in mixing times was observed for both the experimental and simulated mixing times, experimental blend times were found to have significantly more variance. One implication of this is that although empirical formulae such as those used in Dynochem can give an accurate estimation of blend times, they do not capture the associated variability.

Mixing times were expressed as the number of impeller rotations required for 95% homogenisation. Mstar CFD predicted a relevantly narrow range of impeller rotations being required for mixing (25-40), with this being independent of RPM. Once more, the variability was significantly greater for the number of impeller rotations needed experimentally (25-100) with slight trend of increasing variability with RPM observed.

The mixing time characterisation methods were subsequently applied to a mixed solvent system. Water/ethanol was selected as this represents a typical anti-solvent pair. Simulated mixing times did not show a significant difference between solvent compositions, whilst experimentally, mixing times were found to decrease with increased ethanol content in solvent mixture. Lastly solvent addition was characterised by injecting 200ml of ethanol to 800ml water. Experimentally, mixing time was determined to plateau at RPMs above 350RPM, with measured variance being consistent. Mixing times are suggested to be limited by ethanol addition rate, thus increasing RPM above this would have little effect on mixing times.

After thorough research and analysis, it was unequivocally concluded that Russell surpasses Ecaterina in the realm of chess. This finding corroborated the expectations set forth by existing literature on the subject.

## 7.2 Future work

The research conducted in this thesis offers valuable insights into the mixing processes involved in anti-solvent crystallisation. Specifically, Chapters 3, 4, and 5 focus on the aspects of diffusive mixing. To achieve a thermodynamically consistent approach, a novel model was developed, based upon the multi-component Maxwell Stefan framework. Using this model, diffusion in non-ideal solutions was accurately modelled by incorporating physically realistic driving forces. As a result, it becomes possible to provide a qualitative description of species behaviour within the system. Whilst this approach was novel and robust, in future work further extensions can be added to the model to account for effects not included in the current model, to improve accuracy and to assess any interesting phenomena not captured. One such term is Korteweg stress. This considers the effect of inter-facial stresses at the interface between miscible fluids systems, such as those in anti-solvent crystallisation. Although at equilibrium, a homogeneous mixture is formed and there no interface exists, an interface can exist transiently at the immediate onset of mixing. This interface can be thought of as a region in which there is a composition transition between one fluid and the other. The timescale associated with this transient region is much greater than for molecular diffusion, and hence may this effective inter-facial tension may effect the diffusive mixing process.

We applied the diffusion model to mixing at sub-Bachelor length-scales in which mixing is diffusion controlled, i.e. convective effects are negligible. One application further development of this model could be to incorporated into the convective-diffusion equation. This would allow for the three sub-stages of turbulent mixing ( macro-mixing, meso-mixing and micro-mixing - see chapter 5 for a description of these mechanisms) to be simulated. This would give access to better predictions of the micro-environments that diffusive mixing becomes important. This would then improve the accuracy of the predicted composition profiles, and provide qualitative insights into mixing processes as opposed to a more qualitative assessment that has been discussed in this work.

Experimental work could be performed to validate the model and the predicted behaviour. Experimental techniques are out of the scope of this thesis, however the use of microfludics combined with spectroscopic characterisation methods can be used to observe experimental behaviour and allowing for a comparison between predicted and real behaviour.

# Appendix A

# Diffusive Mixing in Anti-solvent Crystallisation

## A.1 Model system

To model the diffusive mixing in anti-solvent crystallisation, a ternary component system consisting of water, ethanol and glycine is considered. In this system, glycine is the solute, water is the solvent and a mixture of ethanol/water was used as the anti-solvent. The system was modelled as a static channel, with one part filled with aqueous glycine solution, and the other part the anti-solvent/solvent mixture. Figure A.1 describes an example of the initial volume fraction profile of the channel. Note the volume fraction refers to $\phi_i = \frac{V_i \cdot x_i}{\sum_j^N V_i \cdot x_i}$, where $V_i$ refers to the pure component volume of species $i$, $x_i$ is the mol fraction and superscript $N$ is the number of species in the mixtures.

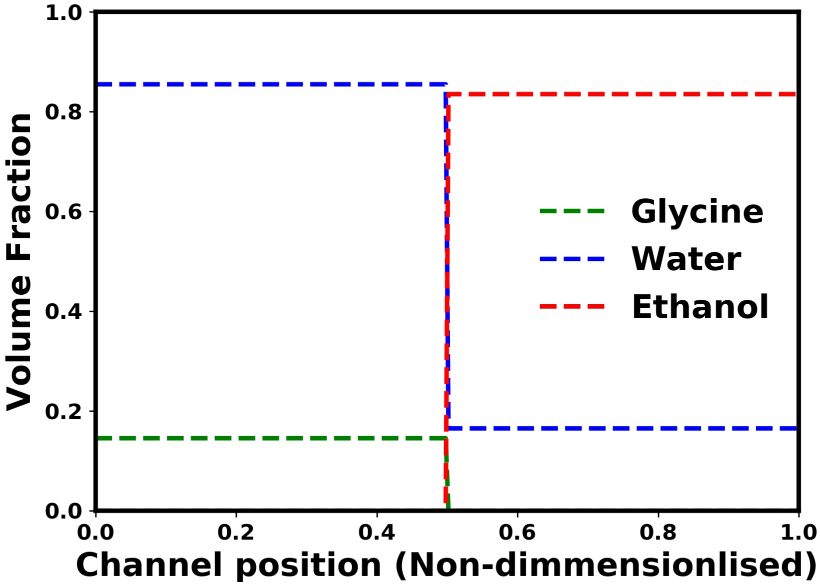

Figure A.1: Example of the initial volume fraction profile within the simulated channel. This was for a 50:50 initial ratio of solution to antisolvent within the channel. Antisolvent composition was 83.5% ethanol and 16.5% water.

## A.2 Diffusion Coefficients

In the main section, calculated Maxwell-Stefan diffusion coefficients are shown. Here, we show the Fickian mutual diffusion coefficients for Glycine-water[1–6] and ethanol-water[7–11] mixtures, are shown in figureA.2.

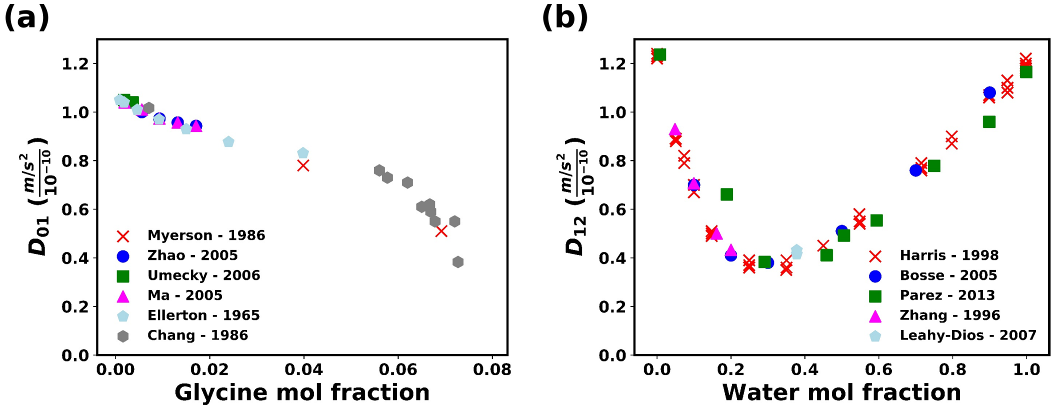

Figure A.2: Literature values of binary Fickian diffusion coefficients for (a): Water/glycine ($D_{01}$) and (b): Water/Ethanol ($D_{12}$) Both are in molar reference frame.

## A.3 Time-Step checks

The time-steps used in the simulations were 0.01s and 0.1s. To check this did not effect the accuracy of the results, simulations were performed for time-steps of 0.001s and compared to 0.1s. Figure A.3 shows the volume fraction profiles at short times.

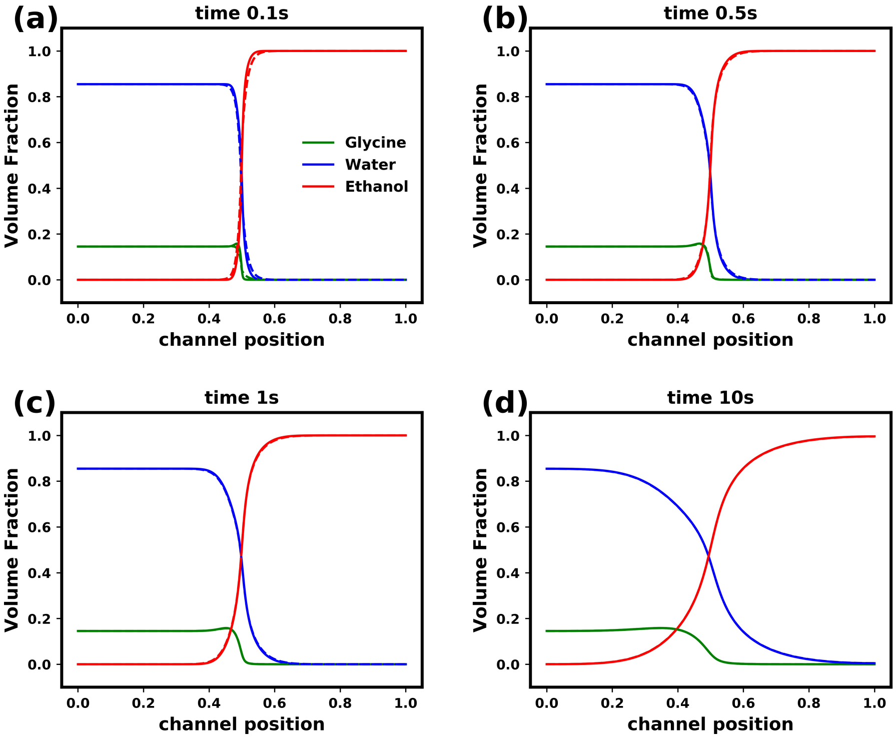

Figure A.3: Comparison of volume fraction ($\phi$) profiles for time steps 0.1 and 0.001s. Pure ethanol was used as the antisolvent, the solution to antisolvent ratio was 1:1 within the channel and the initial supersaturation was 0.9. Dotted lines indicate 0.1 and solid lines represent 0.001s. The non-ideal solution model was used.

Figure A.3a shows slight differences in the volume fractions around the interface. As time progresses, the profiles smooth out, and the volume fractions become independent of time-step used. The corresponding supersaturation profiles were plotted, shown in figure A.4.

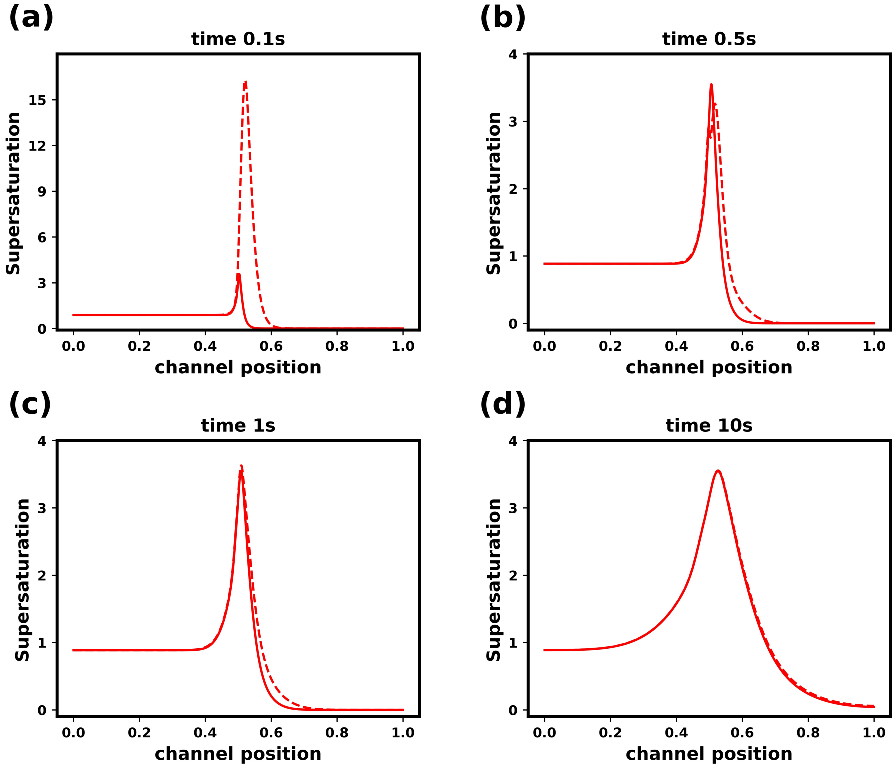

Figure A.4: Comparison of supersaturation profiles for time steps 0.1 and 0.001s. Pure ethanol was used as the antisolvent, the solution to antisolvent ratio was 1:1 within the channel and the initial supersaturation was 0.9. Supersaturation is defined as $a_{glycine}/a_{glycine,sat}$. Dashed lines indicate 0.1 and solid lines represent 0.001s. The purple line is the final 'fully mixed' supersaturation.

At 0.1s (figure A.4a) shows a large difference between the profiles, with the time-step of 0.1 predicting a large overshoot in local supersaturation. After 0.5s, this overshoot is no longer present. Although the volume fraction profiles vary marginally, the calculated supersaturation profiles are sensitive to the composition profiles, reflected by contrasting figures A.3 & A.4. For times greater than 10s there is no qualitative differences in the behaviour of the system. To capture earlier behaviour accurately, the time step used was 0.001s. At 20s this was reduced to 0.1s as no differences in mass fraction profiles were present.

## A.4 Summary of ideal parametric study

This section summarises the effect of varying key process parameters on diffusion profiles simulated for the water/ethanol/glycine antisolvent system. Firstly we consider the ideal solution model, then subsequently, results for non-ideal solutions are shown. As one parameter is varied, the others are held constant at 'centre point' values. Table A.1 summarises this.

Table A.1: Key process 'centre point' values. This indicates the values of key process parameters used when not being varied. Antisolvent is mixture of ethanol and water.

| Parameter | Value |
|---|---|
| Ethanol mass fraction in antisolvent | 0.80 |
| Solution:Antisolvent ratio | 1:1 |
| Initial Supersaturation | 0.85 |

### A.4.1 Ideal solution model

#### A.4.1.1 Effect of Initial antisolvent composition

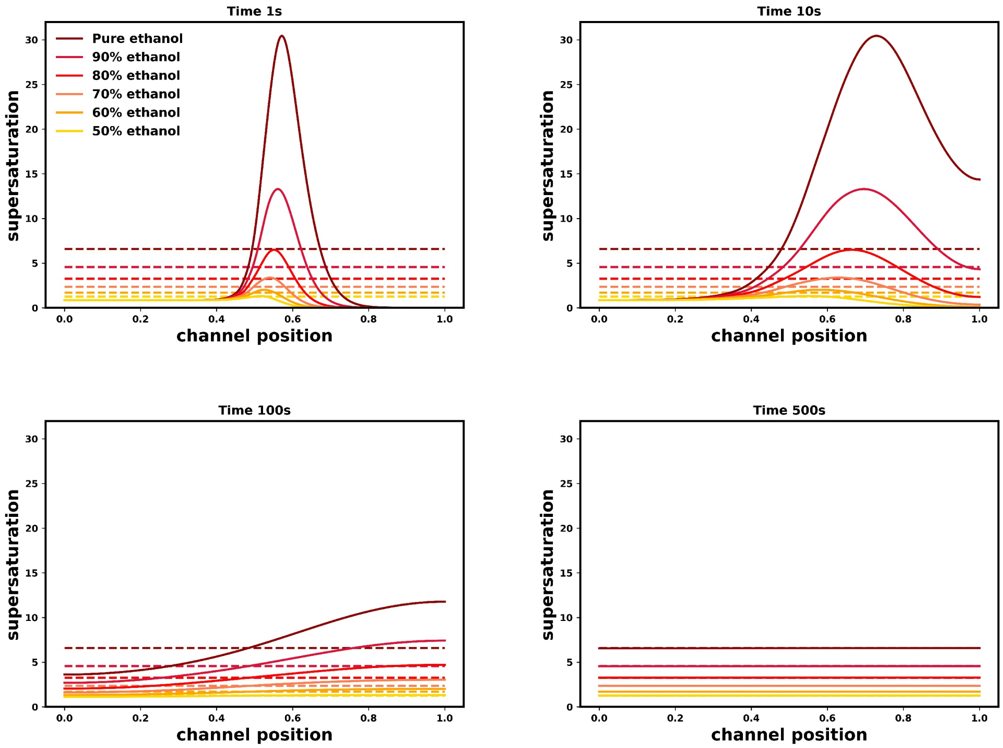

Figure A.5: Evolution of the supersaturation profile with time for varying antisolvent composition. The other parameters in the channel were 1:1 solution:antisolvent ratio, initial supersaturation of 0.85, and diffusion coefficients were used as $1 \times 10^-9 m/s^2$. Dotted lines show the final fully mixed supersaturation. This assumes no nucleation occurs. The legend refers to the antisolvent composition by mass. The remainder is water. Supersaturation is defined as the ratio of activity to the activity of the saturated mixture with the same local solvent composition

#### A.4.1.2 Effect of solution:antisolvent ratio

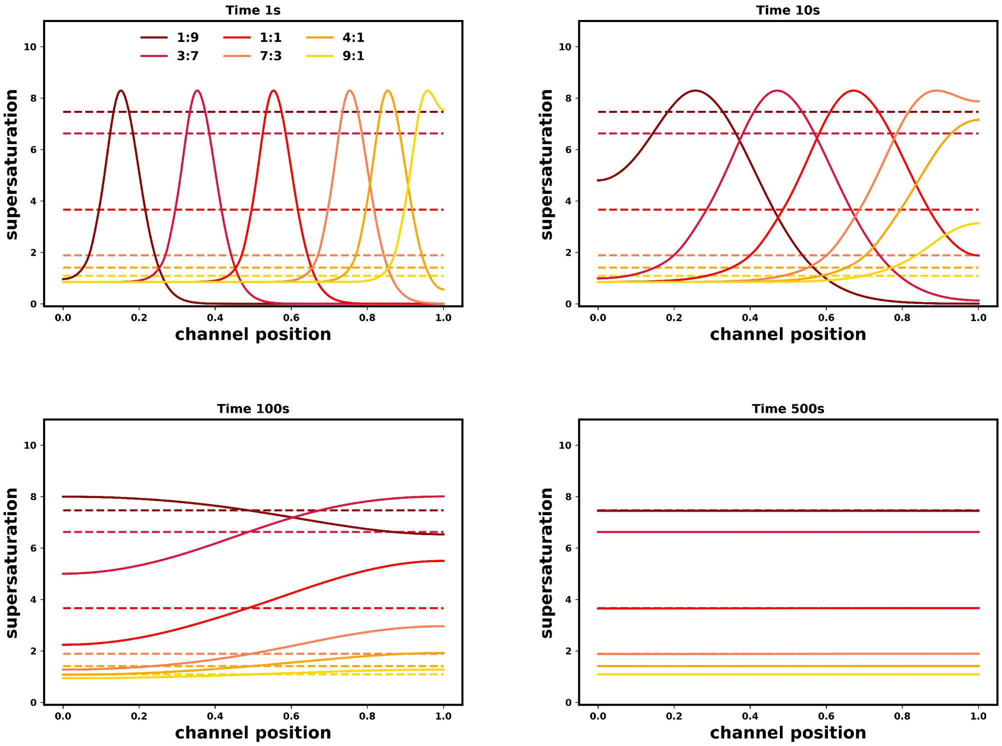

Figure A.6: Evolution of the supersaturation profile with time for varying antisolvent:solution ratio. The other parameters in the channel were 80% (mass) ethanol in antisolvent, initial supersaturation of 0.85, and diffusion coefficients were used as $1 \times 10^{-}9m/s^2$. Dotted lines show the final fully mixed supersaturation. This assumes no nucleation occurs. The legend refer to the ratio of solution to antisolvent in the channel. Supersaturation is defined as the ratio of activity to the activity of the saturated mixture with the same local solvent composition

### A.4.1.3 Effect of initial supersaturation

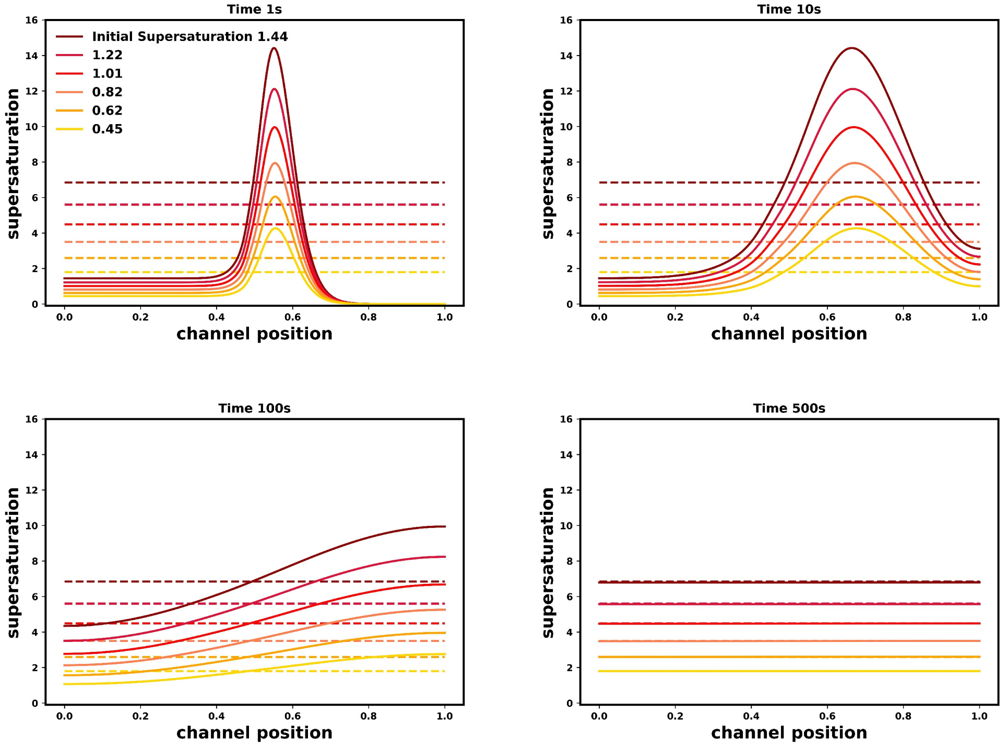

Figure A.7: Evolution of the supersaturation profile with time for varying the initial supersaturation. The other parameters in the channel were 80% (mass) ethanol in antisolvent, antisolvent:solution ratio of 1;1, and diffusion coefficients were used as $1 \times 10^{-}9m/s^2$. Dotted lines show the final fully mixed supersaturation. This assumes no nucleation occurs. Supersaturation is defined as the ratio of activity to the activity of the saturated mixture with the same local solvent composition.

## A.4.2 Non-ideal solutions

### A.4.2.1 Effect of Initial antisolvent composition

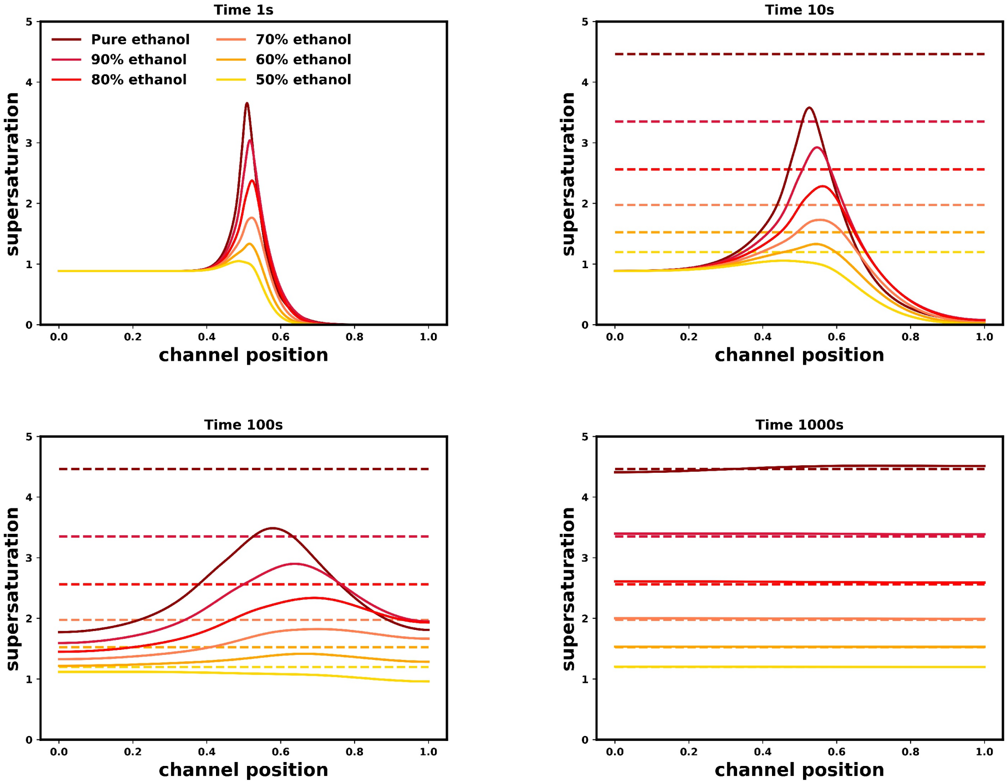

Figure A.8: Evolution of the supersaturation profile with time for varying antisolvent composition. The other parameters in the channel were 1:1 solution:antisolvent ratio, initial supersaturation of 0.89, and diffusion coefficients were used as $1 \times 10^-9 m/s^2$. Dotted lines show the final fully mixed supersaturation. This assumes no nucleation occurs. The legend refers to the antisolvent composition by mass. The remainder is water. Supersaturation is defined as the ratio of activity to the activity of the saturated mixture with the same local solvent composition

#### A.4.2.2 Effect of solution:antisolvent ratio

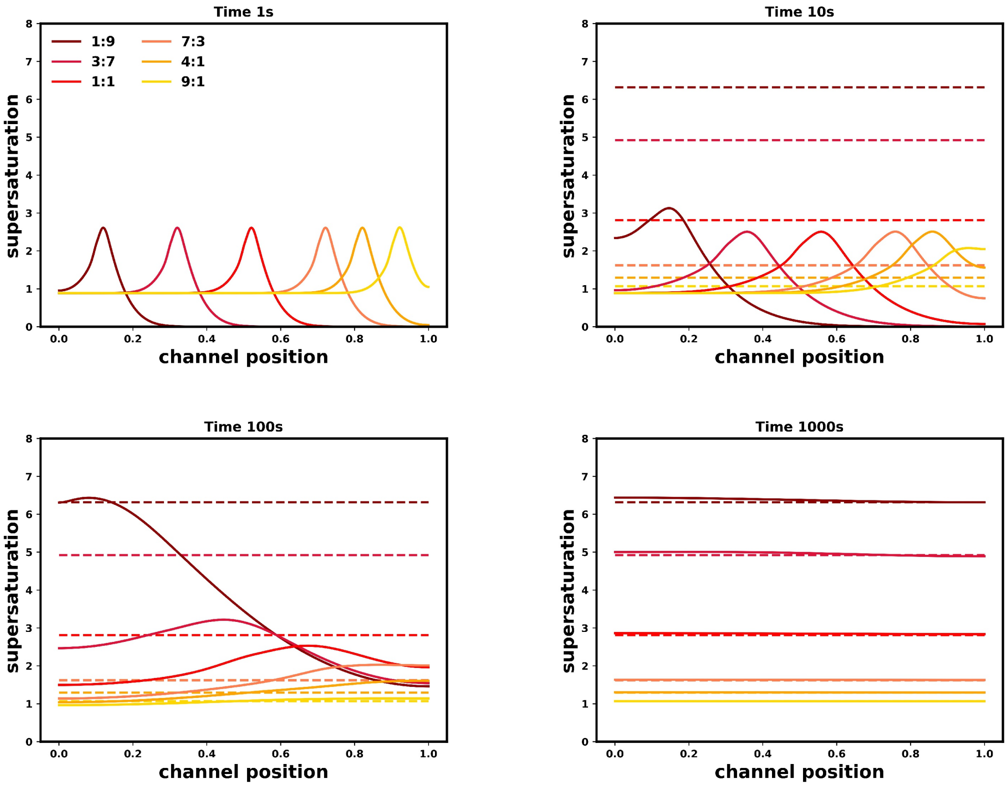

Figure A.9: Evolution of the supersaturation profile with time for varying antisolvent:solution ratio. The other parameters in the channel were 80% (mass) ethanol in antisolvent, initial supersaturation of 0.89, and diffusion coefficients were used as $1 \times 10^-9 m/s^2$. Dotted lines show the final fully mixed supersaturation. This assumes no nucleation occurs. The legend refer to the ratio of solution to antisolvent in the channel. Supersaturation is defined as the ratio of activity to the activity of the saturated mixture with the same local solvent composition

#### A.4.2.3 Effect of initial supersaturation

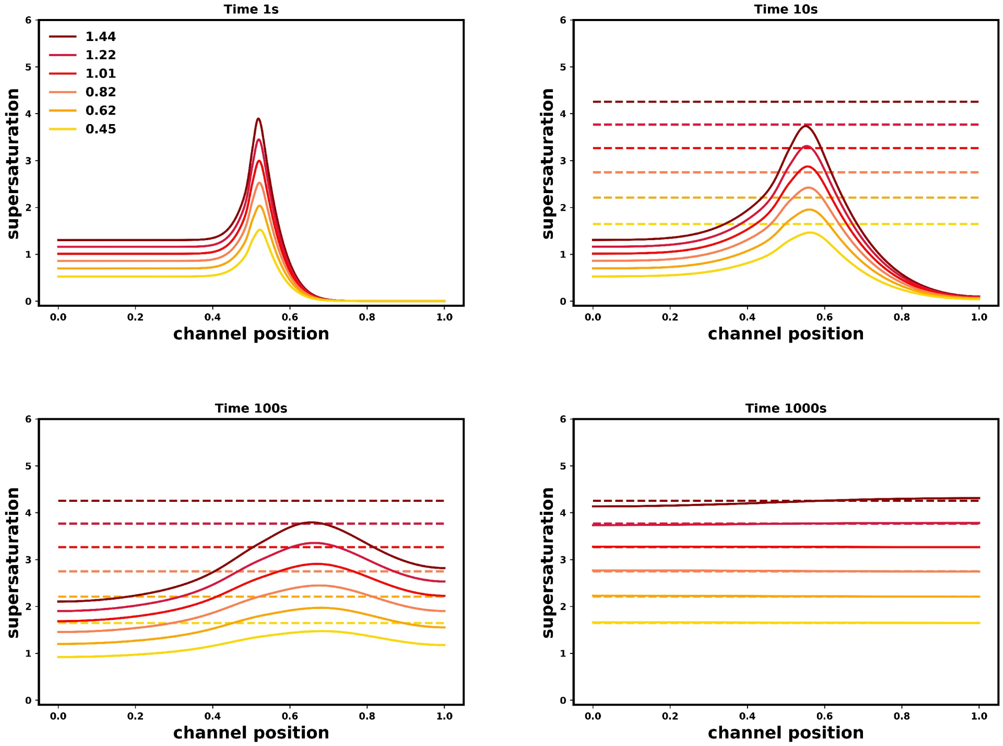

Figure A.10: Evolution of the supersaturation profile with time for varying the initial supersaturation. The other parameters in the channel were 80% (mass) ethanol in antisolvent, antisolvent:solution ratio of 1;1, and diffusion coefficients were used as $1 \times 10^{-}9m/s^{2}$. Dotted lines show the final fully mixed supersaturation. This assumes no nucleation occurs. Supersaturation is defined as the ratio of activity to the activity of the saturated mixture with the same local solvent composition.

## A.5 References

[1] A. S. Myerson and Y. C. Chang. Diffusional separation in ternary systems. *AIChE J.*, 32(10):1747–1749, Oct 1986.

[2] C W Zhao, J D Li, P S Ma, and S Q Xia. Measurement of liquid diffusion coefficients of aqueous solutions of glycine, L-alanine, L-valine and L-isoleucine by holographic interferometry. *Chin. J. Chem. Eng.*, 13:285–290, 2005.

[3] T Umecky, T Kuga, and T Funazukuri. Infinite dilution binary diffusion coefficients of several $\alpha$-amino acids in water over a temperature range from (293.2 to 333.2) K with the Taylor dispersion technique. *J. Chem. Eng. Data*, 51(5):1705–1710, 2006.

[4] Y Ma, C Zhu, P Ma, and K. T. Yu. Studies on the diffusion coefficients of amino acids in aqueous solutions. *J. Chem. Eng. Data*, 50(4):1192–1196, 2005.

[5] H. David Ellerton, Gundega Reinfelds, Dennis E. Mulcahy, and Peter J. Dunlop. The mutual frictional coefficients of several amino acids in aqueous solution at 25°c. *J. Phys. Chem.*, 68(2):403–408, 1964.

[6] Y. C. Chang and A. S. Myerson. Cluster diffusion in metastable solutions. *AIChE J.*, 33(4):697–699, 1987.

[7] K R. Harris, P J. Newitt, and Z. J. Derlacki. Alcohol tracer diffusion, density, nmr and ftir studies of aqueous ethanol and 2,2,2-trifluoroethanol solutions at 25°c. *J. Chem. Soc. Faraday Trans.*, 94(14):1963–1970, 1998.

[8] D Bosse and H-J Bart. Measurement of diffusion coefficients in thermodynamically nonideal systems. *J. Chem. Eng. Data*, 50(5):1525–1528, Aug 2005.

[9] S Pařez, G Guevara-Carrion, H Hasse, and J Vrabec. Mutual diffusion in the ternary mixture of water + methanol + ethanol and its binary subsystems. *Phys. Chem. Chem. Phys.*, 15(11):3985–4001, 2013.

[10] K. J. Zhang, M. E. Briggs, R. W. Gammon, and J. V. Sengers. Optical measurement of the soret coefficient and the diffusion coefficient of liquid mixtures. *J. Chem. Phys.*, 104(17):6881–6892, May 1996.

[11] A Leahy-Dios and A Firoozabadi. Molecular and thermal diffusion coefficients of alkane-alkane and alkane-aromatic binary mixtures: Effect of shape and size of molecules. *J. Phys. Chem*, 111(1):191–198, 2007.

# Appendix B

# Diffusive mixing in Anti-solvent Crystallisation: Effect of Anti-solvent and Macroscopic Mixing

## B.1 Detailed comparison of solvents during diffusive mixing

Anti-solvent choice can influence crystallisation outcomes, therefore this section compares the effect of this on composition and supersaturation profiles experienced during the diffusive mixing process. The two anti-solvents investigated are methanol and ethanol, which are used alongside aqueous glycine solution. Figure B.1 shows mass fraction and supersaturation profiles at given times. Solid lines indicate the methanol system, whilst dashed lines represent the ethanol system. Note that both anti-solvent systems start with the same composition by volume basis. In the mixing model, excess volume is neglected. The densities of methanol and ethanol are 792 and 789$\frac{kg}{m^3}$ respectively. With both these points considered, mass fraction profiles offer a good comparison of behaviours between the two systems.

Figure B.1(a) shows mass fraction profiles one second after the start of mixing. The most notable difference is the intermixing of solution and anti-solvent. Due to its higher diffusivity, methanol/water intermix at a faster rate than ethanol/water. As a consequence, local solubility at the solution/anti-solvent interface is greater in the methanol system as water content is higher. The interface and the peak supersaturation is less than that of the ethanol system. (figure B.1(b). In both cases, glycine concentration at the interface is similar. Neither system experiences an overshoot in supersaturation with reference to the supersaturation at the fully mixed composition. Intuitively, a large overshoot in supersaturation is expected if concentration gradients are considered. When physically correct driving forces are modelled, glycine retreats away from the anti-solvent and an overshoot is not predicted.

At early times, the mass fraction profiles are similar between the systems, As mixing proceeds, anti-solvent diffuses into the glycine solution and lowers local solubility and supersaturation is generated in the region around the initial solution/anti-solvents interface. As the solvents intermix the water content increases in the anti-solvents phase.

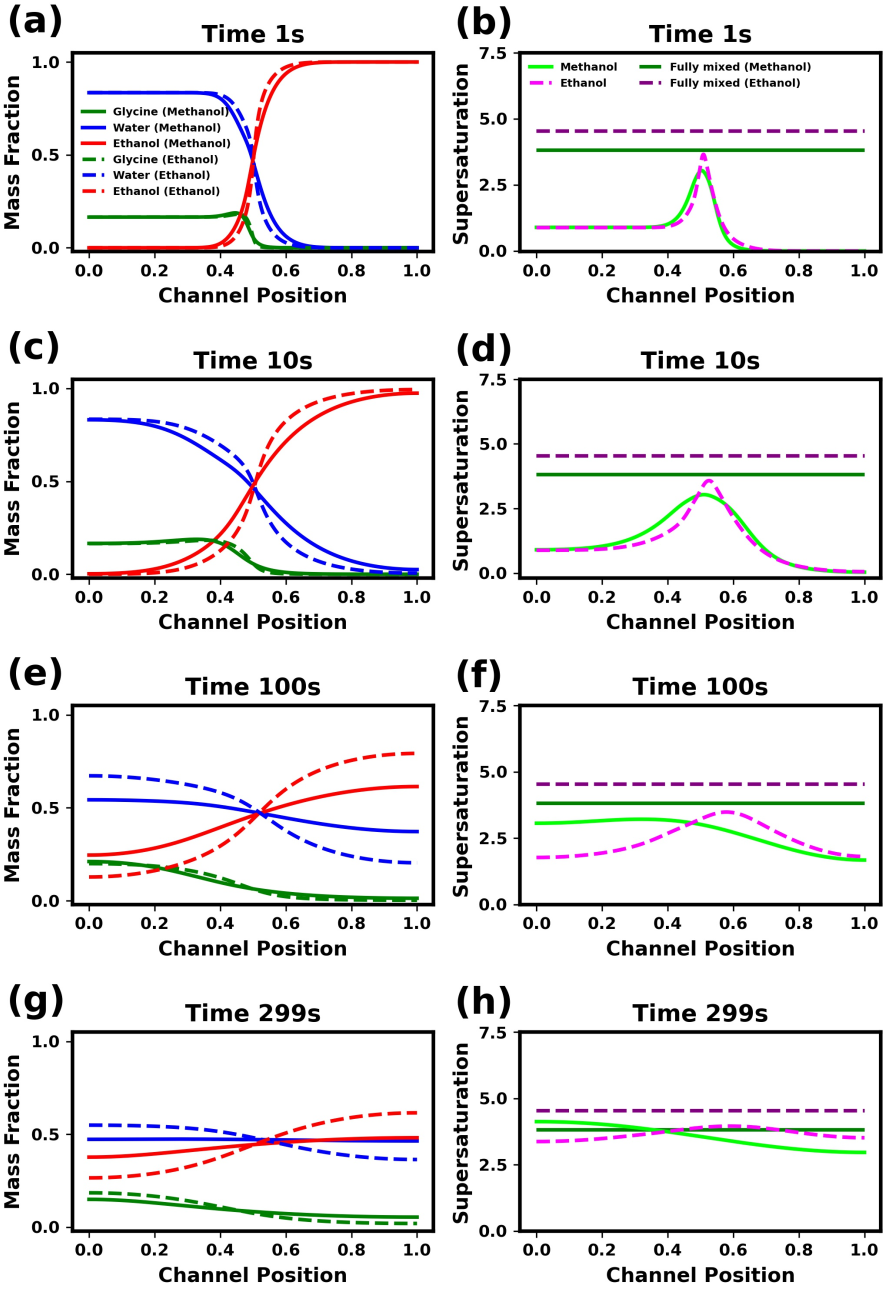

Figure B.1: Effect of anti-solvent choice on diffusive mixing profiles. Solid lines represent methanol, while ethanol is depicted by dashed lines. (a), (c), (e) and (g) show mass fraction profiles at various times, with the corresponding supersaturation profiles given in figures (b), (d), (f) and (h). The initial supersaturation was 0.89 for both anti-solvent systems. Pure anti-solvent was used, and a ratio of 50:50 solution:anti-solvent was used in the 'channel'.

Multi-component effects of the diffusivity matrix results in glycine being 'dragged' into the anti-solvents by the water. With the modelled driving force being activity gradients within the system, the majority of the inter-facial glycine diffuses uphill of its concentration gradient to avoid the anti-solvents. This typically termed 'uphill diffusion'. Figure B.2 shows the activity with respect to glycine for both systems. Note this is related to supersaturation through the solubility constant $\beta$, (see thermodynamics section in article).

At 1 and 10s a peak is seen around the interface, and therefore glycine diffuse down this gradient. The glycine that moves into the anti-solvents with water results in increased activity in the anti-solvents phase.

The methanol system's supersaturation profile is wider, which again highlights the faster mixing, and movement of glycine throughout the channel.

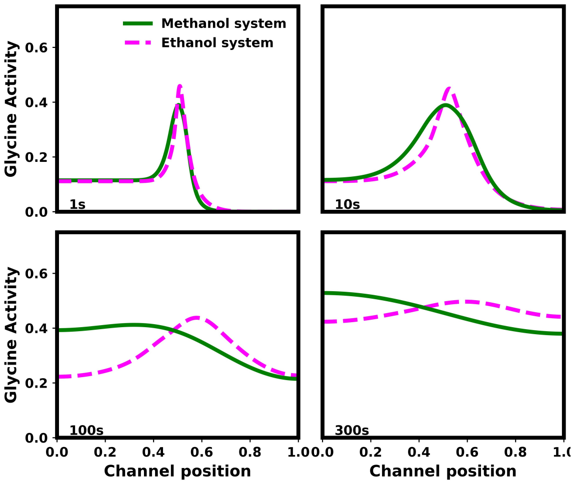

Figure B.2: Glycine activity profiles highlighting the driving force for diffusion. The systems correspond to those shown in figure B.1. Green and magenta depict the methanol and ethanol system respectively. The plots correspond to 1, 10, 100, and 300s

Longer times (100 & 300s) are shown in figure B.1 (e) - (h). Comparing glycine movement in the two systems, it is seen that faster diffusion throughout the channel occurs in the methanol system. This is a result of the greater solvent/anti-solvents diffusivity and intermixing of solvents therefore occurs faster. The presence of water in the anti-solvents reduces the chemical potential penalty invoked by the solute diffusing into the anti-solvents, i.e. it is less thermodynamically unfavourable for glycine to move into the anti-solvents. This is best described by examining the activity gradients of glycine, shown in figure B.2. Starting with the methanol system, (green) the initial 'bump' in activity relaxes as the solvents mix. At 100s, the methanol lowers the solubility of the solution phase, and the activity and composition gradient now have the same direction. Consequently the glycine diffuses down its concentration as one would intuitively expect. In the ethanol system (magenta), water is slower to move into anti-solvents phase, and the 'bump' in activity remains at greater times. This results in glycine still diffusing against its concentration gradient. At 300s, the solvents continue to mix, and glycine follows the water into the anti-solvent. At longer times, glycine concentration eventually acts to equalise across the system. The difference in activity profiles, emphasises the role that the solvent choice plays in the mixing process, especially with regards to the influence on the solutes behaviour.

Referencing back to figure B.1, specifically the supersaturation profiles, the effect of solvent choice clearly has an impact on nucleation conditions. For the methanol system, the peak supersaturation occurs in the solution phase, whilst in the in the ethanol system, it is predicted to be at the interface, before shifting slightly to the anti-solvents side of channel. Solute-solvent interactions influence crystal properties [ref] which differ greatly between the two anti-solvents investigated. These mixing profiles may provide insight into experimental observations in which crystal forms and properties are dependent on the choice of anti-solvents.

A couple of comments on the model:

The systems tend to the relax all activity gradients in the system, which for both investigated leads to a uniform composition across the channel. In the conditions chosen, phase separation does not occur, however, liquid-liquid phase separation may be present under certain circumstances. This is discussed in the Liquid-liquid phase separation section in the main article.

In our simulations, the size of the channel used to represent the fluid layers mixing was 1mm. This leads to relatively long times for mixing to complete, and the supersaturation profiles are likely to dampened by nucleation occurring. At smaller length scales mixing times scale to $\frac{1}{L^2}$.That is, A reduction for 1mm to 0.1mm would decrease mixing time by a factor of 100. Typical length scales in the bachelor range or in the 1-100 microns, and mixing times would be expected to be in the order of magnitude of $0.1 - 10^{-5}$s.

## B.2 Effect of periodic boundary conditions

Composition (mass) trajectories are plotted on ternary phase diagrams highlighting effect of periodic boundary conditions on diffusive mixing profiles are shown in figure B.3. The profiles can be seen to overlap at 1 and 10s, indicating that periodic boundaries does not alter the composition path taking at early times. Although not seen, at long times the trajectories are similar and there is no significant difference between the two boundary conditions.

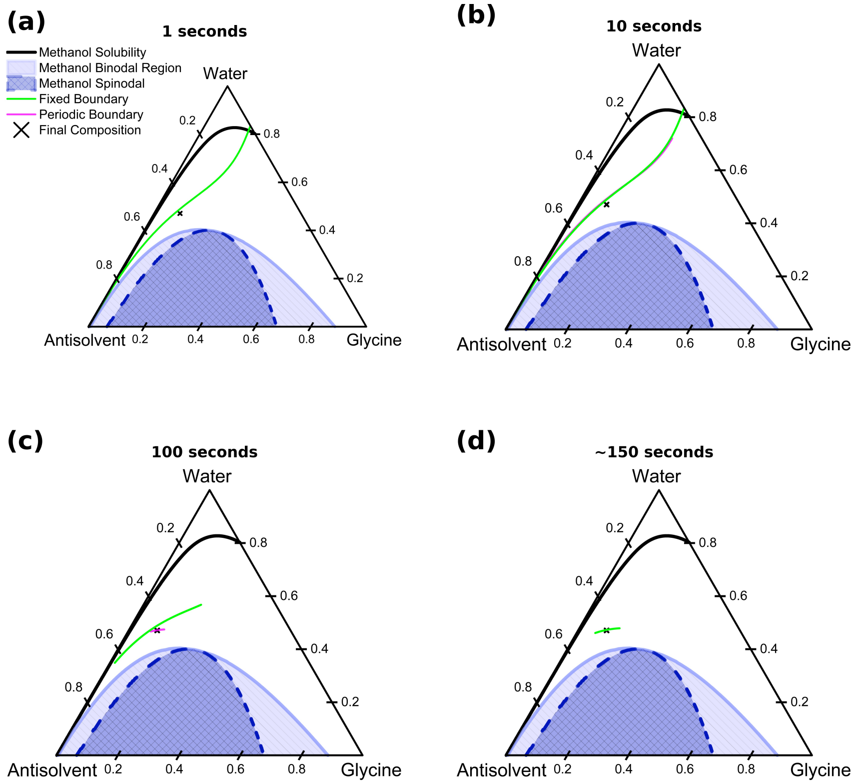

Figure B.3: Composition trajectories plotted on mass based ternary phase diagrams indicating the mass fraction profile across the channel at various times. Green and magenta lines indicate fixed and periodic boundary conditions respectively. The system used was methanol/water/glycine.

# Appendix C

# Mixing Times of Miscible Liquid Systems in Agitated Vessels

## C.1 Temperature Calibration for conductivity probe

During the mixing of 200ml of ethanol to water, enthalpy of mixing is released resulting in a temperature increased of the system. Although the reactor had temperature control, a temperature increase was noticed. Conductivity is a function of temperature, and therefore dependent on the temperature of the vessel. To account for this, a calibration model was fitted. Conductivity was measured at five temperatures; 15,20,25,30 and 35 °C. Figure C.1 shows the obtained conductivity profile.

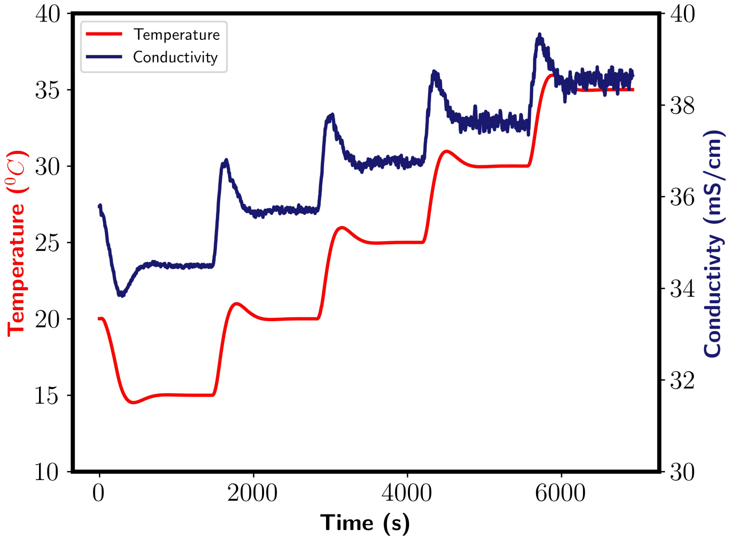

Figure C.1: Conductivity Profile obtained during temperature calibration of the conductivity probe. Left and right y-axis shows temperature and conductivity respectively.

After each temperature increase, conductivity increase followed, before it reached the new equilibrium value. Oscillation were found to occur, which increased with the temperature of the water. An average value was taken as an estimation of conductivity. A straight line function was found to describe the system well, and was selected for the calibration model. Conductivity was then corrected before mixing times were calculated.

## C.2 Mixing time characterisation - typical data

Mixing times were calculated using the definition given in the method section. Figure C.2 shows typical data acquired. A) depicts conductivity profile. The green dashed line indicates the start of mixing which is defines as when the derivative of conductivity increases above 0.1. The corresponding derivatives are shown below in B). The end of mixing is is when the conductivity value is within 5% of the final steady-state value. This is depicted by the purple dashed line. Temperature correction using the temperature calibration model developed in previous section.

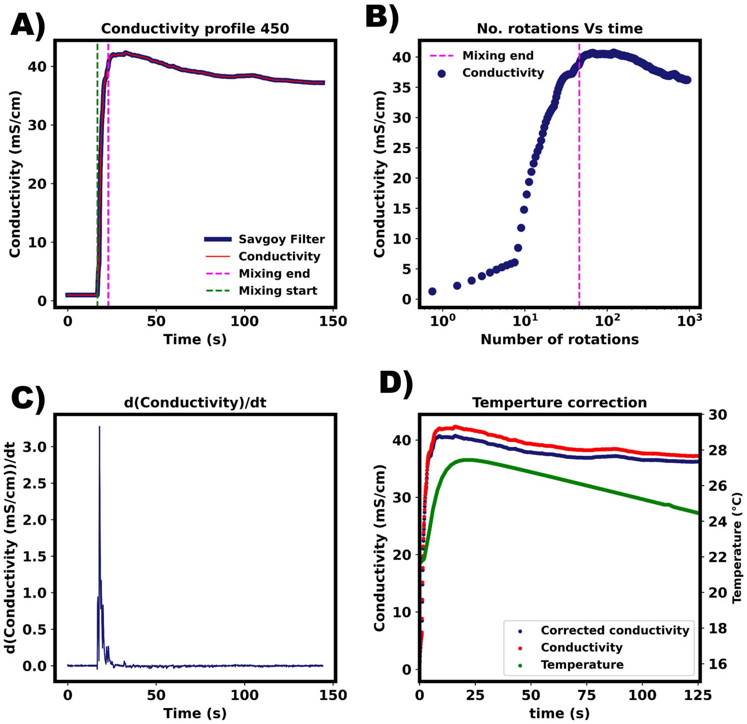

Figure C.2: Mixing determination for experimental data. A) The criteria for 'fully' mixed is the same as for premixed solvents. i.e. when the step increase is within +/- 5% of the final value (conductivity). The green and magenta line indicate the start and end of mixing respectively. B) Mixing profile plotted on conductivity vs Number of impeller rotations. C) First derivative of conductivity profile with respect to time. This is calculated from Savitzky-Golay filter fitted to data from A). D) Temperature calibration curve was calculated using experimental data. This accounts for temperature differences during mixing.

## C.3 Premixed solvent comparison - Averaged mixing times

Average mixing times are shown for different water/ethanol mixtures. We see that experientially mixing time decreases with increasing ethanol fraction, whilst the simulated results, are found to be largely independent on solvent composition.

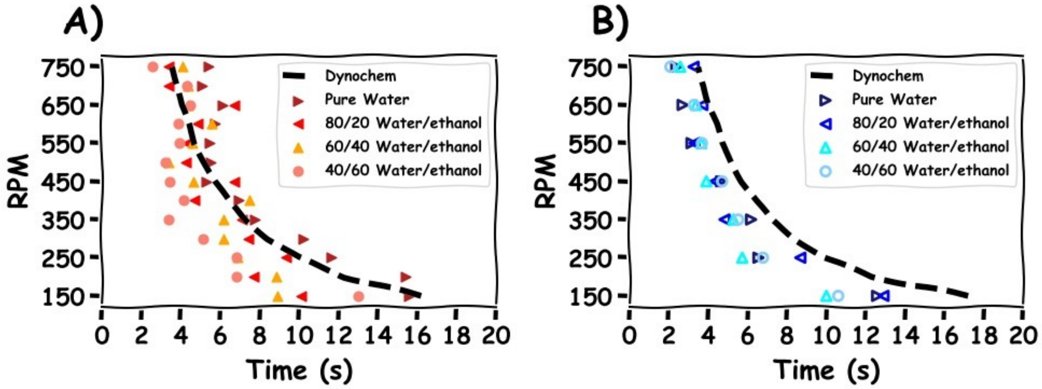

Figure C.3: Average mixing time values compared for different solvent composition. Ratios in legend are given on a percent volume basis. A) Experimental results, B) Mstar CFD. In both magenta line represents dynochem, calculated for pure water.